REDUCED-ORDER AERODYNAMIC MODELS FOR AEROELASTIC CONTROL OF TURBOMACHINES

by

KAREN ELIZABETH WILLCOX

B.E. University of Auckland, New Zealand (1994)
S.M. Massachusetts Institute of Technology (1996)

SUBMITTED TO THE DEPARTMENT OF AERONAUTICS AND ASTRONAUTICS
IN PARTIAL FULFILLMENT OF THE REQUIREMENTS FOR THE DEGREE OF

DOCTOR OF PHILOSOPHY

at the

MASSACHUSETTS INSTITUTE OF TECHNOLOGY

February 2000

Author_____
Department of Aeronautics and Astronautics
November 9, 1999

Certified by_____
Jaime Peraire
Professor of Aeronautics and Astronautics

Certified by_____
James Paduano
Principal Research Engineer, Department of Aeronautics and Astronautics

Certified by_____
Mark Drela
Associate Professor of Aeronautics and Astronautics

Certified by_____
Jacob White
Professor of Electrical Engineering and Computer Science

Accepted by_____
Associate Professor Nesbitt Hagood
Chairman, Department Graduate Committee

Reduced-Order Aerodynamic Models for Aeroelastic Control of Turbomachines

by

Karen Elizabeth Willcox

Submitted to the Department of Aeronautics and Astronautics
on November 9, 1999, in partial fulfillment of the
requirements for the degree of
Doctor of Philosophy

Abstract

Aeroelasticity is a critical consideration in the design of gas turbine engines, both for stability and forced response. Current aeroelastic models cannot provide high-fidelity aerodynamics in a form suitable for design or control applications. In this thesis low-order, high-fidelity aerodynamic models are developed using systematic model order reduction from computational fluid dynamic (CFD) methods. Reduction techniques are presented which use the proper orthogonal decomposition, and also a new approach for turbomachinery which is based on computing Arnoldi vectors. This method matches the input/output characteristic of the CFD model and includes the proper orthogonal decomposition as a special case. Here, reduction is applied to the linearised two-dimensional Euler equations, although the methodology applies to any linearised CFD model. Both methods make efficient use of linearity to compute the reduced-order basis on a single blade passage.

The reduced-order models themselves are developed in the time domain for the full blade row and cast in state-space form. This makes the model appropriate for control applications and also facilitates coupling to other engine components. Moreover, because the full blade row is considered, the models can be applied to problems which lack cyclic symmetry. Although most aeroelastic analyses assume each blade to be identical, in practice variations in blade shape and structural properties exist due to manufacturing limitations and engine wear. These blade to blade variations, known as mistuning, have been shown to have a significant effect on compressor aeroelastic properties.

A reduced-order aerodynamic model is developed for a twenty-blade transonic rotor operating in unsteady plunging motion, and coupled to a simple typical section structural model. Stability and forced response of the rotor to an inlet flow disturbance are computed and compared to results obtained using a constant coefficient model similar to those currently used in practice. Mistuning of this rotor and its effect on aeroelastic response is also considered. The simple models are found to inaccurately predict important aeroelastic results, while the relevant dynamics can be accurately captured by the reduced-order models with less than two hundred aerodynamic states. Models are also developed for a low-speed compressor stage in a stator/rotor configuration. The stator is shown to have a significant destabilising effect on the aeroelastic system, and the results suggest that analysis of the rotor as an isolated blade row may provide inaccurate predictions.

Thesis Supervisor: Jaime Peraire
Title: Professor of Aeronautics and Astronautics

Thesis Supervisor: James Paduano
Title: Principal Research Engineer, Department of Aeronautics and Astronautics

Acknowledgments

So many people have contributed so much to this thesis, it is difficult to know where to begin.

My advisor, Prof. Jaime Peraire, has contributed to making my time at MIT very enjoyable by providing me with an outstanding balance of academic support and freedom. I am extremely lucky to have not only had the benefit of excellent research advice, but also the freedom to pursue my extra-curricular activities. My second advisor, Dr. Jim Paduano, has also provided me with invaluable help and practical suggestions. I especially thank him for the opportunities he has provided for interesting applications of my research and interaction with industry. I have been lucky enough to have a large and very diverse committee. Thanks to Prof. Mark Drela for always knowing the right answer, and offering valuable insight to problems; to Prof. Jacob White for introducing me to the Arnoldi method, and the most interesting result of my thesis; to my minor advisor Prof Carlos Cesnik; and to Dr. Choon Tan for teaching me what I know about internal flows. I would also like to thank Prof. Ken Hall who had many helpful suggestions for my eigenmode problems while he was here at MIT, and Ben Shapiro for the joint work on mistuning and allowing me to use MAST.

Thanks to the current FDRL crew, who are all probably glad they don't have to hear my presentation again. Especially I would like to thank Ed and Anjie, whom I have plagued with countless questions on LaTex, Unix and every other aspect of my computer problems. Thanks also to Prof. Dave Darmofal for reading my thesis and offering me a great deal of important and relevant feedback; and to Tolu "the Unix master" for shell scripts which saved my life and a wonderful program called Cplot (although I still want my money refunded). Thanks also to Bob Haimes who provides a unique and honest perspective on life at MIT, and has provided me with much encouragement. I would especially like to thank Jean Sofronas whose hard work so often goes unnoticed. The organisation she has brought to the lab has made life so much easier, especially for those of us trying to track down Jaime.

To those who have gone before (and escaped) : my former office mate "by the way my real name is Josh Elliot" for setting the example of thesis defense preparation (by the way - London is further than Florida, Josh) and for providing the inspiration for the infamous Mardi Gras trip. To the incorrigible group who helped me survive my first years at MIT - Graeme, Ray, Jim, Guy, Mike, Carmen, Lou and Ernie. In particular, to Graeme Shaw who has been like a brother to me, to Mike Fife for being the wonderfully unique person that he is, and to Ray for staying behind to share the "later years".

Away from the lab, I have been fortunate to meet many interesting people and form some priceless

friendships. I would like to thank my housemates Matt and Chris for many fun times, and for not throwing out the vegemite; Pat Kreidl who always gave me the best perspective on things when I needed it most, and showed us all not to be afraid of following our dreams; Rebecca Morss who has been adventurous (or stupid) enough to go with some of my crazier ideas and outfits; Blotto Van Der Helm for some of my more exciting moments in a car; Simon Karecki for introducing me to Jagermeister; Matthew Dyer for introducing me to bridge; Samuel Mertens for all the chocolate; and Yoshi Uchida for many great hours of chocolate, ice-cream and conversation. I would also like to thank Tienie Van Schoor for running the most hospitable company ever, Brett Masters for being the other NZer, and Gert Gogga Muller for his help in my endeavours to master Afrikaans.

I would especially like to thank William Web Ellis - without that crazy game I would never have survived graduate school. In particular, my years playing with the MIT women's rugby team are some of the best sporting memories of my life - too many great ruggers to mention here, and great coaches, I just hope I was not too bossy on the field! Playing with Beantown RFC has provided me with a fantastic sporting challenge, and also the opportunity to meet many inspiring women. In particular I would like to thank Sonya Church, Liz Satterfield, Jen Crouse, Anna Mackay and Daniel Scary Spice for their friendship. I would have liked to thank the All Blacks for providing me with the best post-defense celebration opportunity, but .... Rugby has given me the opportunity to form some very special friendships - in particular with Marianne Bitler who taught me all I know about midriff shirts - I'm just sorry I never learned to go without sleep; and Judi Burgess for the margaritas when I needed them and when I really didn't, and for really appreciating the little brown bird in me.

I must also thank the faculty and students of my undergrad department at the University of Auckland for the encouragement and help to come to the US for grad school. In particular, Dr Roger Nokes provided some much needed support during the GREs and application process. To my friends James Deaker, Mike O'Sullivan, JP Hansen and Tim Watson - thanks for the visits and the emails to this poor stranded kiwi. And of course thanks to Ivan Brunton and Chris Bradley for their best efforts to sabotage my defense preparation, and to Mark and Justine Sagar for the wonderful times while they were in Boston (and the coolest bathroom ever!).

I owe a special debt of gratitude to my Thursday afternoon counselling group for their unique perspective on life. I am honoured to have developed a friendship with Michael Cook, who is one of the most unselfish people I have ever met. I would also like to give special thanks to Tony and Doreen Puttick who have been my "American" surrogate parents and have contributed so much to my life here in Boston. I only hope I can one day repay your hospitality down under.

I specially owe thanks to my sole-mate Vanessa Chan for recognising my accent, never being the voice of reason, and always providing the transport. Who would have thought MIT could be so much fun! And last but certainly not least, Jaco Pretorius who has shared so much of the pain, and now hopefully the rewards (and a more peaceful night's sleep). He has provided me with all the support and understanding to finish this degree, and I have the best beer cooler in the world. Beste wense met jou beroep as professionele, sosiale gholfer !

Finally, I must thank my family, who from afar have provided so much love and support. To Mum, Dad, Dawn and Keith : thanks for the emails, the letters, the newspaper clippings, the lamb, the vegemite and the clothes to let me dress like a real kiwi. I will thank in advance my brother for the ride in the F-16, and my sister for the visit to her excavation site, and wish them both the best of luck in their careers.

And finally to my grandmothers, Grace and Flora, two very unique and inspiring women who over the last 27 years have done so much for me. To you both I dedicate this thesis. Happy reading!

Contents

List of Figures

Chapter 1

Introduction

Aeroelasticity is defined in [5] as *phenomena which exhibit appreciable reciprocal interaction (static or dynamic) between aerodynamic forces and the deformations induced thereby in the structure of a flying vehicle, its control mechanisms, or its propulsion system.* With the current trend towards increased operating speeds and more flexible blading, aeroelasticity has become a critical consideration in the design of gas turbine engines, and has a large impact on both stability and dynamic response considerations.

Flutter is of particular concern in the design of bladed disks. Unstable vibrations may arise due to coupling between the aerodynamics and the structural dynamics. If the fluid does work on a vibrating blade so as to amplify or maintain the vibration, then the blade is said to be undergoing flutter [31]. The ability to understand and predict this phenomenon is crucial to ensuring that the engine component will operate within stability boundaries, and thus has a large impact on the design process. Appropriate blade design, together with strategies for controlling the onset of instabilities, can significantly impact the stable operating range, potentially leading to better engine performance.

Dynamic response of the blades to various inputs, such as gusts or upstream obstacles, is an important factor in determining the stress loads on the blades and the wear of the engine. In particular, periodic forcing inputs, such as that due to an upstream structural support or blade row, may induce a large blade response if the frequency of excitation is near the blade natural frequency. Blade forced response vibrations can lead to high cycle fatigue, which can in turn cause blade failure. Accurate prediction of blade response to external inputs can facilitate improved understanding of forced response phenomena, allowing design strategies to be adopted to minimise their impact and potentially prolong engine lifetimes.

1.1 Aeroelastic Modelling

Aeroelastic phenomena involve a complicated interaction between the aerodynamics and the structural dynamics of the blades. The challenge is to develop a model which accurately captures the relevant dynamics of both the fluid and the structure, and more importantly, the interactions between the two. Consideration of aeroelastic effects is vital at the design stage to ensure that the compressor will operate within an acceptable response region. The models must therefore satisfy an additional requirement that they are computationally efficient and thus practical to implement within a design framework. Moreover, since aeroelastic instabilities represent a significant impediment to obtaining better engine performance, it may be desirable to consider active control strategies as a means of extending the stable operating range. For such an approach to be possible, the aeroelastic model must be suitable for incorporation to a control framework, which places restrictions upon the size and form of the model.

Traditionally, the structural portion of the problem has been the easier of the two, since linear models are generally adequate to model the structural dynamics. The disks are often assumed to possess cyclic symmetry so that a model of just a single blade passage can be used to obtain the dynamic response of the entire bladed disk. These dynamics can be accurately captured with a finite element model. The system of equations governing the structural dynamics is symmetric, so that evaluation of natural modes (eigenmodes) is relatively straightforward. If deformation of blade shapes is not considered to be important, a simpler structural model may be used. For example, each blade might be given the freedom to move rigidly in certain displacement directions as in a typical section model [54]. In this case, the number of structural states is greatly reduced.

For a given bladed disk geometry, the structural modes must be computed just once, and so it is practical to perform a large finite element analysis to obtain the modal information. However the flow must be modelled over a large range of operating conditions and forcing inputs, therefore it is crucial that the aerodynamic model be computationally efficient. Moreover, the system of equations governing the aerodynamics are not symmetric, and it is very difficult to determine the flow eigenmodes. We therefore require either an alternative means to determine the modes of a complicated aerodynamic model, or a simplified model which can be incorporated to the aeroelastic analysis in its entirety. Such a model should be applicable over a wide range of geometries and operating conditions, and also for a variety of excitation modes.

The most general aerodynamic model describes the blade forces as a function of blade motion, flow operating conditions, reduced frequency, blade geometry and a host of other problem parameters [7].

Within the state-of-the-art, the best possible aerodynamic models are obtained via computational fluid dynamics (CFD) models. By numerically solving the unsteady Euler or Navier-Stokes equations, improved modelling of the flow and better understanding of fluid phenomena can be obtained. However these techniques are generally too computationally expensive to use for unsteady analyses, especially if the full rotor and more than one blade row need to be considered. More efficient methods for time-varying flow can be obtained if the disturbances are small, and the unsteady solution can be considered to be a small perturbation about a steady-state flow [23]. In this case, a set of linearised equations is obtained which can be time-marched to obtain the flow solution at each instant. Cyclic symmetry of the bladed disk can be used to decompose the linear problem into a series of modal problems each containing a single spatial frequency. The analysis can then be carried out for each mode on a single blade passage. Any of the CFD techniques result in models with tens of thousands of states per blade passage, even in two dimensions. A model of this size is not practical for computing stability boundaries, nor is it appropriate as a design tool. In addition, the number of states is prohibitively high for control applications.

Instead, for aeroelastic analyses of turbomachines, the approach has typically been to use simplified aerodynamic models which can be incorporated into the aeroelastic framework in their entirety. The flow is usually assumed to be two-dimensional and potential. Efficient semi-analytic models for lightly loaded thin blades have been developed for subsonic flow [61] and for supersonic flow [2]. These methods are useful near design conditions but inadequately predict the flow off-design, as blade loading effects become important [56] and also do not exist for all flow regimes; in particular the modelling of transonic flows poses a difficulty. Often, the assumptions involved in deriving these simplified models further restrict their range of validity, for instance they may not be valid for high spatial frequency disturbances [40]. Another option is to use an "assumed-frequency" method in which an aerodynamic model is derived from a CFD model for a specific case. The flow is assumed to be sinusoidal in time at a particular frequency, which allows high-fidelity influence coefficients to be calculated from the CFD model. Results have been reported using coefficients calculated from Whitehead's incompressible, two-dimensional aerodynamic model [60] by Dugundji and Bundas [10]. Crawley [7] and Crawley and Hall [8] use coefficients for supersonic flow calculated from the model of Adamczyk and Goldstein [2]. These influence coefficients, although strictly only valid at the temporal frequency selected (usually the blade natural frequency), are then used to provide the aerodynamic model for all flows. They are coupled to the structural model as constant coefficients that are independent of problem parameters such as forcing frequency and boundary conditions. If there is not a significant degree of aerodynamic coupling in the system, then the structural eigenvalues fall close to the blade natural frequency and the assumed-frequency model

predicts the aeroelastic system dynamics well. However, if there is a significant amount of frequency scatter or a large amount of aerodynamic damping, the assumed-frequency models do not provide an accurate representation of the system dynamics. Moreover, even if the aeroelastic eigenvalues are predicted accurately, these models can only predict the system forced response accurately if the forcing frequency is close to the assumed frequency.

1.2 Model Order Reduction

Ideally, we would like to develop an aeroelastic model with a low number of states, but which captures the system dynamics accurately over a range of frequencies and forcing inputs. This can be achieved via reduced-order modelling in which a high-order, high-fidelity CFD model is projected onto a reduced-space basis. If the basis is chosen appropriately, the relevant high-fidelity system dynamics can be captured with just a few states. Figure 1-1 illustrates the concept of reduced-order modelling from CFD. The CFD model can be viewed as an input/output system; operating conditions, blade motions and incoming flow disturbances represent the inputs, while the outputs are functions of the flow field, often the forces and moments acting on each blade and outgoing flow disturbances. A reduced-order model can be developed which replicates the output behaviour of the CFD model over a limited range of input conditions. The range of validity of the reduced-order model is determined by the specifics of the model order reduction procedure.

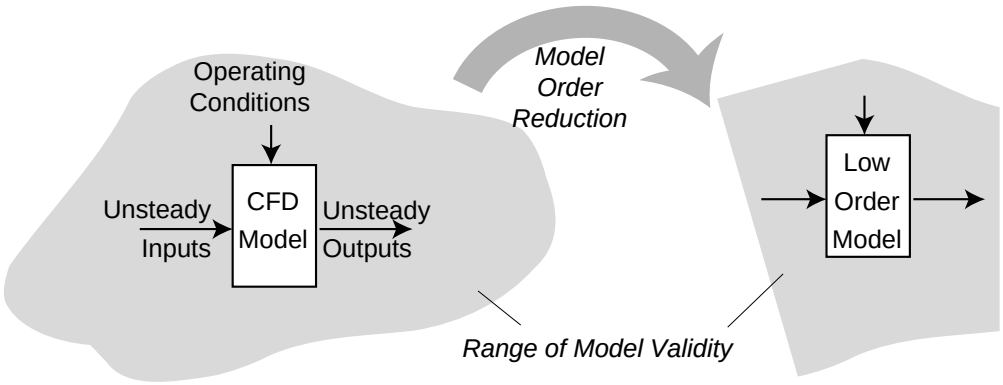

Figure 1-1: Concept of reduced-order modelling from CFD. Unsteady inputs include blade motion and incoming flow disturbances. Outputs of interest are typically outgoing flow disturbances and blade forces and moments.

Reduced-order modelling for linear flow problems is now a well-developed technique and some re-

duction methods are reviewed in [9]. One possibility for a basis is to compute the eigenmodes of the system. This has been done for flow about an isolated airfoil, considering both the Euler equations [46] and the Navier-Stokes equations [38]. In the turbomachinery context, eigenmodes have been used to create reduced-order models for incompressible vortex-lattice models [22], and for linearised potential flow [24, 14]. Along with the use of static corrections or *mode-displacement* methods [5], this approach can lead to efficient models and the eigenmodes themselves often lend physical insight to the problem. However, typical problem sizes are on the order of tens of thousands of degrees of freedom per blade passage even in two dimensions, and solution of such a large eigen-problem is in itself a very difficult task, especially for the Euler or Navier-Stokes equations.

The proper orthogonal decomposition technique (POD), also known as Karhunen-Loéve expansions [36], has been developed as an alternate method of deriving basis vectors for aerodynamic systems [37, 53, 4] and has been widely applied to many different problems. Romanowski used the POD to derive a reduced-order model for aeroelastic analysis of a two-dimensional isolated airfoil [45]. In a POD analysis, a set of instantaneous flow solutions or *snapshots* is obtained from simulations of the high-order CFD system. This data is then used to compute a basis which represents the solution in an optimal way. Typically, the POD snapshots would be obtained from a time domain simulation of the full bladed disk. This expensive computation can be avoided by exploiting the linearity of the governing equations and using the frequency domain to obtain the snapshots efficiently on a single passage. Frequency domain POD methods have been developed for analysis of a vortex lattice aerodynamic model [32], and for an Euler model of flow through a hyperbolic channel [20]. A unique application of the POD to turbomachinery flows has been developed in this research [64].

An alternative to both the eigenmode and the POD approaches is to use an Arnoldi-based method to compute the basis. The Arnoldi algorithm can be used to generate basis vectors which form an orthonormal basis for the Krylov subspace. The full set of Arnoldi vectors spans the same solution space as the system eigenvectors. An efficient reduced set can be constructed by considering both inputs and outputs of interest. Padé-based reduced-order models have been developed for linear circuit analysis using the Lanczos process [13]. This approach matches as many moments of the system transfer function as there are degrees of freedom in the reduced system. While the Arnoldi vectors match only half the number of moments as the Padé approximation, they preserve system definiteness and therefore often preserve stability [52]. This Arnoldi-based approach is a novel method for turbomachinery and is implemented efficiently in this thesis through exploitation of linearity [65].

Once the basis has been computed, the CFD model is projected onto the reduced-order subspace to

obtain the reduced-order model. In this research, a model for the full bladed disk will be developed in the time domain and cast in state-space form. In order to accurately capture system dynamics over a range of excitation modes and frequencies, the model requires several hundred states per blade row, which represents three orders of magnitude reduction from the original CFD model. The general input/output time domain form of the model allows the flexibility to handle problems that cannot be considered with the current tools available. For example, the reduced-order models developed here can be easily incorporated within a global engine model and coupled to upstream and downstream engine components. The tractable size of the model also makes it amenable to control design, while its ability to capture dynamics over a range of frequencies allows accurate representation of both the uncontrolled and the controlled systems. Another advantage of the reduced-order models is that they can be used to determine forced response to an arbitrary forcing (a general function in time and space). The assumption of single frequency sinusoidal forcing in the influence coefficient models can be extremely restrictive in, for example, determining gust response or the effect of an upstream blade row.

1.3 Reduced-Order Modelling Applications

Although useful for aeroelastic analyses in which a low degree of interblade coupling is present, a host of cases exist for which the assumed-frequency models are inadequate. Some of these will be addressed in this research, and include analysis of mistuned bladed disks and forced response to general inlet disturbances such as those generated by neighbouring blade rows. Moreover, interesting aeroelastic phenomena are more likely to be encountered when a significant amount of aerodynamic coupling exists in the system. The cases of most relevance are therefore often outside the range of validity of the assumed-frequency models. It will be shown that in these situations a reduced-order model with generalised boundary conditions can play an important role.

Currently in most aeroelastic analyses the bladed disk is assumed to be tuned, that is all blades are assumed to be the same. In practice, small blade to blade variations exist, due both to limitations in the manufacturing process and to engine wear and tear. If the aeroelastic response of the bladed disk is to be computed accurately, these factors must be included in the analysis [12]. Mistuning can lead to mode localisation [57], and thus the generation of large forces on individual blades. The actual forced response amplitude for some blades may therefore be much higher than that predicted by a tuned analysis, which has serious ramifications for prediction of engine life and high cycle fatigue. Wei and Pierre [58] and Ottarsson and Pierre [43] determined that moderately weak interblade

coupling was required for the occurrence of significant forced response amplitude increases. Kruse and Pierre [33] consider two sources of interblade coupling: aerodynamic coupling and disk structural coupling. Aerodynamic coupling was found to be a significant factor, increasing the vibratory stress levels by 70% over the tuned response. Kenyon and Rabe [30] measured the response of an integrally bladed disk (blisk) to inlet forcing, and compared the results to those predicted using a structural reduced-order model. It was concluded that the response was strongly influenced by aerodynamic loading.

In all of these studies, the aerodynamic coupling was represented in the form of unsteady aerodynamic influence coefficients. Kenyon and Rabe [30] found that the response was dominated by aerodynamic phenomena not effectively captured by the model, which led to an inaccurate prediction of the rotor response. It was concluded that more consideration must be given to the role of aerodynamic coupling in mistuned bladed disks. When mistuning is present, the discrete spatial modes present in the system do not decouple, and a much greater degree of aerodynamic coupling is observed. It is therefore not surprising that influence coefficients derived at a specific frequency do not accurately capture the important dynamics. This is clearly an application which requires the use of more sophisticated aerodynamic models, although the need for computational efficiency is even more stringent due to the lack of cyclic symmetry in the problem. Any analysis (both structural and aerodynamic) must consider the full bladed disk. However, a simulation of a full finite element blade assembly is very expensive, and so reduced-order structural models have been developed directly from finite element models [42]. The motion of an individual blade is assumed to consist of cantilever blade elastic motion and disk-induced static motion. Finite element models of the bladed-disk components are established for each of these motions, and then systematically reduced to generate lower order models. These reduced-order models have been used to investigate the forced response of mistuned bladed disks and to examine the physical mechanisms associated with mistuning [34]. A natural extension is to obtain reduced-order models for the aerodynamics. Such models will allow the entire bladed disk to be modelled with a reasonable number of states, and will also be valid over a range of frequencies, thus capturing the important dynamics even when a significant amount of aerodynamic coupling exists.

It has also been shown that mistuning can increase the stability margin of a compressor [29, 28], thus suggesting intentional mistuning as a form of passive control for flutter. The mistuning problem has been cast as a constrained optimisation problem [8, 50] in which a deliberate mistuning pattern is chosen so as to maximise the stability margin of a blade row. Forced response sensitivity to random mistuning is observed when a lightly damped structural mode exists and there is also a

significant amount of variation in the damping ratios of the structural modes [50]. Mistuning serves to reduce the interblade coupling, decreasing the scatter in the structural eigenvalues and thus the forced response sensitivity [7]. Shapiro [49] discusses the idea of robust design in which a certain level of random mistuning is assumed to always exist in practice. An intentionally mistuned design point is then chosen so that the worst case forced response due to random variations about the intentionally mistuned design point is more acceptable than the worst case forced response due to random variations about the tuned design point.

It is possible to encounter both structural and aerodynamic mistuning. In the former, the mass and/or stiffness characteristics of each blade may vary, while the latter describes variations in blade geometry and flow incidence angles. Although just structural mistuning will be considered here, the reduced-order models could be extended to include aerodynamic mistuning effects. A great deal of interest exists in the effects of aerodynamic mistuning, although it has not been addressed in the literature. This is, for the most part, due to the lack of models which can incorporate such effects. Without higher fidelity aerodynamic models of the form developed in this research, the effects of mistuning in bladed disks cannot be predicted accurately. This is clearly an area where reduced-order aerodynamic modelling can contribute significantly towards improving prediction and design tools, and also towards improved understanding of physical effects.

Another area in which reduced-order modelling offers significant benefits is in the determination of interblade row coupling effects. Almost all current aerodynamic tools make the assumption that the bladed disk can be analysed as an isolated blade row, which means that the potentially important unsteady effects of neighbouring blade rows are ignored. Experimental evidence shows that these effects are indeed significant in computing the aeroelastic response of a blade row [39]. A rotating blade row moves through the wakes of an upstream stationary blade row, resulting in a periodic forcing excitation which may have important repercussions in determining blade fatigue. The aerodynamic coupling between adjacent blade rows has been investigated by time marching the fluid governing equations [44, 17]. In a general problem, these time-marching CFD approaches require the full bladed disks to be included in the computational analysis, unless the number of blades in each row is such that the problem can be reduced to a smaller periodic domain. The models are therefore computationally very expensive and not suitable for incorporation into an aeroelastic analysis. Giles [16] introduces the idea of "time inclining" which allows the computation to be performed on a single blade passage. However this technique cannot be extended to more than two blade rows.

More computationally efficient methods for multiple blade rows have been developed by considering

certain modes to be reflected and transmitted between the blade rows, thus allowing the analysis to be performed in the frequency domain on a single blade passage [6, 25]. Conventional frequency domain CFD methods are used to compute reflection and transmission coefficients which describe the response of an isolated blade row to an incoming perturbation wave. It is assumed that the pressure and vorticity perturbation waves travelling between the blade rows can be modelled with just a few modes. Because the analysis is performed in the frequency domain, it is also assumed that all forcing (blade motion and inlet/exit disturbance waves) are sinusoidal in time.

The reduced-order models developed in this research can capture the relevant system dynamics with just one or two hundred states per blade row. It is therefore practical to derive such models for each blade row of interest and to couple them together so that a full time-domain model of the multiple blade row system is obtained. In this procedure, there is no assumption made about the modal content of the waves travelling between the blade rows, other than the range of inputs sampled when deriving the reduced-order model. Several stages can be coupled in this framework easily and efficiently, thus providing a means of quantifying the effects of neighbouring blade rows. The system can be time-marched to determine forced response and aeroelastic stability. In addition to neighbouring blade rows, models of other engine components may be included in the analysis. In this way, a global engine analysis may be performed. This may be useful in determining post-stall transient behaviour, in which it is important to consider the compressor as interacting dynamically with other engine components [40].

1.4 Outline

The goal of this research is therefore to develop a low-order, high-fidelity aerodynamic model which is suitable for incorporation into aeroelastic analyses where current models are insufficient. A model of the full rotor will be derived from a CFD method using model order reduction techniques, and cast in the time domain.

In Chapter 2, the underlying computational model of the aeroelastic system is presented. The two-dimensional linearised Euler equations are used for the aerodynamic model, while the structural dynamics are represented by a simple typical section analysis. An efficient modal decomposition method for solving the linear aerodynamic system will be discussed. The CFD model is validated against experimental data for both steady and unsteady flows.

The model order reduction process is discussed in Chapter 3 and applies to any linearised compu-

tational method. Here the reduction is applied to the aeroelastic model presented in Chapter 2. If the underlying CFD method were available, it would be straightforward to extend the methodology to three-dimensional and/or viscous flows, as well as to more complicated structural dynamic models. Several options for performing the reduction are discussed. The first is a simple influence coefficient model, which is the type typically used in practice. Three techniques for obtaining more general reduced-order models are presented. The first is an eigenmode approach, which is not suitable because of the difficulties associated with computation of the aerodynamic eigenmodes. The second method is a unique application of the POD to turbomachinery flows which exploits linearity of the problem to compute the models efficiently in the frequency domain on a single blade passage. Finally, the method of choice involves an Arnoldi-based approach which is extremely efficient to compute. In this case a basis is selected which replicates the input/output characteristic of the CFD model.

In Chapter 4, reduced-order modelling results are presented for a transonic twenty-blade rotor. The aeroelastic response of the system is computed using the POD and Arnoldi approaches, and compared to that obtained using a conventional influence coefficient approach. It is found that in many cases the influence coefficient model cannot capture the dynamics relevant to flutter and forced response accurately, while the reduced-order models do so with a three order of magnitude reduction from the original CFD method.

Analysis of a structurally mistuned transonic rotor is considered in Chapter 5. The reduced-order models are incorporated into a mistuning design framework and used to provide high-fidelity results for robust design. Analysis of random mistuning in a rotor is performed and compared to results obtained using a simple assumed-frequency model. Mistuning is identified as an application where the use of high-fidelity reduced-order models is critical for predicting aeroelastic response accurately.

In Chapter 6, a multiple blade row model is developed and used to analyse a stator/rotor combination in a low-speed compressor. The stator is found to have a significant destabilising effect on the system, and it is shown that the isolated blade row analysis inaccurately predicts system stability and forced response.

Finally, in Chapter 7 conclusions and recommendations for future work are presented.

Chapter 2

Aeroelastic Model

Aeroelasticity is concerned with the interaction between structural dynamics and aerodynamics. In the context of turbomachines, models must be developed which accurately describe the deformations of the bladed disks, and also the complicated flow through the engine. While the structural dynamics can typically be well represented by a linear analysis, it is generally agreed that the unsteady aerodynamic effects are extremely complex. At least some of the flow details (such as shock motion, blade loading, viscosity and boundary conditions) must be modelled to obtain realistic analyses. Because very little data exists to isolate the most important of these details, the current state of the art utilises CFD analyses to capture as much of the physics as possible.

When deriving an aeroelastic model, we are often not concerned with the precise details of the flow field, but instead with predicting certain relevant output quantities accurately. These outputs are typically the forces and moments acting on the blades, and sometimes outgoing flow disturbances at the passage inlet and exit. The aerodynamic problem can therefore be viewed as an input/output system where blade motions, incoming flow perturbations and flow operating conditions provide the inputs. Similarly, the structural model can be viewed as a means of obtaining the blade displacements and stresses given a specific forcing configuration. Figure 2-1 illustrates the concept of an input/output aeroelastic model. Computational models, such as finite element models for the structure and CFD models for the flow, should provide an accurate representation of the appropriate outputs given a set of input conditions. The operating conditions, an important input to the aerodynamic model, are represented by many different parameters (for example Mach number, rotation speed, pressure ratio), and so the aerodynamics constitute a complicated problem with many controlling parameters.

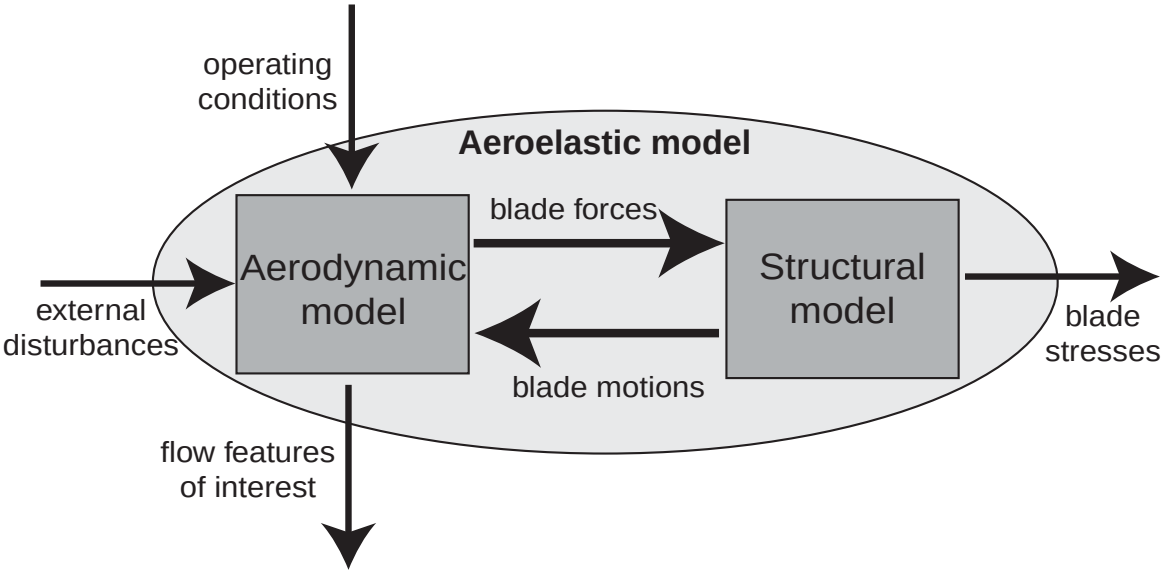

Figure 2-1: Input/output view of aeroelastic model.

The system has associated to it a certain "state", which, along with the input, completely determines the behaviour and output characteristic. For example, for the structural system, the states may be the instantaneous deformations and motions of the blades, while the aerodynamic states may be the values of the flow variables over the entire domain. The computational tools must provide a model of how the system states evolve with time due to certain forcing inputs. In general, we will consider a bladed disk with r deformable blades, operating at conditions represented by Θ. In addition we will allow an external flow disturbance d. A general nonlinear model takes the form

$$\frac{d\mathbf{s}}{dt} = f(\mathbf{s}, \Theta, \mathbf{d}, t) \qquad \mathbf{y} = g(\mathbf{s}, \Theta, \mathbf{d}, t), \tag{2.1}$$

where $\mathbf{s}$ contains all the aerodynamic and structural states for the full bladed disk, and $\mathbf{y}$ contains all outputs of interest.

If we consider small blade deformations and small deviations of the aerodynamics from the mean operating conditions, then (2.1) can be linearised to obtain

$$\frac{d\mathbf{s}}{dt} = M(\overline{\Theta})\mathbf{s} + E(\overline{\Theta})\mathbf{d}, \tag{2.2}$$

where $M(\overline{\Theta})$ represents the linearisation of the unforced dynamics evaluated at the mean operating conditions, $\overline{\Theta}$, and $E\mathbf{d}$ is the forcing term due to external disturbances.

2.1 Aerodynamic Model

As Figure 2-1 shows, there are many factors affecting the complicated flow through an aeroengine. Full three-dimensional simulation of the Navier-Stokes equations can provide an accurate representation of the system, but is not always practical to implement or necessary for a given problem. In many cases, simplifying assumptions about the flow can be made, reducing the complexity of the aerodynamic model. For example, a compressor stage with a large ratio of hub diameter to tip diameter may be approximated by a linear, two-dimensional cascade of blades moving in a straight line. Moreover in some problems, viscous and/or compressibility effects may not be considered important. In this research we consider two-dimensional, inviscid flows. Although these assumptions somewhat restrict the range of applicability of the models, important insight and understanding can be gained which is relevant for many turbomachinery problems, including flow through transonic compressors.

Compressors comprise two types of blade rows. The rotating rows, or rotors, consist of a disc with blades attached, and are usually followed by a stationary row of blades known as a stator which redirect the flow to the axial direction. A single compressor stage with a rotor and stator is shown in Figure 2-2. We will consider unsteady flow through the compressor due to external disturbances in the flow passages. These could be from an inhomogeneity in the incoming flow field (for example a temperature variation) or due to an upstream blade row or strut. In addition, we allow unsteady motion of the rotor blades which are modelled as flexible structures. In the models developed here, each rotor blade can move with a bending displacement (plunge) and a twist about an elastic axis (pitch), although in general, blade shape deformations could be included. The stator blades are assumed to be rigid.

Consider a single blade row of the stage shown in Figure 2-2. The computational domain for this blade row is depicted in Figure 2-3. The circumferential coordinate θ is related to the rectilinear coordinate y by

$$\theta = \frac{2\pi y}{rP} \qquad 0 \le y \le rP, \quad 0 \le \theta \le 2\pi, \tag{2.3}$$

where r is the number of blades in the cascade and P is the inter-blade spacing or pitch. Computational boundaries exist at the inlet and exit of the blade row, and on the surfaces of each blade. In addition, we impose periodic boundaries to retain the circumferential nature of the problem. If a point on the lower periodic boundary has coordinates (x, y_l) and circumferential location $\theta_l = \frac{2\pi y_l}{rP}$, then the corresponding point on the upper periodic boundary $(x, y_l + rP)$ has circumferential location

$\theta_l + 2\pi$. We therefore impose the condition that for any flow quantity u,

$$u(x, y_l) = u(x, y_l + rP). \tag{2.4}$$

The periodic boundaries are shown in Figure 2-3 to be horizontal for the incoming flow and roughly aligned with the exit angle of the blade for the outgoing flow. However, the orientation of these boundaries is arbitrary, and does not affect the flow computation. The alignment is chosen for convenience; for example for a viscous calculation we would be interested in flow quantities along the blade wake, hence it is useful to align the periodic boundaries as shown in Figure 2-3.

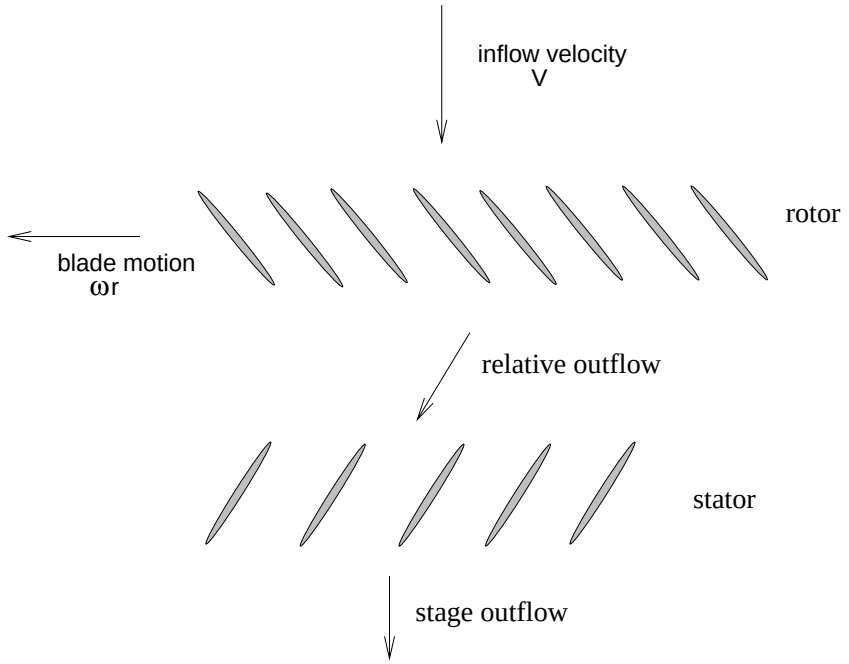

Figure 2-2: Rectilinear, two-dimensional representation of compressor stage.

2.1.1 Governing Equations

Consider a time-varying control volume $\Omega(t)$ with boundary $\Gamma(t)$ as shown in Figure 2-3. The Euler equations governing the unsteady two-dimensional flow of an inviscid compressible fluid can be written in integral form as

$$\frac{\partial}{\partial t}\int_\Omega W\,dxdy + \oint_\Gamma (Fn_x + Gn_y)\,d\Gamma = 0 \tag{2.5}$$

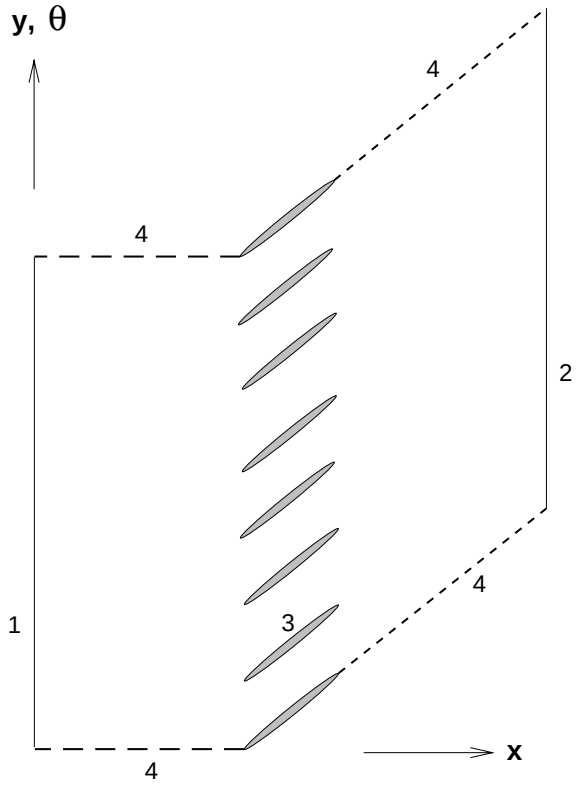

Figure 2-3: Computational domain for single blade row. Inlet boundary (1), exit boundary (2), blade surfaces (3) and periodic boundaries (4).

where n_x and n_y are the cartesian components of the unit normal vector pointing out of Ω, W is the unknown vector of conserved variables given by

$$W = (\rho, \rho u, \rho v, e)^T \tag{2.6}$$

and F and G are the inviscid flux vectors given by

$$F = \begin{pmatrix} \rho(u - x_t) \\ p + \rho u(u - x_t) \\ \rho v(u - x_t) \\ pu + e(u - x_t) \end{pmatrix} \quad \text{and} \quad G = \begin{pmatrix} \rho(v - y_t) \\ \rho u(v - y_t) \\ p + \rho v(v - y_t) \\ pv + e(v - y_t) \end{pmatrix}. \tag{2.7}$$

Here ρ, u, v, p, and e denote density, cartesian velocity components, pressure, and total energy, respectively. x_t and y_t are the speeds in the x and y directions with which the boundary $\Gamma(t)$ moves.

Also, for an ideal gas the equation of state becomes

$$e = \frac{p}{\gamma - 1} + \frac{1}{2}\rho(u^2 + v^2), \tag{2.8}$$

where γ is the ratio of specific heats.

2.1.2 Nonlinear Model

The governing equations are discretised using a finite volume formulation on an unstructured triangular grid covering the computational domain and approximations to the unknown flow vector W are sought at the vertices of that grid. For an interior vertex j, equation (2.5) can be written

$$\frac{d}{dt}(V_j W_j) + \int_{\Gamma_j} (F n_x + G n_y) d\Gamma = 0, \tag{2.9}$$

where V_j is the volume consisting of all the triangles having vertex j as shown in Figure 2-4, Γ_j is the boundary of V_j and W_j represents the average value of W over volume V_j. The integral in equation (2.9) is evaluated by considering weighted summations of flux differences across each edge in the control volume [63]. At boundary vertices, some of the flow variables are prescribed via appropriate boundary conditions. These prescribed quantities are contained within the vector $\mathbf{U}_b$, while the unknown flow quantities are contained in the vector $\mathbf{U}$. For interior nodes the components of the unknown vector $\mathbf{U}$ are the conservative flow variables (2.6), while for boundary nodes a transformation to other appropriate flow quantities is performed. The particular transformation depends on which flow quantities are specified via the boundary conditions at that node. For example, at a point j on the blade surface, the normal velocity must be specified. At that node, we therefore perform a transformation from the conservative variables (2.6) to boundary condition-specific variables given by

$$\tilde{W}_j = (\rho, u_n, u_t, p)_j^T, \tag{2.10}$$

where u_n and u_t are the normal and tangential velocities respectively. The prescribed variable $(u_n)_j$ will be contained in the vector $\mathbf{U}_b$, while the unknowns $\rho_j, (u_t)_j$ and p_j will be contained in the vector $\mathbf{U}$. Similar transformations are performed at the passage inlet and exit according to the particular boundary condition.

Evaluation of (2.9) at each node combined with appropriate variable transformations leads to a large set of nonlinear ordinary differential equations for the unknown flow vector $\mathbf{U}$ which can be written

as

$$\frac{d\mathbf{U}}{dt} + \mathbf{R}(\mathbf{U}, \mathbf{U}_b, \mathbf{x}) = 0, \tag{2.11}$$

where $\mathbf{R}(\mathbf{U}, \mathbf{U}_b, \mathbf{x})$ represents the nonlinear flux contributions which are a function of the problem geometry $\mathbf{x}$, the flow solution $\mathbf{U}$ and the boundary conditions $\mathbf{U}_b$. We consider unsteady motion in which each blade can move with two degrees of freedom, although in general, blade shape deformations could also be included. For blade i the bending displacement (plunge) is denoted by h_i and torsion about an elastic axis (pitch) by α_i. The grid geometry $\mathbf{x}$ depends directly on the positions of the individual blades, that is for r blades

$$\mathbf{x} = \mathbf{x}(h_1, \alpha_1, h_2, \alpha_2, ..., h_r, \alpha_r). \tag{2.12}$$

At the passage inlet and exit we allow external flow disturbances. These could be, for example, time-varying pressure or velocity distortions which may be due to a neighbouring blade row or to an inhomogeneity in the incoming flow. Given blade motion $\mathbf{q}$ and disturbance $\mathbf{d}$, the boundary conditions can be written as

$$\mathbf{U}_b = \mathbf{U}_p(\mathbf{q}, \dot{\mathbf{q}}, \mathbf{d}, \mathbf{x}), \tag{2.13}$$

where $\mathbf{q}$ is a vector containing the plunge and pitch displacements for each blade

$$\mathbf{q}_i = [h_i \;\; \alpha_i]^T. \tag{2.14}$$

In (2.13), $\mathbf{U}_p$ is the vector containing the prescribed values of the boundary condition flow variables at each instant in time. In general, these values will depend on the instantaneous blade positions and velocities, the external flow disturbance and the instantaneous grid position.

We define outputs of interest in the vector $\mathbf{y}$. These could be any feature of the flow field, but typically are the aerodynamic forces and moments acting on each blade and perhaps the unsteady flow at the passage inlet and exit. The nonlinear CFD model can be summarised as

$$\begin{aligned} \frac{d\mathbf{U}}{dt} + \mathbf{R}(\mathbf{U}, \mathbf{U}_b, \mathbf{x}) &= 0, \\ \mathbf{U}_b &= \mathbf{U}_p(\mathbf{q}, \dot{\mathbf{q}}, \mathbf{d}, \mathbf{x}), \\ \mathbf{y} &= \mathbf{y}(\mathbf{U}, \mathbf{U}_b, \mathbf{x}). \end{aligned} \tag{2.15}$$

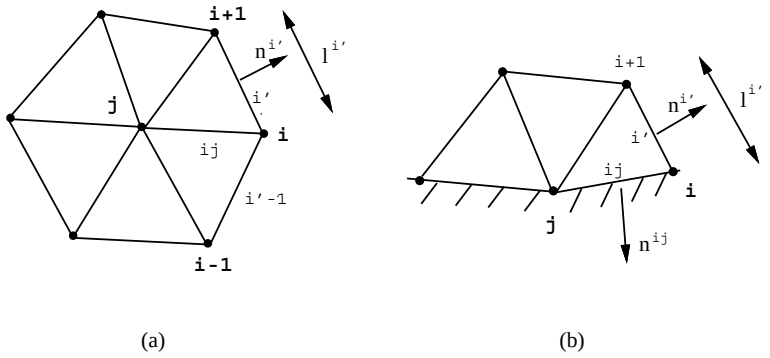

Figure 2-4: Control volume V_j associated to a generic node j of an unstructured grid (a) Interior node, (b) Boundary node.

Steady-state solutions can be evaluated by driving the nonlinear residual $\mathbf{R}(\mathbf{U}, \mathbf{U}_b, \mathbf{x})$ in (2.15) to zero. This is done by implementation of a Newton scheme coupled with an iterative GMRES solver [62]. Assuming subsonic conditions, the density, total enthalpy and tangential velocity are prescribed at the inlet boundary and the exit pressure is specified. At the blade surfaces, a flow tangency condition is applied to the velocity. For steady-state flows in which the solution is the same in all passages, the computation can be performed on a single blade passage with use of appropriate periodic boundary conditions as shown in Figure 2-5.

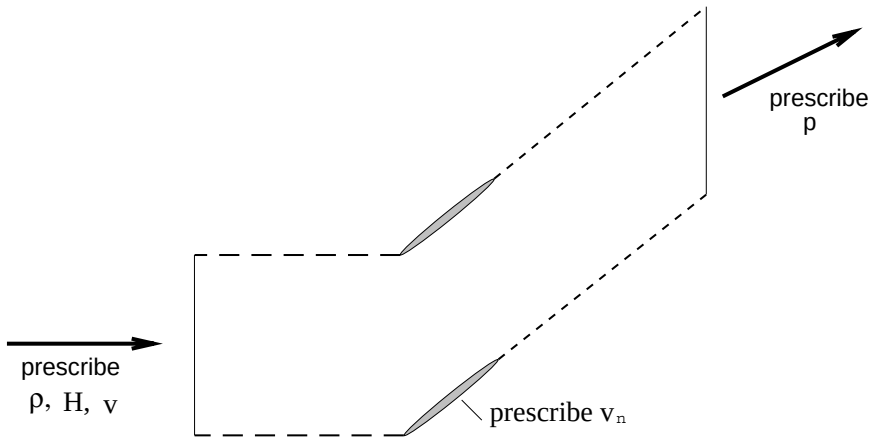

Figure 2-5: Computational domain for solution of steady-state flow. Boundary conditions are applied at blade surfaces and passage inlet and exit. Periodic conditions are applied at dashed boundaries. Inlet and exit boundary conditions shown assume subsonic axial flow.

2.1.3 Linearised Model

For consideration of unsteady flows, caused by unsteady disturbances in the passage or by blade motion, the full nonlinear equation (2.15) could be integrated in time. This procedure is computationally expensive, especially if the disturbances considered have circumferential variation. If we limit ourselves to the consideration of small amplitude unsteady motions, the problem can be considerably simplified by linearising the equations. We assume that the unsteady flow and grid geometry are small perturbations about a steady state

$$\begin{aligned} \mathbf{U}(\mathbf{x},t) &= \overline{\mathbf{U}}(\mathbf{x}) + \mathbf{U}'(\mathbf{x},t), \\ \mathbf{U}_b(\mathbf{x},t) &= \overline{\mathbf{U}}_b(\mathbf{x}) + \mathbf{U}'_b(\mathbf{x},t), \\ \mathbf{x}(t) &= \overline{\mathbf{x}} + \mathbf{x}'(t). \end{aligned} \tag{2.16}$$

Additionally, we assume that the unsteady forcing terms $\mathbf{q}$, $\dot{\mathbf{q}}$ and $\mathbf{d}$ are small. Performing a Taylor expansion about steady-state conditions, the nonlinear residual in (2.15) can be written

$$\mathbf{R}(\mathbf{U},\mathbf{U}_b,\mathbf{x}) \simeq \mathbf{R}(\overline{\mathbf{U}},\overline{\mathbf{U}}_b,\overline{\mathbf{x}}) + \frac{\partial \mathbf{R}}{\partial \mathbf{U}}(\overline{\mathbf{U}},\overline{\mathbf{U}}_b,\overline{\mathbf{x}})\mathbf{U}' + \frac{\partial \mathbf{R}}{\partial \mathbf{U}_b}(\overline{\mathbf{U}},\overline{\mathbf{U}}_b,\overline{\mathbf{x}})\mathbf{U}'_b + \frac{\partial \mathbf{R}}{\partial \mathbf{x}}(\overline{\mathbf{U}},\overline{\mathbf{U}}_b,\overline{\mathbf{x}})\mathbf{x}'. \tag{2.17}$$

Using the fact that $\mathbf{R}(\overline{\mathbf{U}},\overline{\mathbf{U}}_b,\overline{\mathbf{x}}) = 0$ and neglecting quadratic and higher order terms in $\mathbf{U}'$, $\mathbf{U}'_b$ and $\mathbf{x}'$, the linearised form of equation (2.15) is

$$\frac{d\mathbf{U}'}{dt} + \frac{\partial \mathbf{R}}{\partial \mathbf{U}}\mathbf{U}' + \frac{\partial \mathbf{R}}{\partial \mathbf{U}_b}\mathbf{U}'_b + \frac{\partial \mathbf{R}}{\partial \mathbf{x}}\mathbf{x}' = 0, \tag{2.18}$$

where all derivatives are evaluated at steady-state conditions. Note that due to the linear assumption, the grid is not actually deformed for unsteady calculations, however the final term on the left-hand side of equation (2.18) represents the first-order effects of grid motion. Likewise, the boundary conditions can be linearised to obtain

$$\mathbf{U}'_b = \frac{\partial \mathbf{U}_p}{\partial \mathbf{q}}\mathbf{q} + \frac{\partial \mathbf{U}_p}{\partial \dot{\mathbf{q}}}\dot{\mathbf{q}} + \frac{\partial \mathbf{U}_p}{\partial \mathbf{d}}\mathbf{d} + \frac{\partial \mathbf{U}_p}{\partial \mathbf{x}}\mathbf{x}'. \tag{2.19}$$

We can further simplify the system by condensing $\mathbf{U}'_b$ out of (2.18) using (2.19) and writing the grid displacement as a linear function of blade displacement

$$\mathbf{x}' = \mathcal{T}\mathbf{q}, \tag{2.20}$$

where $\mathcal{T}$ is a constant transformation matrix. The final set of ordinary differential equations then becomes

$$\frac{d\mathbf{U}'}{dt} + \frac{\partial \mathbf{R}}{\partial \mathbf{U}}\mathbf{U}' = \left(-\frac{\partial \mathbf{R}}{\partial \mathbf{x}}\mathcal{T} - \frac{\partial \mathbf{R}}{\partial \mathbf{U}_b}\frac{\partial \mathbf{U}_p}{\partial \mathbf{q}} - \frac{\partial \mathbf{R}}{\partial \mathbf{U}_b}\frac{\partial \mathbf{U}_p}{\partial \mathbf{x}}\mathcal{T} \right) \mathbf{q} - \frac{\partial \mathbf{R}}{\partial \mathbf{U}_b}\frac{\partial \mathbf{U}_p}{\partial \dot{\mathbf{q}}}\dot{\mathbf{q}} - \frac{\partial \mathbf{R}}{\partial \mathbf{U}_b}\frac{\partial \mathbf{U}_p}{\partial \mathbf{d}}\mathbf{d}, \quad (2.21)$$

which can be written equivalently as

$$\frac{d\mathbf{U}'}{dt} = \mathcal{A}\mathbf{U}' + \mathcal{B}\mathbf{u} + \mathcal{E}\mathbf{d}. \quad (2.22)$$

Here $\mathbf{u} = [\mathbf{q}\ \dot{\mathbf{q}}]^T$ is the blade motion input vector containing the displacement and velocity of each blade, and the matrices $\mathcal{B}$ and $\mathcal{E}$ contain the appropriate forcing terms of equation (2.21).

It would be possible to include further sensitivities in the linearisation of the governing equations. For example, one could consider small variations in the inlet flow Mach number about a nominal value M_0. We would then include a term of the form

$$\frac{\partial \mathbf{R}}{\partial M}(\overline{\mathbf{U}}, \overline{\mathbf{U}}_b, \overline{\mathbf{x}}, M_0)(M - M_0). \quad (2.23)$$

in equation (2.18). Sensitivities to airfoil shape or other flow parameters could be included in a similar way.

To determine the unsteady response of the cascade, the blade motion inputs $\mathbf{u}(t)$ and the external disturbance $\mathbf{d}(t)$ are specified and the large system (2.22) is time-marched to determine the resulting flow. The outputs of interest can be written as a linear function of the flow perturbation $\mathbf{U}'$. The linearised CFD model can be summarised as

$$\begin{aligned} \frac{d\mathbf{U}'}{dt} &= \mathcal{A}\mathbf{U}' + \mathcal{B}\mathbf{u} + \mathcal{E}\mathbf{d}, \\ \mathbf{y} &= \mathcal{C}\mathbf{U}', \end{aligned} \quad (2.24)$$

and compared to the nonlinear formulation (2.15). In the above, $\mathcal{C}$ is a matrix, typically a function of the problem geometry and the mean flow conditions, which defines the outputs of interest. For example, if $\mathbf{y}$ contains the forces and moments acting on each blade, then $\mathcal{C}$ contains the geometric and mean flow contributions to the linearised force calculation. It is possible that the outputs may also depend explicitly on the blade motion and external disturbance, in which case the definition of $\mathbf{y}$ in (2.24) will also include terms of the form $\mathcal{D}\mathbf{u}$ and $\mathcal{F}\mathbf{d}$. However, all outputs considered in this

research (blade forces and outgoing flow perturbations at the passage inlet and exit) are defined by (2.24).

2.1.4 Linearised Boundary Conditions

At the passage inlet and exit, the incoming one-dimensional characteristic quantities are evaluated in terms of perturbations in the inlet and exit flows as follows. At the inlet prescribe entropy, vorticity and downstream running pressure waves which are given respectively by

$$\begin{aligned} c_1 &= p' - \overline{c}^2 \rho', \\ c_2 &= \overline{\rho}\ \overline{c}\ u'_t, \\ c_3 &= p' - \overline{\rho}\ \overline{c}\ u'_n. \end{aligned} \tag{2.25}$$

At the outflow boundary prescribe the upstream running pressure wave given by

$$c_3 = p' - \overline{\rho}\ \overline{c}\ u'_n. \tag{2.26}$$

Here, u'_n and u'_t are the normal and tangential components of perturbation velocity (note that the normal is always defined to point out of the domain), and $\overline{c}$ is the speed of sound of the steady-state flow. It would also be possible to use more sophisticated models for the inlet and exit boundary conditions [15].

On the blade surfaces, the normal velocity is prescribed to be equal to the value induced by the blade motion, v_n^{pr}. This can be written

$$\mathbf{v}'.\overline{\mathbf{n}} = v_n^{pr} - \overline{\mathbf{v}}.\mathbf{n}', \tag{2.27}$$

where $\mathbf{v} = [u\ \ v]^T$ is the vector of cartesian velocity components and $\mathbf{n} = \overline{\mathbf{n}} + \mathbf{n}'$ is the instantaneous position of the surface normal vector. Note the two contributions in (2.27). The term v_n^{pr} which contains the blade motion will depend on the blade velocities $\dot{h}_j$ and $\dot{\alpha}_j$, while the second term contains the perturbation to the normal vector, $\mathbf{n}'$, which depends on blade rotational displacement α_j.

2.1.5 Modal Analysis

Due to the fact that for small perturbation analysis the governing equations (2.24) are linear, any general farfield disturbance or blade motion can be decomposed into a summation of circumferential travelling wave components containing just a single spatial frequency, and each of these modes can be considered separately. Moreover, the temporal variation of the forcing can be viewed as a superposition of harmonic components. By superposing these spatial and temporal modes, any arbitrary disturbance in space and time may be represented. The response due to each of these modes can be computed separately and then recombined appropriately to obtain the overall response to the general forcing function.

Consider first the motion of r blades given by

$$\mathbf{u}(t) = [\mathbf{u}_1^T(t)\ \mathbf{u}_2^T(t)\ \ \ldots\ \ \mathbf{u}_r^T(t)]^T. \tag{2.28}$$

Due to the circumferential nature of the problem, there exist within this motion discrete allowable values of spatial frequency σ_j. Moreover, due to the discrete nature of the blades, the blade motion contains a finite number of spatial modes. For a bladed disk with r blades, there are just r possible modes, with spatial frequencies given by

$$\sigma_j = \frac{2\pi j}{r} \qquad\qquad j = 0, 1, 2, \ldots, r-1. \tag{2.29}$$

Here, σ_j is known as the interblade phase angle and describes the phase difference between the motion of a given blade and its neighbour [21].

A general motion of the blades (2.28) can be decomposed into its spatial modes by performing a discrete Fourier transform. If we denote the complex magnitude of the modal component corresponding to σ_j by $\overline{\mathbf{u}}_j$, then for blade n we can write

$$\mathbf{u}_n(t) = Re\left\{\sum_{j=0}^{r-1} \overline{\mathbf{u}}_j(t) e^{i(n-1)\sigma_j}\right\}. \tag{2.30}$$

The transformation from blade coordinates $\mathbf{u}$ to interblade phase angle coordinates $\overline{\mathbf{u}}$ can therefore be written

$$\mathbf{u}(t) = Re\left\{P\overline{\mathbf{u}}(t)\right\}, \tag{2.31}$$

where the components of P are given by (2.30):

$$P_{nj} = e^{i(n-1)\sigma_j}. \tag{2.32}$$

A similar decomposition can be performed for a general inlet or exit disturbance. Still the discrete values of σ_j defined by (2.29) are the only ones allowable (to satisfy circumferential periodicity), but now an infinite number of spatial modes may be present, that is j can take any integer value. The Fourier transform for a disturbance $\mathbf{d}$ can therefore be written

$$\mathbf{d}(t) = Re\left\{\sum_{j=-\infty}^{\infty} \overline{\mathbf{d}}_j(t) e^{i\sigma_j}\right\}. \tag{2.33}$$

Similarly, the time-varying component of blade motion and disturbance forcing can be decomposed into temporal frequency components. In this case, an infinite number of possible frequencies exists. Thus, a motion $\mathbf{u}$ can be represented as

$$\mathbf{u}(t) = Re\left\{\int_{-\infty}^{\infty} \overline{\mathbf{u}}(\omega) e^{i\omega t} d\omega\right\}. \tag{2.34}$$

In practice, discrete values of temporal frequency are chosen, so that the blade motion can be represented as a summation over temporal and spatial modes. If m temporal frequencies are selected, then the motion of blade n can be written as

$$\mathbf{u}_n(t) = Re\left\{\sum_{k=1}^{m}\sum_{j=0}^{r-1} \overline{\mathbf{u}}_{jk} e^{i(\omega_k t + (n-1)\sigma_j)}\right\}. \tag{2.35}$$

A similar expression can be written for the disturbance. With m temporal frequencies and l spatial frequencies, we obtain

$$\mathbf{d}(t) = Re\left\{\sum_{k=1}^{m}\sum_{j=0}^{l-1} \overline{\mathbf{d}}_{jk} e^{i(\omega_k t + \sigma_j)}\right\}. \tag{2.36}$$

Assuming decompositions of the form (2.35) and (2.36) have been performed on the forcing functions, we can now consider each modal component separately. Consider then a blade motion $\mathbf{u}^{jk}$ containing a single temporal frequency ω_k and single spatial frequency σ_j. The motion of any blade n can be written in terms of the motion of the first blade as

$$\mathbf{u}_n^{jk}(t) = \mathbf{u}_1^{jk}(t) e^{i(n-1)\sigma_j}, \tag{2.37}$$

where also from (2.35)

$$\mathbf{u}_1^{jk}(t) = \overline{\mathbf{u}}_{jk}(t)e^{i\omega_k t}. \tag{2.38}$$

The corresponding flow solution in each passage will also be harmonic of the form

$$\mathbf{U}_n^{jk}(t) = \overline{\mathbf{U}}_{jk}e^{i\omega_k t}e^{i(n-1)\sigma_j}, \tag{2.39}$$

with the same spatial frequency σ_j because all blades have the same aerodynamic shape and so the jth spatial forcing only excites the jth spatial aerodynamic response. Here the vector $\mathbf{U}_n$ represents the unknown perturbation flow variables associated with blade n. Since each $\overline{\mathbf{U}}_{jk}$ contains a single spatial frequency, if the response of the first blade is known, then the response of all subsequent blades can be determined by using (2.39). The governing equations can therefore be discretised on a single blade passage making the computation much more efficient than a time domain calculation.

Analogous relations can be written for each modal component of $\mathbf{d}$, and the linearised Euler equations (2.24) can now be cast in the frequency domain on a single passage as

$$[i\omega_k - \mathcal{A}_j]\,\overline{\mathbf{U}}_{jk} = \mathcal{B}\overline{\mathbf{u}}_{jk} + \mathcal{E}\overline{\mathbf{d}}_{jk}, \tag{2.40}$$

where $\mathcal{A}_j$ represents the original matrix $\mathcal{A}$ for just one passage, but modified to allow for a complex periodicity condition. This condition enforces the fact that the flow along the upper periodic boundary is the same as that along the lower periodic boundary but phase shifted by the spatial frequency σ_j. Equation (2.40) is solved using a complex GMRES algorithm. The system is preconditioned by computing an incomplete LU factorisation of the matrix $\mathcal{A}_j$. An outline of the GMRES algorithm is given in Appendix A.

The solution procedure can be summarised as follows: a general blade motion and disturbance forcing are decomposed into temporal and spatial harmonics. The frequency domain CFD equations (2.40) are solved on a single passage for each ω_k, σ_j pair to obtain the component of the response $\overline{\mathbf{U}}_{jk}$ in the first passage. These components could then be recombined using a relation of the form (2.35) to to obtain the overall response in each passage to the complete forcing.

2.2 CFD Model Validation

In this section two cases are presented for validation of the non-linear steady-state CFD model, one subsonic and one transonic. The unsteady linearised solver is validated against experimental data

for a subsonic cascade.

2.2.1 UTRC Low-Speed Cascade

The non-linear steady-state CFD code was validated against experimental data for a low-speed UTRC blade which is documented in [26]. The computational steady-state grid is shown in Figure 2-6 and has 2541 nodes per blade passage. The blunt trailing edge of this blade has been made sharp by linearly tapering the blade thickness, The inlet Mach number is 0.113 at an angle of 38°. Figure 2-7 shows a good agreement between the experimental data and the calculated pressure coefficient along the upper and lower surfaces of the blade. The higher calculated pressure at the trailing edge is mainly due to the increase in flow area from the sharpening of the trailing edge.

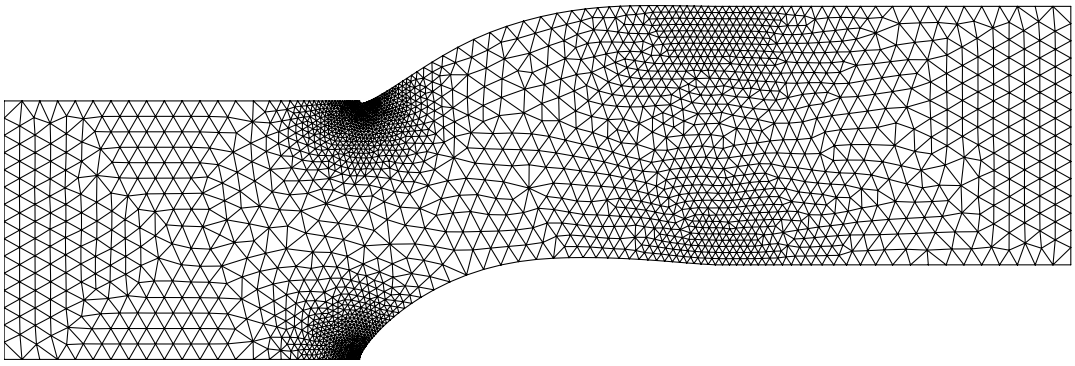

Figure 2-6: CFD grid for UTRC subsonic blade. 2541 points, 4817 triangles.

2.2.2 DFVLR Transonic Cascade

The DFVLR cascade is an experimental cascade set up to analyse the flow in a two-dimensional low turning cascade at transonic and low supersonic inlet Mach numbers. The computational domain for a single passage is shown in Figure 2-8. The case selected for analysis here has a steady-state flow with an inlet Mach number of 0.82 at a relative flow angle of 58.5°. The pressure contours of the steady-state solution for this problem are shown in Figure 2-9. The steady-state pressure coefficient calculated along the blade compared well with experiment and is shown in Figure 2-10.

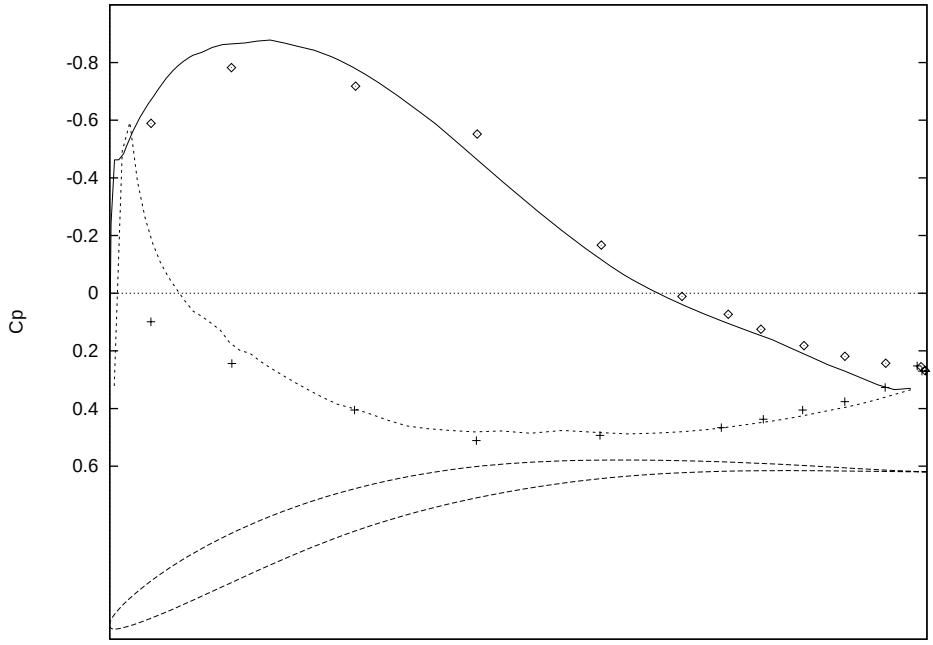

Figure 2-7: Pressure distribution for UTRC subsonic blade, experimental data (points) and CFD results (lines). $M = 0.113, \beta = 38°$.

2.2.3 First Standard Configuration

The standard configurations were established to provide a database of well documented experimental data for aeroelastic analysis of turbomachines [1]. The first standard configuration is a low subsonic compressor stage and is shown in Figure 2-11 along with the pressure coefficient distributions on the top and bottom surfaces. The stagger angle of the blades is 55° and the inlet Mach number is 0.18 at an angle of $-66°$. The cascade was analysed in sinusoidal pitching motion $\alpha = \overline{\alpha} e^{i\omega t}$ where the magnitude of the oscillations is $\overline{\alpha} = 1°$ and ω is defined in terms of the reduced frequency

$$k = \frac{\omega c}{V}, \tag{2.41}$$

where c is the blade chord length and V is the inlet flow velocity. For the results presented here, the reduced frequency is $k = 0.122$.

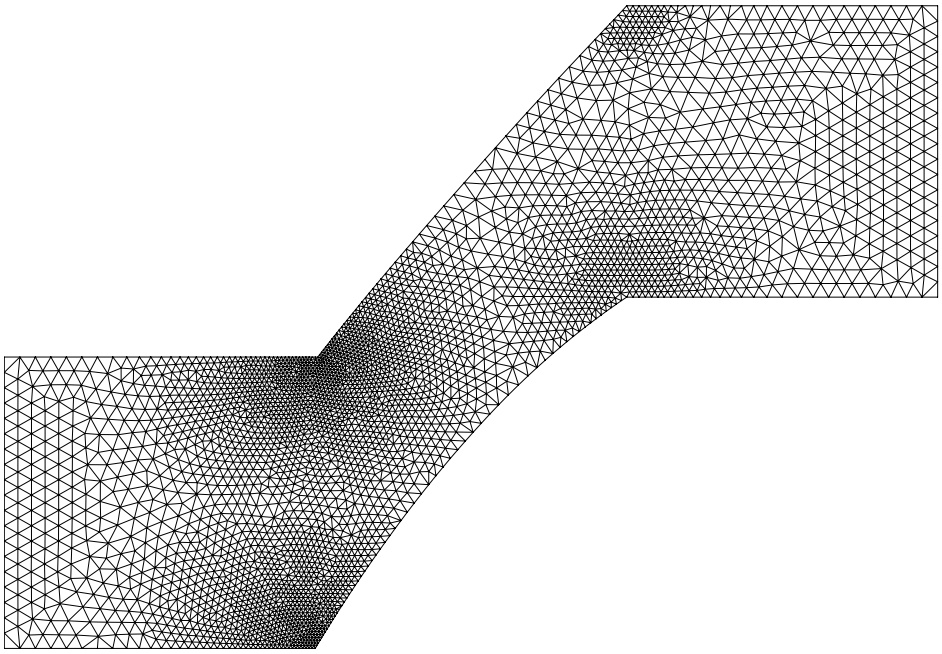

Figure 2-8: CFD grid for DFVLR transonic rotor. 3668 points, 7040 triangles.

The aerodynamic work per cycle is a measure of the energy transferred from the fluid to the structure in one oscillation period of sinusoidal motion and is given by

$$W_h = \oint L.dh \tag{2.42}$$

for bending vibrations and

$$W_\alpha = \oint M_{ea}.d\alpha \tag{2.43}$$

for torsional vibrations. Here, L is the aerodynamic force, M_{ea} is the moment acting about the elastic axis and the integral is over one oscillation period of the blade. The work per cycle quantities can be used to assess the stability of an aeroelastic system. If the work per cycle is positive, then there is a negative amount of damping being applied to the structure and the system is unstable. Negative but low in magnitude values of work per cycle indicate that a system is stable but lightly damped. In [1] the corresponding aerodynamic damping coefficients are defined as

$$\Xi_h = -\frac{W_h}{\pi |h|^2} \tag{2.44}$$

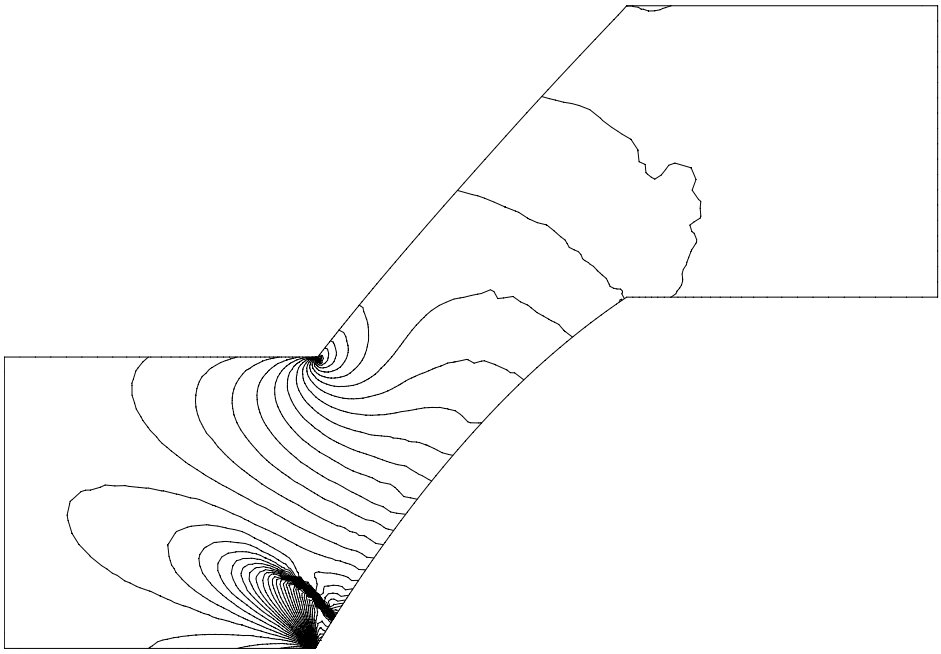

Figure 2-9: Steady-state pressure contours for DFVLR transonic rotor. $M = 0.82$, $\alpha = 58.5°$.

and

$$\Xi_\alpha = -\frac{W_\alpha}{\pi|\alpha|^2}. \tag{2.45}$$

The aerodynamic damping was evaluated as a function of interblade phase angle using the CFD analysis and is plotted in Figure 2-12 along with the experimental data from [1]. The aeroelastic force coefficients were determined experimentally as the transfer functions between the imposed vibratory motion and the measured lift or moment. The imaginary part of these coefficients is a measure of the aeroelastic damping. Figure 2-12 shows a good correlation with the experimental data. The agreement obtained is much better than that shown in [1] for other analytic and computational methods.

2.3 Structural Model

So far the computational model for the aerodynamic governing equations has been presented. In (2.2), we also require a model which describes the evolution of the structural states. This could be a

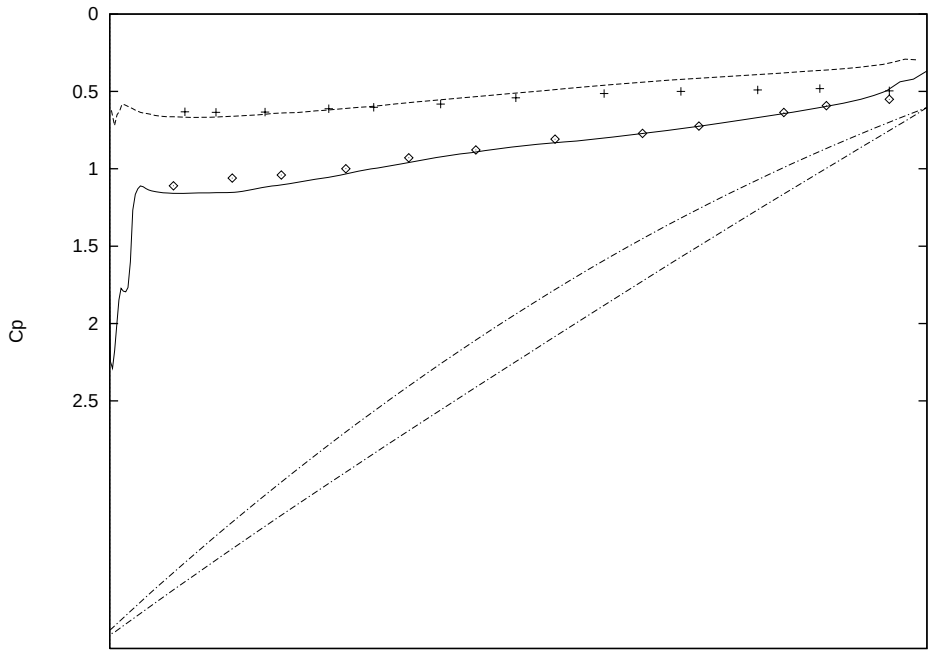

Figure 2-10: Pressure distribution for DFVLR transonic blade, experimental data (points) and CFD results (lines). $M = 0.82, \beta = 58.5°$.

complicated model, such as a finite element analysis which describes the general deformations of each blade, or a simple model such as a low-order mass-spring system. Here, each blade is allowed just two structural degrees of freedom (pitch and plunge). The structural equations governing this motion can be derived by considering a simple mass-spring-damper model with two degrees of freedom as shown in Figure 2-13. For a blade with mass per unit length m and chord c, the equations of motion can be written in non-dimensional form as

$$\begin{bmatrix} \mathcal{M}_1 & 0 & . & . & 0 \\ 0 & \mathcal{M}_2 & 0 & . & 0 \\ . & . & . & . & . \\ . & . & . & . & . \\ 0 & . & . & 0 & \mathcal{M}_r \end{bmatrix} \begin{bmatrix} \ddot{\mathbf{q}}_1 \\ \ddot{\mathbf{q}}_2 \\ . \\ . \\ \ddot{\mathbf{q}}_r \end{bmatrix} + \begin{bmatrix} C_1 & 0 & . & . & 0 \\ 0 & C_2 & 0 & . & 0 \\ . & . & . & . & . \\ . & . & . & . & . \\ 0 & . & . & 0 & C_r \end{bmatrix} \begin{bmatrix} \dot{\mathbf{q}}_1 \\ \dot{\mathbf{q}}_2 \\ . \\ . \\ \dot{\mathbf{q}}_r \end{bmatrix}$$

$$+ \begin{bmatrix} K_1 & 0 & . & . & 0 \\ 0 & K_2 & 0 & . & 0 \\ . & . & . & . & . \\ . & . & . & . & . \\ 0 & . & . & 0 & K_r \end{bmatrix} \begin{bmatrix} \mathbf{q}_1 \\ \mathbf{q}_2 \\ . \\ . \\ \mathbf{q}_r \end{bmatrix} = \begin{bmatrix} \mathbf{L}_1 \\ \mathbf{L}_2 \\ . \\ . \\ \mathbf{L}_r \end{bmatrix}, \tag{2.46}$$

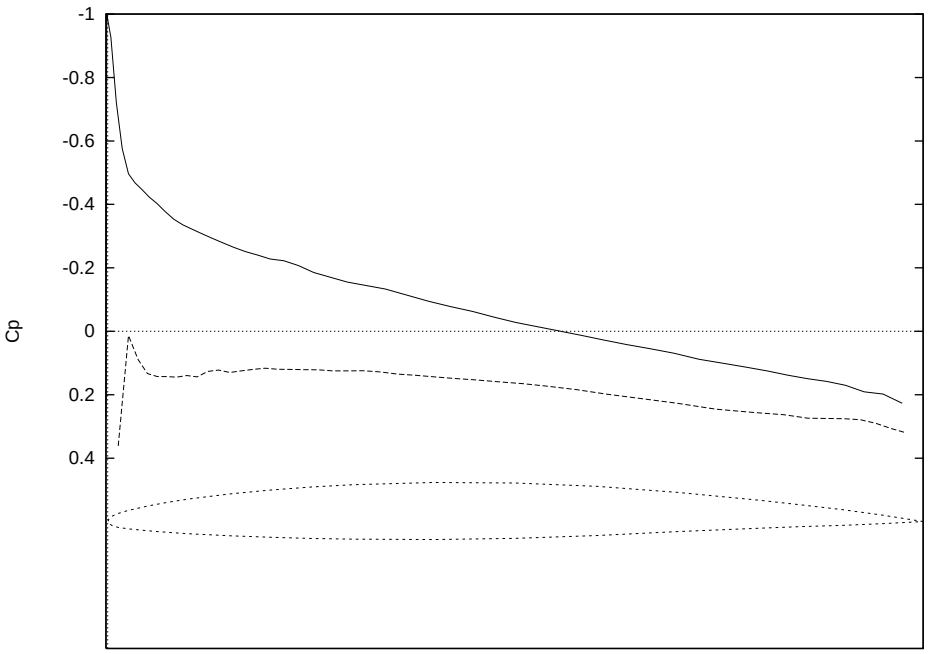

Figure 2-11: First standard configuration blade pressure distribution: $M = 0.18$, $\beta = -66°, \gamma = 55°$.

where $[\mathcal{M}_i]$, $[C_i]$ and $[K_i]$ are the non-dimensional mass, damping and stiffness matrices for each blade i and are given by

$$[\mathcal{M}_i] = \begin{bmatrix} 1 & x_\alpha \\ x_\alpha & r_\alpha^2 \end{bmatrix}_i, [C_i] = \begin{bmatrix} 2kM\zeta & 0 \\ 0 & 2kM\zeta\left(\frac{\omega_h}{\omega_\alpha}\right) r_\alpha \end{bmatrix}_i, [K_i] = \begin{bmatrix} k^2M^2 & 0 \\ 0 & k^2M^2\left(\frac{\omega_h}{\omega_\alpha}\right)^2 r_\alpha^2 \end{bmatrix}_i. \quad (2.47)$$

Here ω_h and ω_α are the uncoupled natural frequencies of the blade in plunge and pitch respectively, ζ is the structural damping coefficient, x_α is the non-dimensional distance of the centre of gravity from the elastic axis, and r_α is the radius of gyration about the elastic axis. The reduced frequency is defined in terms of the plunge natural frequency, $k = \frac{\omega_h c}{V}$, and the load vector for each blade is

$$\mathbf{L}_i = \frac{2M^2}{\pi\mu} \begin{bmatrix} -C_l^i \\ C_m^i \end{bmatrix}, \quad (2.48)$$

where C_l^i is the lift coefficient for blade i and C_m^i is the moment coefficient about the aerodynamic centre which is located a distance a chord lengths in front of the elastic axis. M is the inlet Mach number and μ is the blade mass ratio given by

$$\mu = \frac{4m}{\pi\rho c^2}. \quad (2.49)$$

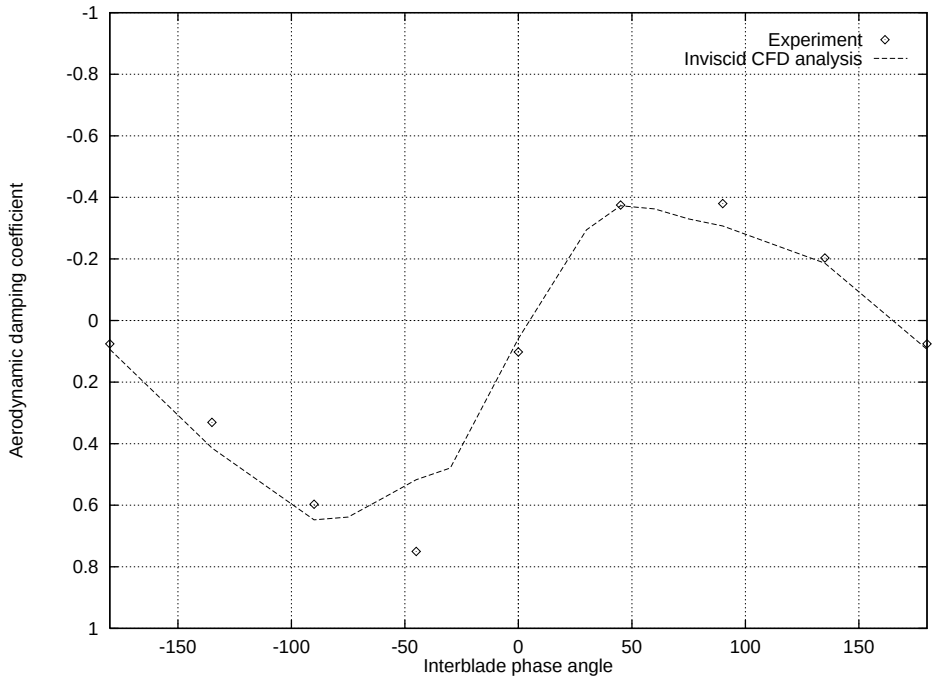

Figure 2-12: First standard configuration: torsional aerodynamic damping coefficient as a function of interblade phase angle. $M = 0.18, \beta = -66°, k = 0.122$.

By using the identities $\frac{dh_j}{dt} = \dot{h}_j$ and $\frac{d\alpha_j}{dt} = \dot{\alpha}_j$, the structural system (2.46) can be written as a first order system as follows

$$\frac{d\mathbf{u}}{dt} = S\mathbf{u} + T\mathbf{y}, \tag{2.50}$$

where $\mathbf{u}_i = [\mathbf{q}_i \ \dot{\mathbf{q}}_i]$ as in the aerodynamic system (2.24), $\mathbf{y}$ contains the aerodynamic force and moment coefficients for each blade, and the matrices S and T follow from (2.46). We note that in reality, the rotation of the rotor will affect the structural system as defined in (2.46). However, for the purpose of this simple structural analysis, this will be ignored.

2.4 Coupled Aerodynamic/Structural Model

Equation (2.50) shows the coupling between the aerodynamic and structural models. To determine the structural states, it is necessary to know the instantaneous aerodynamic forces and moments acting. These forces depend on the aerodynamics states, which in turn require the blade motion $\mathbf{u}$

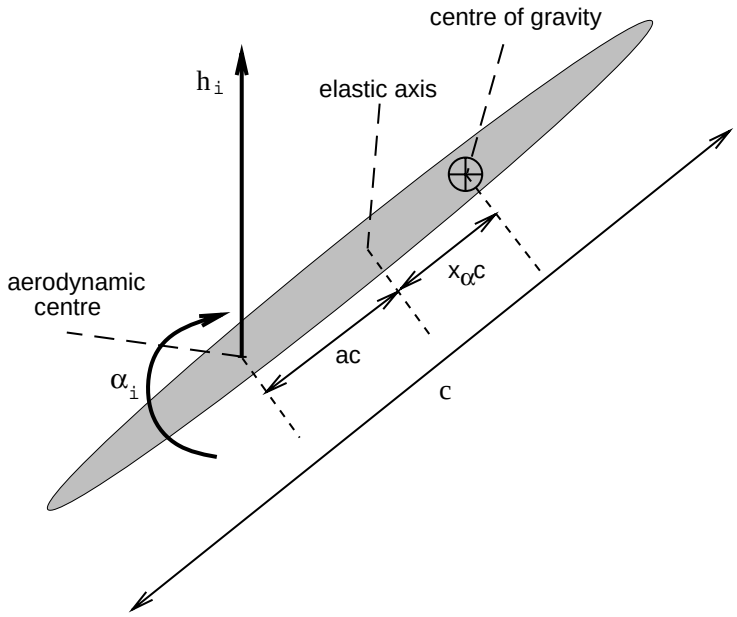

Figure 2-13: Typical section structural model for blade i.

as input to equation (2.24). The coupled aerodynamic/structural system can be written as

$$\begin{bmatrix} \dot{\mathbf{U}}' \\ \dot{\mathbf{u}} \end{bmatrix} = \begin{bmatrix} \mathcal{A} & \mathcal{B} \\ T\mathcal{C} & S \end{bmatrix} \begin{bmatrix} \mathbf{U}' \\ \mathbf{u} \end{bmatrix} + \begin{bmatrix} \mathcal{E} \\ 0 \end{bmatrix} \mathbf{d}. \tag{2.51}$$

At each timestep the external disturbance $\mathbf{d}$ could be specified and the structural and aerodynamic equations solved simultaneously to determine the system forced response. Equation (2.51) can also be used to investigate stability properties by determining the eigenvalues of the unforced coupled system. Since a simple structural model was considered, there are only four structural states per blade. However, the CFD model describing the aerodynamics has tens of thousands of states per blade passage (four unknowns for every point in the computational domain). Although the system (2.51) describes the aerodynamics well, it is very large and not well suited to aeroelastic analysis. In the next chapter alternative low-order aerodynamic models will be discussed.

Chapter 3

Reduced-Order Aerodynamic Modelling

While the CFD model described in the previous section provides an accurate representation of the flow aerodynamics, the set of ordinary differential equations obtained is extremely large. There are four unknowns at each grid point in the computational domain, so the system size is typically of the order of tens of thousands of unknowns per blade passage. The aeroelastic model (2.51) is so large that it is not at all well suited to stability analysis or to control design. It is therefore desirable to develop a model which still provides an accurate description of the relevant system aerodynamics but which has only a few states. Such a model would not only be efficient for solving unsteady flow problems, but would also provide an excellent framework for coupling with global engine models and for control design.

Low-order models have been proposed that fall into essentially two categories. The first is to obtain a model by making simplifying assumptions about the physics of the problem. For example, the flow may be assumed to be incompressible and two-dimensional, while the blades can be regarded as flat plates. These assumptions lead to low-order actuator-disc methods which can be solved analytically, such as that developed in [59]. While the simplified-physics models often provide insight to a given problem, and have been widely used, the assumptions involved are generally very restrictive. More general models can be obtained via the second approach which involves model order reduction of a high-order CFD method. Within this category, there are again two possibilities. The first is to simplify the CFD model by computing the system response at particular flow conditions. The overall

response is then characterised in terms of constant coefficients which represent the CFD solution at these assumed conditions but which are used to provide the aerodynamic model for all flows. These methods are referred to as "assumed-frequency" or "influence coefficient" models. Alternatively, one can systematically reduce the order of CFD method by projecting it onto a reduced-order subspace, thus restricting its range of validity. In some sense, the assumed-frequency methods are a subset of this approach, since by restricting the CFD model to a single flow condition, they compute a model of the lowest possible order (constant coefficients). The idea of systematic model order reduction is to increase the number of states in the low-order model thereby preserving a larger range of validity.

Aerodynamic influence coefficient models have been used in many turbomachinery aeroelastic applications, for example in [10, 7, 8, 33]. The response is calculated from a CFD model by imposing sinusoidal motion on the blade at a particular frequency (often the blade natural frequency). These aerodynamics are then assumed to represent the system for all flows. In practice, a significant amount of coupling often exists between the flow and the structure, as will be demonstrated in this chapter by some typical examples. In this case the blade response will contain a range of frequencies and an influence coefficient model cannot accurately represent the system dynamics. Instead, a high-fidelity, low-order model which is valid over a range of frequencies can be obtained by projecting the CFD model onto a set of basis vectors. These vectors are chosen carefully so that the relevant system dynamics can be well represented with a small number of states; the "efficiency" of the model can be characterised by the number of states required to accurately capture the relevant dynamics. Reduced-order models developed in this manner can be easily cast into state-space form and hence lend themselves naturally to control design problems.

An influence coefficient model derived from the linearised CFD model of Chapter 2 will be presented in this chapter, along with some other options for constructing reduced-order models. There are several alternatives available for choosing the basis vectors, some of which will be discussed in this chapter. One is to derive a set of vectors which depend on the system operator, that is a set of vectors which depend on the large linearised matrix $\mathcal{A}$ in equation (2.24). Eigenmodes are well known as an efficient means of representing a solution over a given frequency range, and have been widely used in modal analyses for structural problems and also for aerodynamic reduced-order modelling [24]. However to calculate eigenmodes for a large, complex problem can be difficult. An alternative is to use the singular vectors of the system which are easy to compute, however these vectors do not possess the modal character of the eigenvectors and there is no guarantee that the required dynamics can be captured with a reduced set. Another option is to construct a set of vectors based on the solution characteristics of the problems under consideration. The proper orthogonal decomposition

[53] [4] is a method for extracting modal information based on simulations of the system. The final method which will be discussed is based on spanning Krylov subspaces of the matrix $\mathcal{A}$. This approach is related to the eigenmode models and includes the POD as a special case.

3.1 Aerodynamic Influence Coefficients

The first method of CFD model order reduction that will be described is an assumed-frequency approach. The high-order aeroelastic CFD model (2.51) will be used to calculate the blade response to a particular prescribed set of inputs. This calculation results in a set of influence coefficients which are coupled to the structural model and assumed to represent the response for all flows. For blade motion, these influence coefficients represent the magnitude of the forces generated on each blade due to an imposed unit sinusoidal motion on one blade and all other blades fixed. For external forcing, they represent the forces generated on each blade due to a unit sinusoidal disturbance in the appropriate flow quantity. Although coefficients must be constructed for each of the r blades being perturbed in turn, the calculation need only be performed for the first blade, with the remaining $r-1$ cases obtained through symmetry considerations.

Consider the calculation for plunging motion (those for pitching motion and external disturbance follow analogously). We impose a unit sinusoidal motion at a particular frequency, ω_c, on the first blade, and fix all other blades :

$$\begin{aligned} h_1 &= e^{i\omega_c t}, \\ h_j &= 0 \qquad j = 2, 3, \ldots, r. \end{aligned} \tag{3.1}$$

Although the motion is written as a complex quantity, this is done for convenience and it is only the real part which is relevant. The analysis can be completed more easily using complex quantities, and then the real part of the final answer taken.

The linearised CFD model (2.24) could be used to obtain the amplitude of the force acting on each blade under these conditions. This would involve performing a time simulation of the large linearised system for the entire bladed disk. The calculation can be performed much more efficiently by exploiting the linearity of the governing equations and performing a modal analysis as described in Section 2.1.5. The blade motion $\mathbf{h}$ already contains a single temporal frequency, and can be further decomposed into a finite set of orthogonal spatial Fourier modes. The component of motion

corresponding to spatial mode j is given by $\overline{h}_j$ and has an interblade phase angle of $\sigma_j = 2\pi j/r$. Since (2.24) is linear, the force contribution due to each $\overline{h}_j$ can be computed separately and then summed together over all j to obtain the overall force acting.

Consider the imposed blade motion given by (3.1). Applying the inverse of the transformation (2.31) to obtain the modal components of this motion, we find

$$\overline{h}_j = \frac{1}{r} \qquad j = 0, 1, 2, \ldots, r-1, \tag{3.2}$$

and note that since (3.1) represents a discrete spatial delta function, the Fourier transform (3.2) is a constant. The response due to each of the spatial modes can then be determined by solving the complex frequency domain Euler equations (2.40) on a single blade passage, requiring a total of r solves for each set of influence coefficients. Recombining the results for each spatial mode via (2.31), we obtain the complex force amplitude $\overline{L}$ acting on each blade due to sinusoidal motion of blade one. The instantaneous force acting on blade j due to motion of blade one can therefore be written as

$$L_{j1}(t) = \left(\overline{L}^R_{j1} + i\overline{L}^I_{j1}\right) h_1(t), \tag{3.3}$$

where $\overline{L}^R$ and $\overline{L}^I$ represent the real and imaginary parts of $\overline{L}$ respectively. In order to obtain real coefficients which can be implemented in the time domain, we note that for the assumed sinusoidal motion, blade velocity is related to blade displacement via $\dot{h} = i\omega_c h$. Equation (3.3) can therefore be written as

$$L_{j1}(t) = \overline{L}^R_{j1} h_1(t) + \frac{\overline{L}^R_{j1}}{\omega_c} \dot{h}_1(t) \tag{3.4}$$

and used in an influence coefficient model to represent the force generated on blade j due to any general motion of blade one. However, due to the assumptions made in obtaining the coefficients, the representation for non-sinusoidal motions will obviously contain inaccuracies.

The procedure to calculate the influence coefficients can be summarised as follows. Firstly, for each type of blade motion impose a unit motion on blade one which varies sinusoidally with time at the assumed frequency ω_c, and fix all other blades. Next, decompose this motion into its r spatial Fourier modes and compute the resulting flow for each mode separately by solving the complex system (2.40) a total of r times. Each of these contributions is then summed over the full rotor using (2.31) to determine the overall flow response and the resulting aerodynamic force on each blade. This produces the influence coefficients for motion of blade one. Finally, the coefficients for

subsequent blades can be obtained via symmetry; that is noting that the force on blade n due to motion at blade m is identical to the force on blade $n+p$ due to motion at blade $m+p$. Coefficients for external disturbances are computed in an analogous way, noting that allowable spatial frequencies σ_j now hold for any integer value of j. In practice, a finite set of values of spatial frequency are chosen which are representative of the expected disturbances. These influence coefficients are then used to represent the aerodynamics in equation (2.50) for *all* flows, not just sinusoidal motions at ω_c.

3.2 Reduction Using Congruence Transforms

Although the aerodynamic influence coefficient method provides a means of obtaining low-order, high-fidelity aerodynamics, the resulting model is only precise for sinusoidal motions at the assumed frequency, and has an unknown region of validity for other similar (in frequency content and forcing shape) flows. Interaction between the aerodynamics and structure often excites a significant range of temporal frequencies and damping in the blade aeroelastic response, and in many turbomachinery flows a high degree of coupling or blade-to-blade variations may be present, in which case these simple models are inadequate. Also, non-sinusoidal forcing inputs may often be of interest. An alternative approach is to take the high-order linear CFD model (2.24) and project it onto a set of efficient basis vectors to create a low-order model which captures the relevant high-fidelity dynamics over a range of frequencies.

It is desirable to choose an orthogonal set of vectors, since the resulting congruent transformation preserves the system definiteness, and therefore often preserves system stability. If the set of q orthonormal basis vectors are contained in the columns of the matrix V_q, a qth order approximation to the perturbation solution can be made by assuming

$$\mathbf{U}' = V_q \mathbf{v}, \tag{3.5}$$

where $\mathbf{v}(t)$ is the reduced-order aerodynamic state vector. Substituting this representation of $\mathbf{U}'$ into the linearised governing equations (2.24), we obtain the reduced-order system

$$\frac{d\mathbf{v}}{dt} = V_q^T \mathcal{A} V_q \mathbf{v} + V_q^T \mathcal{B} \mathbf{u} + V_q^T \mathcal{E} \mathbf{d}. \tag{3.6}$$

Writing the reduced-order matrix as $A = V_q^T \mathcal{A} V_q$, it is clear from (3.6) that the definiteness of the

original system has been preserved. Consider an arbitrary vector $\mathbf{w}$, then

$$\mathbf{w}^T A\mathbf{w} = \mathbf{w}^T V_q^T \mathcal{A} V_q \mathbf{w} = (V_q \mathbf{w})^T \mathcal{A} (V_q \mathbf{w}) . \tag{3.7}$$

Therefore if the original matrix $\mathcal{A}$ yields strictly positive results from a quadratic form such as (3.7), so will the reduced system matrix A. This is the definition of positive definiteness; an analogous statement can be made for negative definiteness and we also note that indefinite matrices remain indefinite. A negative semidefinite matrix implies that all the eigenvalues have non-positive real part and the aerodynamic system is stable. In this case, the model reduction will preserve the stability properties of the system. Many representations involve the computation of two sets of vectors, a right set V_q and a left set W_q, where V_q and W_q are orthogonal. In this case, the reduced-order system becomes

$$\frac{d\mathbf{v}}{dt} = W_q^T \mathcal{A} V_q \mathbf{v} + W_q^T \mathcal{B}\mathbf{u} + W_q^T \mathcal{E}\mathbf{d} \tag{3.8}$$

and in general the definiteness of the matrix is not preserved. Unfortunately in the aerodynamic governing equations considered here, it is not possible to determine the definiteness of the system matrix. The result (3.7) is therefore of limited use in this context.

3.3 Eigenmode Representation

A reduced-order model can be obtained by computing the eigenmodes of the large linear system (2.24) and selecting just a few to form a basis. This approach has been taken for many problems, especially in structural dynamics where the matrices are generally symmetric and the eigenmodes are easy to compute. Typically the modes with low frequencies are chosen. A large error can result from the omission of the higher frequency modes, especially if the forcing contains a significant high-frequency component. This error can be reduced by using a static correction as discussed in [46]. Eigenmodes have been used to form reduced-order models in many applications. While they may in practice form a very efficient basis, they are very expensive and difficult to compute for such large systems, even in a two-dimensional analysis.

To describe the difficulties associated with the computation of eigenvalues in a turbomachinery context, an attempt was made to calculate the eigenmodes of the system (2.24) for the subsonic rotor described in Section 2.2.1. The numerical package ARPACK was used for the eigenvalue computations [35]. This software uses the Implicitly Restarted Arnoldi Method and is appropriate for sparse

complex matrices. However, only the first five eigenmodes were able to be calculated accurately for a large problem, even with the use of complex shifting techniques. The degree of ill-conditioning of the eigenvalue problem was investigated by looking at the sensitivity of the eigenvalues to random perturbations in the entries of the matrix $\mathcal{A}$. For a smaller problem (a very coarse grid) of size $n = 492$ the eigenvalue spectrum was calculated. The eigenmodes for this case were calculated accurately using a complex shifting technique. The matrix entries were then randomly perturbed by quantities on the order of 0.001% of the diagonal term and the eigenvalues were recalculated. In this case, less than a 1% movement of the eigenvalues was noted. The same process was applied for perturbations of the order 0.1% and the eigenvalues were now seen to vary significantly, up to 25% for some modes. These results are plotted in Figure 3-1. The same analysis was applied to a realistic problem ($n = 7632$) and it can be seen from Figure 3-2 that even perturbations of the order 0.001% made a significant difference to the eigenvalues, with variations of up to 20% observed. It was determined that the eigenvalue problem for a realistic grid was very ill-conditioned, which means that the matrix is non-normal. This makes it very difficult to calculate the eigenmodes accurately, and also suggests that the eigenmodes may not have physical significance [55].

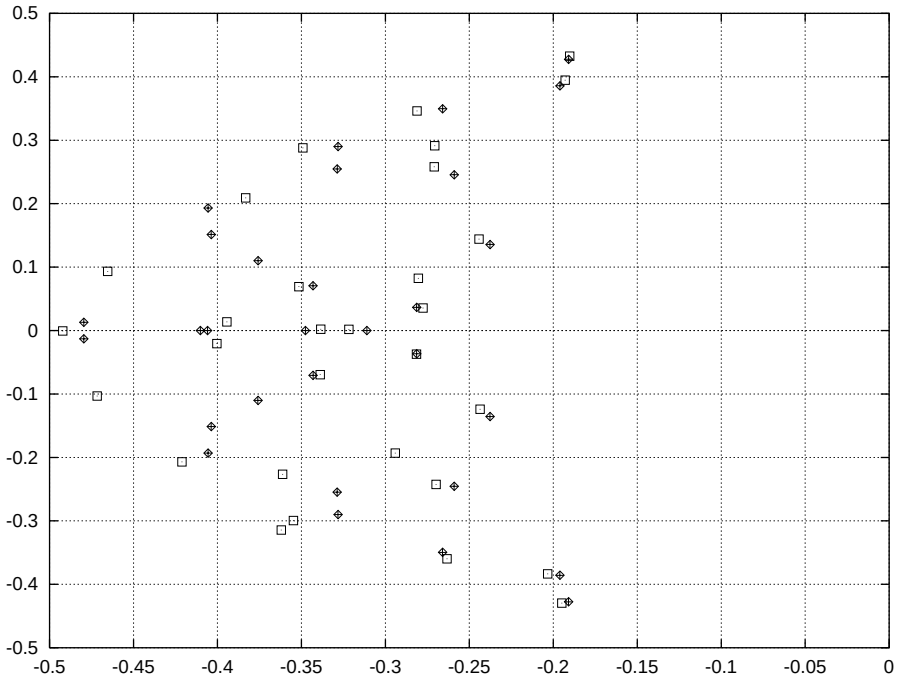

Figure 3-1: Eigenvalue spectrum for small problem, $n = 492$. Eigenvalues for unperturbed matrix (diamonds) and random perturbations of order 0.1% (squares) and 0.001% (plus signs) of the diagonal.

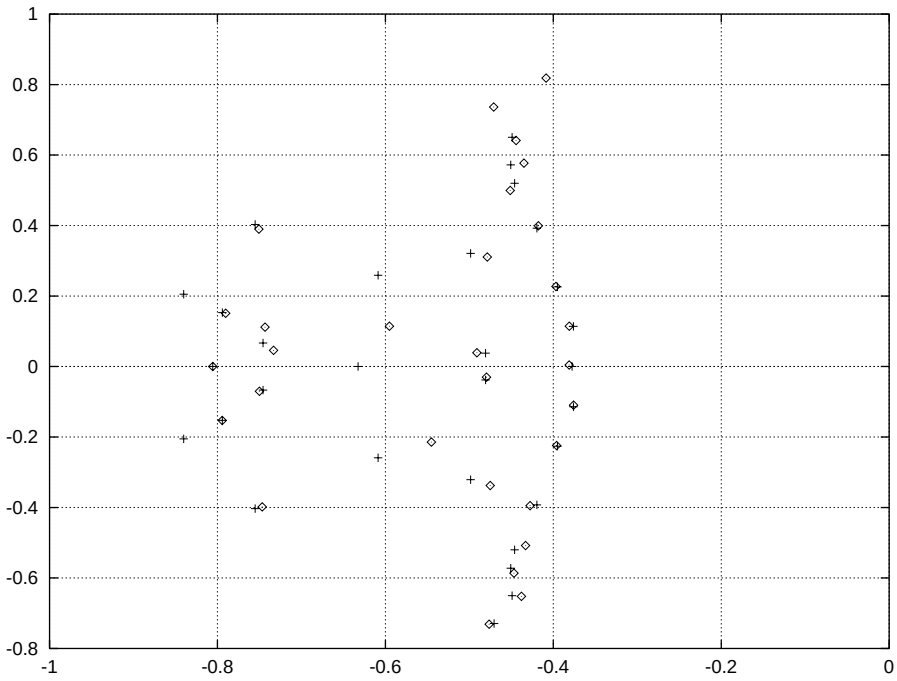

Figure 3-2: Eigenvalue spectrum for large problem, $n = 7632$. Eigenvalues for unperturbed matrix (plus signs) and random perturbations of order 0.001% (diamonds) of the diagonal.

In addition, for a non-symmetric problem as in the system considered here, both the right eigenvectors V_q and the left eigenvectors W_q must be computed. Although this is not a congruent transformation, a basis is obtained which preserves system stability, since the eigenvalues of the reduced-order model are a subset of the original system eigenvalues. This can be seen by noting that the reduced system matrix is

$$A = W_q^T \mathcal{A} V_q = \Lambda_q, \tag{3.9}$$

where Λ_q is a diagonal matrix whose entries are the eigenvalues corresponding to those eigenvectors included in the basis V_q.

Other orthogonal sets can be computed more easily, for example the singular vectors of the matrix, however these lack the efficiency of the eigenvectors and a very large number may be required to obtain reasonable solutions. A reduced-order model was constructed using the right singular vectors as a basis and it was determined that several hundred modes per interblade phase angle were required to capture the relevant flow dynamics accurately.

3.4 Proper Orthogonal Decomposition

The POD is a popular alternative to the eigenmode approach for determining an efficient basis. Typically, a time simulation of the system for a characteristic unsteady flow is performed and instantaneous solutions or *snapshots* are obtained at selected times. These snapshots are then combined to produce an orthogonal set of basis vectors which represents the solution $\mathbf{U}'$ in some optimal way. The criterion for choosing the basis vectors was first posed in variational form in [53]. Here we consider choosing the basis vectors $\mathbf{\Psi}$ so as to maximise the following cost [4]:

$$\max_{\mathbf{\Phi}} \frac{\langle |(\mathbf{U}', \mathbf{\Phi})|^2 \rangle}{(\mathbf{\Phi}, \mathbf{\Phi})} = \frac{\langle |(\mathbf{U}', \mathbf{\Psi})|^2 \rangle}{(\mathbf{\Psi}, \mathbf{\Psi})}, \tag{3.10}$$

where $(\mathbf{U}', \mathbf{\Psi})$ denotes the scalar product of the basis vector with the field $\mathbf{U}'(\mathbf{x}, t)$ and $\langle\ \rangle$ represents a time-averaging operation. Equation (3.10) can be rewritten as a constrained optimisation problem

$$\max_{(\mathbf{\Phi}, \mathbf{\Phi})=1} \langle |(\mathbf{U}', \mathbf{\Phi})|^2 \rangle. \tag{3.11}$$

We can then form the Lagrangian function

$$\mathcal{L}(\mathbf{\Phi}, \lambda) = \langle |(\mathbf{U}', \mathbf{\Phi})|^2 \rangle - \lambda \left[(\mathbf{\Phi}, \mathbf{\Phi}) - 1 \right], \tag{3.12}$$

where λ is the Lagrange multiplier for the constraint on the norm of the basis vector. By differentiating (3.12) and setting the result to be zero, we obtain that the function $\mathbf{\Psi}$ providing the maximum in (3.10) is an eigenfunction of the kernel K defined by

$$K(\mathbf{x}, \mathbf{x}') = \frac{1}{n} \sum_{i=1}^{n} \mathbf{U}_i'(\mathbf{x}) \mathbf{U}_i'(\mathbf{x}'), \tag{3.13}$$

where $\mathbf{U}_i'(\mathbf{x})$ is the instantaneous perturbation flow field at a time t_i and the number of snapshots n is sufficiently large [53]. The eigenvectors of K are of the form

$$\mathbf{\Psi} = \sum_{i=1}^{n} B_i \mathbf{U}_i', \tag{3.14}$$

where the constants B_i can be seen to satisfy the eigenvector equation

$$CB = \Lambda B \tag{3.15}$$

and C is now the correlation matrix constructed by forming inner products between the snapshots

$$C_{ij} = \frac{1}{n} (\mathbf{U}_i', \mathbf{U}_j') \qquad 1 < i < n, \quad 1 < j < n. \tag{3.16}$$

It can also be shown [4] that the maximum in (3.10) is achieved and the eigenfunction obtained corresponds to μ_1, the largest eigenvalue of C.

The procedure to calculate the POD basis vectors can be summarised as follows. A set of n snapshots characterising problems of interest is obtained and used to calculate the correlation matrix C defined by (3.16). The eigenvalues μ_i and eigenvectors $\mathbf{a}_i = [\alpha_1^i \alpha_2^i \dots \alpha_n^i]^T$ of C are computed and ordered according to the size of the real eigenvalues: $\mu_1 \geq \mu_2 \geq \dots \geq \mu_n$. Now the basis vectors $\mathbf{\Psi}_i$ are chosen as linear combinations of the snapshots, namely: $\mathbf{\Psi}_i = \sum_{j=1}^{n} \alpha_j^i \mathbf{U}'_j$. Then for any q, we represent the solution as a linear combination of basis vectors

$$\mathbf{U}'(\mathbf{x}, t) = \sum_{i=1}^{q} v_i(t) \mathbf{\Psi}_i(\mathbf{x}). \tag{3.17}$$

The magnitude of the ith POD eigenvalue μ_i determines the amount of "flow energy" $\langle (\mathbf{U}', \mathbf{U}') \rangle$ contained in the ith basis vector, and since

$$\sum_{i=1}^{q} \langle |v_i(t)|^2 \rangle = \sum_{i=1}^{q} \mu_i, \tag{3.18}$$

for a given number of modes the POD is optimal for reconstructing a signal $\mathbf{U}'(\mathbf{x}, t)$ in the sense that the subspace spanned by the resulting vectors $\mathbf{\Psi}_i$ minimizes the "averaged energy" or the 2-norm of the error between the exact and projected data.

3.4.1 Snapshot Generation

Typically in a POD approach of the form described, a time simulation of the full system is run which is characteristic of the types of flows we wish to analyse and control. In this simulation certain modes of the system are excited, and the POD analysis captures this information as snapshots are taken at different instants in time. It is therefore crucial that the important system dynamics are excited in the sample simulation. This raises an issue if the reduced-order model is to be used for control, since the idea in controlling a system is the change the nature of the system dynamics. If the POD analysis is performed on the uncontrolled system, then the modes captured could be completely different from the important dynamics of the controlled system, and the reduced-order model will not accurately represent the controlled system [18]. Also, the time-marching simulation of the full bladed disk is an expensive computation.

A more convenient approach is to use linearity and the frequency domain to address some of the problems associated with the time-domain POD method. The frequency-domain form of the Euler

equations was discussed in the previous chapter. The forcing and aerodynamic response is decomposed into spatial and temporal Fourier modes and the snapshots for each of these modes are obtained separately. A conventional POD analysis on a motion which contains just a single temporal frequency shows that only two independent modes exist. The harmonic motion can be completely reproduced with a linear combination of these two modes. We also note that a harmonic motion can be completely described by a complex magnitude vector as in (2.39):

$$\mathbf{U}' = \overline{\mathbf{U}} e^{i\omega t} = (\overline{\mathbf{U}}_R \cos\omega t - \overline{\mathbf{U}}_I \sin\omega t) + i(\overline{\mathbf{U}}_I \cos\omega t + \overline{\mathbf{U}}_R \sin\omega t). \tag{3.19}$$

Rather than obtaining the snapshots from a time simulation of each harmonic component of the forcing, for each spatial frequency σ_j we pick a set of sample temporal frequencies ω_k and solve the frequency domain equations (2.40) on a single passage to obtain the complex solution $\overline{\mathbf{U}}^{jk}$. We then take the real and imaginary parts of this solution as snapshots for the POD process. If the complex solution for frequencies σ_j and ω_k has real and imaginary parts $\overline{\mathbf{U}}_R$ and $\overline{\mathbf{U}}_I$ respectively, the snapshots for the full rotor are constructed as follows:

$$\mathbf{U}_1 = \left\{ \begin{array}{c} \overline{\mathbf{U}}_R \\ \overline{\mathbf{U}}_R \cos\sigma_j - \overline{\mathbf{U}}_I \sin\sigma_j \\ \overline{\mathbf{U}}_R \cos 2\sigma_j - \overline{\mathbf{U}}_I \sin 2\sigma_j \\ \cdots \\ \overline{\mathbf{U}}_R \cos(r-1)\sigma_j - \overline{\mathbf{U}}_I \sin(r-1)\sigma_j \end{array} \right\} \tag{3.20}$$

and

$$\mathbf{U}_2 = \left\{ \begin{array}{c} \overline{\mathbf{U}}_I \\ \overline{\mathbf{U}}_I \cos\sigma_j + \overline{\mathbf{U}}_R \sin\sigma_j \\ \overline{\mathbf{U}}_I \cos 2\sigma_j + \overline{\mathbf{U}}_R \sin 2\sigma_j \\ \cdots \\ \overline{\mathbf{U}}_I \cos(r-1)\sigma_j + \overline{\mathbf{U}}_R \sin(r-1)\sigma_j \end{array} \right\}. \tag{3.21}$$

Because we are working in the frequency domain and the forcing contains a single spatial frequency, all complex solves are made on just a single passage. The frequency domain approach is therefore much more efficient than sampling in the time domain. Additionally, we are picking relevant frequency content when choosing the basis vectors, rather than modes which are excited under a certain type of forcing. If it is possible to assess what range of frequencies will be present in both the uncontrolled and the controlled response, then a reduced-order model can be constructed which represents both sets of system dynamics.

The quality of the reduced-order model is highly dependent on the (arbitrary) choice of sample frequencies. Careful consideration needs to be given to ensure that the range sampled spans all important frequencies in problems of interest, and also that a sufficiently high number of frequencies within this range are included. Although much more efficient than a time domain POD analysis, this model requires the large matrix $[i\omega_k - A_j]$ to be factored for each pair of snapshots. If a large frequency range needs to be considered, the cost of generating the model can become high.

3.5 Arnoldi-Based Model Order Reduction

In this section, an approach will be developed which is related to the eigenmode approach and includes the POD method as a special case. A set of Arnoldi vectors is used to construct the basis [55]. The Arnoldi vectors approximate the eigenvectors [47] but are much more straightforward to compute. The full set of Arnoldi vectors spans the same solution space as the system eigenvectors; a reduced set of q vectors spans the qth order Krylov subspace. The approach also contains some flavour of the POD in that an efficient reduced set can be constructed by considering inputs and outputs of interest. While the basis is easy to compute, some of the issues associated with the sampling requirements in the POD are addressed. Padé-based reduced-order models have been developed for linear circuit analysis using the Lanczos process [13]. This approach matches as many moments of the system transfer function as there are degrees of freedom in the reduced system. While the Arnoldi vectors match only half the number of moments as the Padé approximation, they preserve system definiteness and, as discussed in Section 3.2, in the case of a stable negative definite system therefore preserve stability [52]. The Arnoldi vectors are also much cheaper to compute than the Padé vectors.

Our basic goal is to obtain a reduced system which has many fewer states than the original system, but which still represents the original system's dynamics accurately. One approach to ensuring accurate representation of system dynamics would be to try to match the transfer functions of the reduced and the original systems. This would enable us to replicate the output behaviour of the high-order CFD model for a range of inputs. Consider first a single input, single output system

$$\dot{\mathbf{U}}' = \mathcal{A}\mathbf{U}' + \mathbf{b}u, \qquad y = \mathbf{c}^T\mathbf{U}'. \tag{3.22}$$

We note that if the output definition were to include direct transmission terms of the form $\mathcal{D}\mathbf{u}$ or $\mathcal{F}\mathbf{d}$, these would not affect the model order reduction procedure. The transfer function between

input $u(t)$ and output $y(t)$ is

$$H(s) = \mathbf{c}^T(sI - \mathcal{A})^{-1}\mathbf{b}, \tag{3.23}$$

which can also be represented as a rational function

$$H(s) = \frac{N(s)}{D(s)} = \frac{b_{n-1}s^{n-1} + b_{n-2}s^{n-2} + \ldots + b_1 s + b_0}{a_n s^n + a_{n-1}s^{n-1} + \ldots + a_1 s + 1}, \tag{3.24}$$

where n is the dimension of the high-order system (3.22). A qth order Padé approximation to the transfer function is obtained by retaining q coefficients in each of the polynomials $N(s)$ and $D(s)$ as follows:

$$H_q(s) = \frac{\tilde{b}_{q-1}s^{q-1} + \ldots + \tilde{b}_1 s + \tilde{b}_0}{\tilde{a}_q s^q + \tilde{a}_{q-1}s^{q-1} + \ldots + \tilde{a}_1 s + 1}. \tag{3.25}$$

The $2q$ coefficients $\tilde{a}_j$ and $\tilde{b}_k$ are selected so as to match the coefficients of the first $2q$ terms in a McLaurin expansion of the transfer function (3.23). We can write

$$H(s) = -\sum_{k=0}^{\infty} m_k s^k, \tag{3.26}$$

where the kth coefficient

$$m_k = \mathbf{c}^T \mathcal{A}^{-(k+1)}\mathbf{b} \tag{3.27}$$

is the kth moment of $H(s)$. By equating (3.25) and (3.26), and considering each power of s separately, a system of equations for the $\tilde{a}_j$ and $\tilde{b}_k$ can be obtained. The q Padé vectors can be constructed via the Lanczos process and will therefore lead to a reduced-order system which matches the first $2q$ moments of $H(s)$.

An alternative approach is to use the Arnoldi method to generate a set of vectors which spans the qth order Krylov subspace defined by

$$\mathcal{K}_q(\mathcal{A}, \mathbf{b}) = span\{\mathcal{A}^{-1}\mathbf{b}, \mathcal{A}^{-2}\mathbf{b}, ..., \mathcal{A}^{-q}\mathbf{b}\}. \tag{3.28}$$

By selecting the sequence of vectors

$$\begin{aligned} \mathbf{\Psi}_1 &= A^{-1}\mathbf{b}, \\ \mathbf{\Psi}_2 &= A^{-2}\mathbf{b} \perp \mathbf{\Psi}_1, \end{aligned}$$

$$\vdots$$

$$\mathbf{\Psi}_q \quad = \quad A^{-q}\mathbf{b} \perp (\mathbf{\Psi}_1, \mathbf{\Psi}_2, \ldots, \mathbf{\Psi}_{q-1}) \tag{3.29}$$

for the basis V_q, a qth order reduced-order model of the form (3.6) is obtained. In (3.29), the symbol $\perp$ denotes the orthogonalisation of each vector with all previous vectors. This is done by subtracting the appropriate components, as in a standard Gram-Schmidt orthogonalisation procedure. The q moments of the transfer function of this reduced system are identical to the first q moments of the original system transfer function, as is proved in [52]. The Arnoldi approach therefore matches only half the number of moments as the Padé approximation, however the basis is much cheaper to compute. It is possible to reduce systems with multiple inputs using the block Arnoldi method. For example, if we consider a system with two inputs u_1 and u_2,

$$\dot{\mathbf{U}}' = \mathcal{A}\mathbf{U}' + \mathbf{b}_1 u_1 + \mathbf{b}_2 u_2, \tag{3.30}$$

then the block Arnoldi method is used to generate vectors which span the Krylov subspace

$$\mathcal{K}_q(\mathcal{A}, \mathbf{b_1}, \mathbf{b_2}) = span\{\mathcal{A}^{-1}\mathbf{b}_1, \mathcal{A}^{-1}\mathbf{b}_2, \mathcal{A}^{-2}\mathbf{b}_1, \mathcal{A}^{-2}\mathbf{b}_2, ..., \mathcal{A}^{-q}\mathbf{b}_1, \mathcal{A}^{-q}\mathbf{b}_2, \}. \tag{3.31}$$

We also note that it is not necessarily the first q moments of the transfer function which must be matched. If we were to consider a Taylor series expansion of the transfer function about some non-zero value of s, a model could be obtained which would give a better approximation of the system dynamics for higher frequencies. For an expansion about $s = i\omega$, the jth basis vector has the form $(A - i\omega)^{-j}\,\mathbf{b}$. These multiple frequency point Arnoldi methods are described in [19].

3.5.1 Computation of Arnoldi Basis

In order to calculate the basis, we consider input vectors which correspond to a particular blade having a unit displacement or velocity and all other blades fixed. Although vectors must be constructed for each of the r blades being perturbed in turn, the calculation need only be performed once, with the remaining $r - 1$ vectors constructed through symmetry considerations. Once again we can use linearity to decompose this forcing into a set of r orthogonal modes each containing a single spatial frequency via (2.31), and the calculation for each of these modes can be performed on a single blade passage. For expansions of the transfer function about $s = i\omega_k$, solutions must be performed of the complex frequency domain equations (2.40). The resulting solutions are then combined via the

inverse of the transformation (2.31) to obtain the first blade basis vector. Vectors for subsequent blades are computed through use of symmetry. Further simplification can be obtained by noting that for expansions about $s = 0$, the set of Arnoldi vectors for spatial frequencies σ and $-\sigma$ are complex conjugates of one another. The algorithm for the single input, single output case expanded about ω_k is shown below.

Algorithm 3.1 (Arnoldi Method)

`arnoldi(input` $\mathcal{A}, \mathbf{b}, \omega_k, q_k, r$`; output` V_q`)`

{

`for` $(j = 0; j <= r-1; j++)$ { `% loop over interblade phase angles`

  `Factor` $[i\omega_k - \mathcal{A}_j]$ `% most expensive step in the algorithm`

  `Solve` $[i\omega_k - \mathcal{A}_j]\mathbf{\Psi}_1 = \mathbf{b}$ `% first basis vector` $\mathbf{\Psi}_1 = \mathcal{A}_{jk}^{-1}\mathbf{b}$

  `for` $(k = 1; k < q_k; k++)$ { `% loop over Krylov subspace directions`

    `Solve` $[i\omega_k - \mathcal{A}_j]\mathbf{w} = \mathbf{\Psi}_k$ `% subsequent vectors` $\mathbf{\Psi}_i = \mathcal{A}_{jk}^{-1}\mathbf{\Psi}_{i-1}$

    `for` $(i = 1; i <= k; i++)$ { `% orthogonalise wrt previous vectors`

      $h = \mathbf{w}^T\mathbf{\Psi}_i$ `% compute projections`

      $\mathbf{w} = \mathbf{w} - h\mathbf{\Psi}_i$ `% subtract the projections for orthogonality`

    }

    $\mathbf{\Psi}_{k+1} = \frac{\mathbf{w}}{||\mathbf{w}||}$ `% normalise to get the` $(k+1)$`th basis vector`

  }

  $V_q^j = [\mathbf{\Psi}_1 ... \mathbf{\Psi}_q]$ `%` q`th order basis for` j`th spatial frequency`

 }
}

3.5.2 Arnoldi Approach versus POD

One can see the similarities between the POD approach and the multiple frequency point Arnoldi method. In fact, solving the system (2.40) at J frequencies to obtain the POD snapshots results in

an identical data set as taking J frequency points and computing a single Arnoldi vector at each point (the subsequent orthogonalisation procedure differs between the two methods). This can be seen by noting that the vector which solves the complex system (2.40) is both the POD snapshot at the frequency ω_k and the first vector in the Arnoldi basis expanded about ω_k. It is postulated that very efficient models could be constructed by considering a range of frequencies and using the POD analysis to choose the basis vectors, but also computing more than one vector at each frequency as in the Arnoldi approach. One must evaluate the relative gain in choosing a higher number of frequency points, since by far the most expensive part of the calculation is the factorisation of the matrix in solving the linear system. In the Arnoldi approach, the matrix is computed and factored just once for each ω_k and σ_j, but as outlined in the Algorithm 3.1, q_k vectors are obtained per factorisation. For the POD a different matrix must be factored for every pair of snapshots, and moreover the number of snapshots typically exceeds the final number of basis vectors constructed by a significant amount.

3.5.3 Arnoldi Model Extensions

The Arnoldi method described here could be further extended to produce even more efficient models. It would be possible to consider the dual problem. That is, instead of forming vectors which span the Krylov space $\mathcal{K}_q(\mathcal{A}, \mathbf{b})$, we choose vectors which span the dual Krylov space $\mathcal{K}'_q(\mathcal{A}^T, \mathbf{c})$. This would involve solving a series of systems of the form $\mathcal{A}^T\mathbf{v} = \mathbf{c}$. In this way more efficient models can be obtained if the number of inputs of the original system is greater than the number of outputs. This is typically the case in aeroelastic analyses, since for each structural degree of freedom there are two inputs (blade position and velocity) and just one output (aerodynamic force or moment). For example for plunge, the inputs are h and $\dot{h}$, while the single output is the force on the blade C_l. This concept could be further extended if *both* inputs and outputs of interest were included in the choice of basis vectors. The resulting system could be post-processed using a truncated balanced realisation to get even more improvement [27].

3.6 Projection onto Optimal Basis Vectors

Although we use the frequency domain to obtain the snapshots efficiently on a single blade passage (whether using the POD or the Arnoldi approach), the reduced-order model is developed in the time domain for the full rotor. The resulting set of ordinary differential equations is in "state-space" form and can therefore be easily incorporated into a general aeroelastic analysis.

3.6.1 Static Corrections

If eigenmodes are used to form the basis, a significant error can arise due to the high-frequency modes which are excluded, especially if the forcing function contains a significant component in these frequencies. This has been well documented for both structural dynamic problems [5] and aerodynamic problems [46, 24]. The "mode-displacement" method can be used to reduce this error, thus allowing accurate models to be constructed with a small number of eigenmodes. The high-frequency modes can be assumed to respond in a quasi-static way, so that the solution can be written

$$\mathbf{U}'(\mathbf{x},t) = \mathbf{U}_{\text{hom}}(\mathbf{x},t) + \mathbf{U}_{\text{par}}(\mathbf{x},t). \tag{3.32}$$

The homogeneous part of the solution is projected onto a small number of basis functions

$$\mathbf{U}_{\text{hom}}(\mathbf{x},t) = \sum_{i=1}^{q} v_i(t)\,\mathbf{\Psi}_i(\mathbf{x}), \tag{3.33}$$

while static corrections are derived for blade motion and each type of external disturbance. If we consider the external flow disturbance to be in the ℓth spatial Fourier mode, $d(\theta,t) = d_\ell(t)e^{il\theta}$, then the particular solution is

$$\mathbf{U}_{\text{par}}(\mathbf{x},t) = h(t)\mathbf{U}_h(\mathbf{x}) + \dot{h}(t)\mathbf{U}_{\dot{h}}(\mathbf{x}) + \alpha(t)\mathbf{U}_\alpha(\mathbf{x}) + \dot{\alpha}(t)\mathbf{U}_{\dot{\alpha}}(\mathbf{x}) + d_\ell(t)\mathbf{U}_\ell. \tag{3.34}$$

The static correction functions $\mathbf{U}_h$, $\mathbf{U}_{\dot{h}}$, $\mathbf{U}_\alpha$ and $\mathbf{U}_{\dot{\alpha}}$ are particular solutions of the flow system and are precomputed by solving for steady flows with unit boundary conditions on blade position and velocity. Similarly, $\mathbf{U}_\ell$ is the ℓth spatial Fourier component of a steady flow with a unit external disturbance and is also precomputed.

These corrections are not required for the POD or Arnoldi approaches, since the basis vectors are selected based on solutions of the flow system, which already contain the relevant high-frequency dynamics. In fact, we note that for Arnoldi vectors computed about $s = 0$, the first basis vector is exactly the static correction, although the solution representation is slightly different. For example, if we consider plunge and write the forcing term $\mathcal{B}\mathbf{u}$ in (2.24) as $\mathbf{b}_h h + \mathbf{b}_{\dot{h}}\dot{h}$, then the first two Arnoldi vectors satisfy the equations

$$\mathcal{A}\mathbf{\Psi}_1 = \mathbf{b}_h \tag{3.35}$$

and

$$\mathcal{A}\mathbf{\Psi}_2 = \mathbf{b}_h. \tag{3.36}$$

Equations (3.35) and (3.36) represent exactly flows with a unit blade displacement and velocity respectively, which are the conditions used to obtain the static corrections. The resulting reduced-order models have a much simpler form if the static corrections are not used. For completeness, derivation of reduced-order models both with and without the corrections will be presented.

3.6.2 Reduced-Order Models

If no static corrections are used, the reduced-order model is simple to derive. The assumed expansion for the solution (3.33) is substituted into the governing equations (2.24), where the basis vectors $\mathbf{\Psi}$ could be derived from either the POD or the Arnoldi-based approach. Using orthogonality, a system of ordinary differential equations for the modal coefficients is obtained as follows

$$\frac{dv_i}{dt} = \mathbf{\Psi}_i^T \mathcal{A} \sum_{i=1}^{q} v_j \mathbf{\Psi}_j + \mathbf{\Psi}_i^T \mathcal{B}\mathbf{u} + \mathbf{\Psi}_i^T \mathcal{E}\mathbf{d}. \tag{3.37}$$

The reduced-order model is constructed by considering each pair of interblade phase angles $\pm\sigma$ separately, and using the fact that solutions at different interblade phase angles, since they represent circumferential Fourier modes, are orthogonal to one another. Since (3.37) represents a congruent transformation, the definiteness of the original matrix $\mathcal{A}$ is preserved, as discussed in Section 3.2. The full state-space system can be written

$$\dot{\mathbf{v}} = A\mathbf{v} + B\mathbf{u} + E\mathbf{d} \qquad\qquad \mathbf{y} = C\mathbf{v}, \tag{3.38}$$

where $\mathbf{v}$ contains all the modal coefficients and the A matrix is block diagonal according to interblade phase angle,

$$A = \begin{bmatrix} [A_1] & 0 & 0 & 0 \\ 0 & [A_2] & 0 & 0 \\ 0 & 0 & [\ldots] & 0 \\ 0 & 0 & 0 & [\ldots] \end{bmatrix}. \tag{3.39}$$

This can be seen by noting that for a basis vector $\mathbf{\Psi}_j$ corresponding to interblade phase angle σ_j, the vector $A\mathbf{\Psi}_j$ also has a spatial frequency of σ_j since the matrix A is periodic and is the same in each passage. The value of $\mathbf{\Psi}_i^T A \mathbf{\Psi}_j$ in (3.37) is therefore zero if $\mathbf{\Psi}_j$ and $\mathbf{\Psi}_i$ correspond to different

spatial frequencies. Note also that in (3.38) the states $\mathbf{v}$ correspond to each interblade phase angle, while the inputs $\mathbf{u}$ correspond to each blade.

The output vector $\mathbf{y}$ contains quantities of interest, typically the aerodynamic forces and moments acting on each blade. For r blades the output vector $\mathbf{y}$ defining aerodynamic forces and moments is given by

$$\mathbf{y} = \begin{bmatrix} C_l^1 \\ C_m^1 \\ C_l^2 \\ C_m^2 \\ \cdots \\ \cdots \\ C_l^r \\ C_m^r \end{bmatrix}. \tag{3.40}$$

The matrix C defines the output appropriately and is typically a function of the problem geometry.

With the use of static corrections, the system becomes a little more complicated. Substituting the assumed expansions for the perturbation solution (3.33) and (3.34) into the governing equations (2.24) and using orthogonality, a slightly different system of ordinary differential equations is obtained as follows:

$$\frac{dv_i}{dt} = \overline{\mathbf{\Psi}}_i^T \mathcal{A} \sum_{i=1}^{q} v_j \overline{\mathbf{\Psi}}_j + f_i, \tag{3.41}$$

where the forcing vector f is given by

$$f_i(t) = -\dot{\overline{h}}(t)\overline{\mathbf{\Psi}}_i^T \mathbf{U}_h - \ddot{\overline{h}}(t)\overline{\mathbf{\Psi}}_i^T \mathbf{U}_{\dot{h}} - \dot{\overline{\alpha}}(t)\overline{\mathbf{\Psi}}_i^T \mathbf{U}_\alpha - \ddot{\overline{\alpha}}(t)\overline{\mathbf{\Psi}}_i^T \mathbf{U}_{\dot{\alpha}} - \dot{d}_\ell(t)\overline{\mathbf{\Psi}}_i^T \mathbf{U}_\ell. \tag{3.42}$$

Because the static correction functions are derived for each interblade phase angle, $\overline{h}$ and $\overline{\alpha}$ in (3.42) represent the component of blade displacement corresponding to a particular spatial frequency. In order to write these in terms of the actual blade displacements, the problem is formulated in a standing wave representation which allows for arbitrary transient motion of the blades [10]. The arbitrary motion of r blades $\mathbf{u}_j$ can be represented as a superposition of r standing wave modes. For example for plunge displacement, we write

$$h_j(t) = \sum_{r=0}^{\frac{r-1}{2}} \left[h_{cr}(t) \cos j\sigma_r + h_{sr}(t) \sin j\sigma_r \right]. \tag{3.43}$$

The two travelling modes corresponding to interblade phase angles σ and $-\sigma$ are considered together to obtain two standing wave modes for each pair. This can be written equivalently in matrix form as

$$\mathbf{h} = \tilde{P}\overline{\mathbf{h}}_r, \tag{3.44}$$

where $\mathbf{h}$ contains the plunge displacement of each blade as a function of time and $\overline{\mathbf{h}}_r$ contains the so-called multiblade coordinates h_{cr} and h_{sr}. $\tilde{P}$ is the transformation matrix from standing waves to blade coordinates and is given by

$$\tilde{P} = \begin{bmatrix} 1 & \cos 0\sigma_1 & \sin 0\sigma_1 & \dots & \sin 0\sigma_{(r-1)/2} \\ 1 & \cos 1\sigma_1 & \sin 1\sigma_1 & \dots & \sin 1\sigma_{(r-1)/2} \\ \vdots & \vdots & \vdots & \vdots & \vdots \\ 1 & \cos(r-1)\sigma_1 & \sin(r-1)\sigma_1 & \dots & \sin(r-1)\sigma_{(r-1)/2} \end{bmatrix} \tag{3.45}$$

The system of ordinary differential equations (3.41) can therefore be written

$$\dot{\mathbf{v}} = \overline{A}\mathbf{v} + \overline{B}_r\tilde{\mathbf{u}}_r + \overline{E}\dot{\mathbf{d}} \qquad \mathbf{y} = \overline{C}\mathbf{v} + \overline{D}_r\tilde{\mathbf{u}}_r + \overline{F}\mathbf{d}, \tag{3.46}$$

where $\tilde{\mathbf{u}}_r$ contains the displacement, velocity and acceleration components corresponding to each standing wave mode and $\overline{B}_r$ and $\overline{E}$ contain the appropriate forcing terms of (3.42). The expression for the output $\mathbf{y}$ is obtained by substituting the assumed expansions (3.33) and (3.34) into the linearised output definition $\mathbf{y} = C\mathbf{U}'$. Using the transformation (3.44) for each of the standing wave displacements, velocities and accelerations, we can replace $\tilde{\mathbf{u}}_r$ in (3.46) to obtain the resulting state-space system

$$\dot{\mathbf{v}} = \overline{A}\mathbf{v} + \overline{B}\tilde{\mathbf{u}} + \overline{E}\dot{\mathbf{d}} \qquad \mathbf{y} = \overline{C}\mathbf{v} + \overline{D}\tilde{\mathbf{u}} + \overline{F}\mathbf{d}, \tag{3.47}$$

where $\tilde{\mathbf{u}}$ now contains the displacements, velocities and accelerations of each blade. Note that both $\mathbf{q}(t)$, which is used for evaluating output, and $\ddot{\mathbf{q}}(t)$, which occurs in the forcing term, appear in the model. Similarly, the forcing term requires the evaluation of $\dot{\mathbf{d}}$. The matrix $\overline{A}$ is still block diagonal by interblade phase angle, however we now require the matrices $\overline{C}$, $\overline{D}$ and $\overline{F}$ to define the outputs, where the extra matrices $\overline{D}$ and $\overline{F}$ arise from the representation of the solution (3.32,3.34).

3.7 Reduced-Order Modelling Summary

Currently in aeroelastic analyses, influence coefficients are computed for imposed sinusoidal motion from a high-fidelity aerodynamic model. In this way a low order but accurate means of representing the aerodynamics in (2.2) is obtained. However these models are only valid at the frequency at which they were computed, and for a typical system in which the blade response contains a range of frequencies, these models are insufficient. The challenge has therefore been to develop aerodynamic models which are not only low order and high fidelity, but which also describe the aerodynamics over a range of frequencies. This can be achieved via reduced-order modelling in which appropriate CFD solutions are projected onto a reduced-space basis.

The eigenmodes of the system would be a desirable choice for basis vectors since they depend on the aerodynamic operator and capture all the possible dynamics. A reduced set can be constructed by considering only eigenvalues whose frequencies fall within the range of interest. However, eigen-problems of the type encountered in turbomachinery flows are too ill-conditioned numerically to be used. The singular vectors of the system are also operator dependent and are easy to compute, however it was found that hundreds of vectors per blade passage were required to get an accurate model. The proper orthogonal decomposition has been used very successfully to construct accurate models efficiently, however for a typical bladed disk, the cost of generating the snapshots can be high if a large frequency range is to be considered. Another issue with the POD approach is that it is necessary to determine the arbitrary set of sample frequencies. Typically some knowledge will be available on the range of frequencies expected to be present in the system response, and the POD will be sampled over this range. However, it is also necessary to choose exactly which frequencies will be sampled within this range. If samples are placed too far apart, important system dynamics may be missed; if they are placed too closely together, a large number of matrix factorisations and solves is necessary, thus the cost of generating the model will be high.

The Arnoldi method provides an excellent alternative to the eigenmode and POD approaches. The Arnoldi basis has the benefits of an eigenmode approach in that it models the dynamics of the original high-order system, but it is much more straightforward to compute. The basis is selected according to inputs of interest, which makes it very efficient, but since several vectors are calculated at each frequency, the model is much less sensitive to the choice of sample frequencies. The models are much cheaper to compute than those constructed using the POD since one matrix factorisation can be used to obtain many basis vectors. Results presented in the next chapter will show that these reduced-order models can capture the relevant system dynamics accurately with a huge reduction in the number of states.

Chapter 4

Reduced-Order Modelling of a Transonic Rotor

Reduced-order models have been developed for subsonic and transonic cascades undergoing general pitching and plunging motion. A variety of forced response cases have been considered to validate the models and determine the size of the resulting reduced-order state-space systems. Results will be presented in this chapter for the DFVLR L030-4 transonic rotor discussed in Chapter 2. This rotor is analysed in unsteady plunging motion for a twenty-blade configuration. Figure 4-1 shows the grid for two passages of the rotor. The steady-state flow has an inlet Mach number of 0.82 and was shown previously in Figure 2-9. A CFD analysis of the full rotor would have 287760 unknowns. With the resources available, routine computations of this size as required for design are not feasible. The results presented in this chapter will demonstrate that the system dynamics relevant to flutter and forced response can be accurately captured with less than two hundred states in the reduced-order model.

4.1 Aerodynamic Reduced-Order Models

To illustrate the application of different model order reduction techniques to a representative problem, reduced-order aerodynamic models were developed using both the POD and Arnoldi approaches.

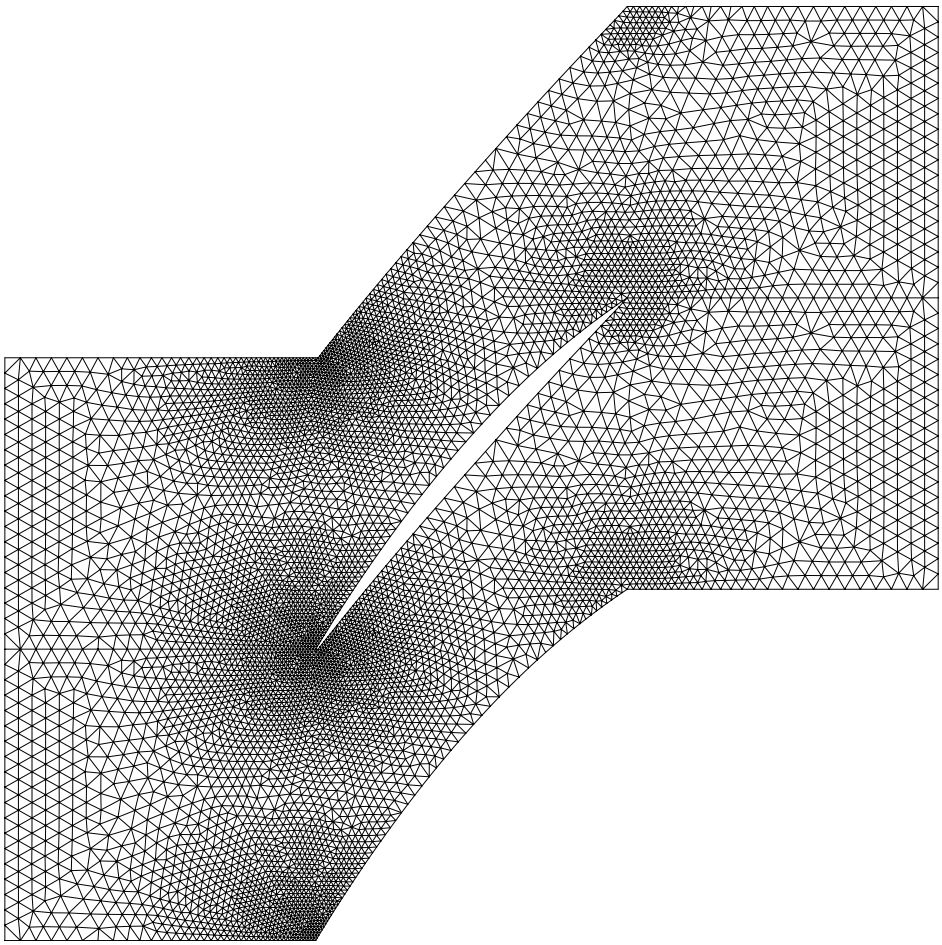

Figure 4-1: Computational domain for two passages of the DFVLR transonic rotor. 3668 nodes, 7040 triangles per blade passage.

4.1.1 POD Reduced-Order Model

To construct the POD model, twenty snapshots were obtained for each interblade phase angle, with samples being made at ten equally spaced reduced frequencies over the range $k = 0$ to $k = 1.22$ for a total of four hundred snapshots. This frequency range represents the low-frequency aerodynamics which are typically of interest in an aeroelastic analysis. The POD eigenvalue spectra for interblade phase angles of 0° and 180° are plotted in Figure 4-2. Note the log scale on the plot and the huge variation between the largest and smallest eigenvalues. The jth POD eigenvalue is an indication of how much flow energy is captured by the jth POD basis vector, and so this plot shows that only the first six or eight modes for each interblade phase angle are required to capture almost all of the system dynamics in this sample set. For these two interblade phase angles, choosing just the first six modes captures over 99% of the flow energy. The POD eigenvalues for the other interblade phase

angles show similar trends.

A reduced-order model was constructed using the first six POD basis vectors for each interblade phase angle. The eigenvalues of the reduced-order aerodynamic system were computed and are shown in Figure 4-3. We see that all eigenvalues have negative real parts, indicating that the aerodynamic system is stable.

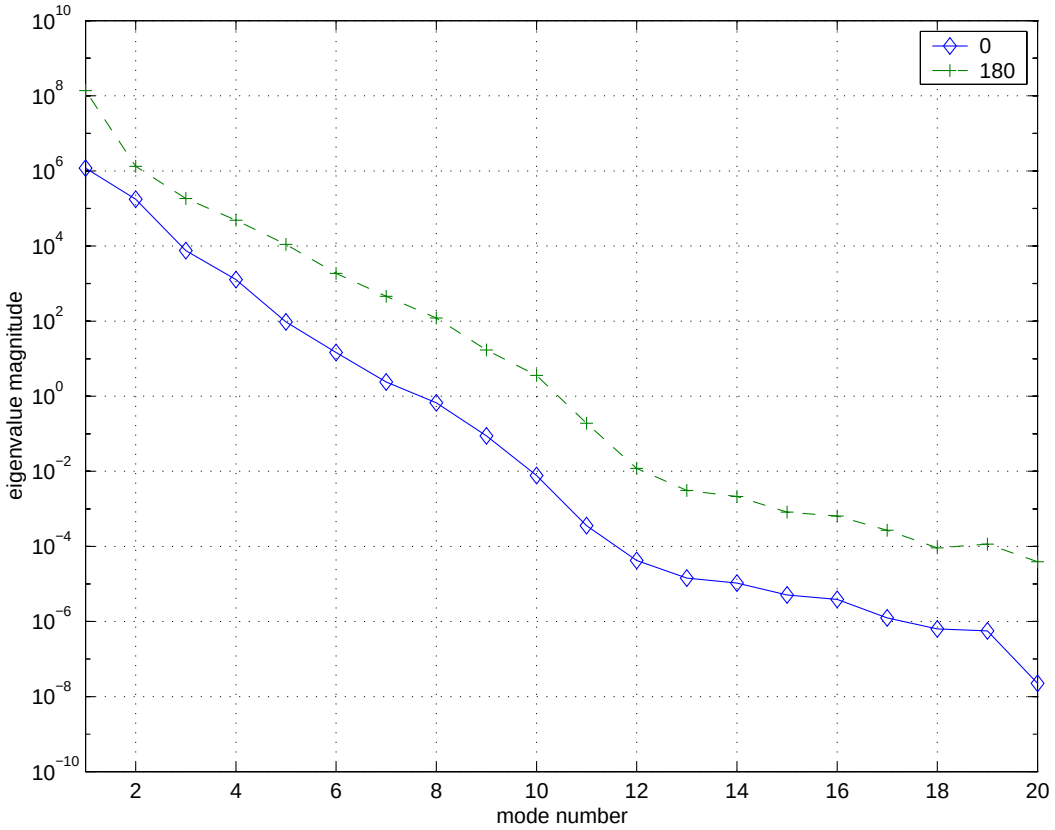

Figure 4-2: POD Eigenvalue spectra for transonic cascade in plunge. $M = 0.82$, $\sigma = 0°, 180°$.

4.1.2 Arnoldi Reduced-Order Model

The Arnoldi-based method was also used to compute a reduced-order model for the twenty-blade cascade. Six vectors were again chosen for each interblade phase angle, and all were computed about $s = 0$. The eigenvalues of the Arnoldi aerodynamic system are shown in Figure 4-4. The first thing we notice is that with exactly the same number of modes, the Arnoldi reduced-order model covers a much larger area of the complex plane, which suggests that it is capturing a greater portion of the dynamics. The eigenvalues of the Arnoldi reduced-order model should approximate those of

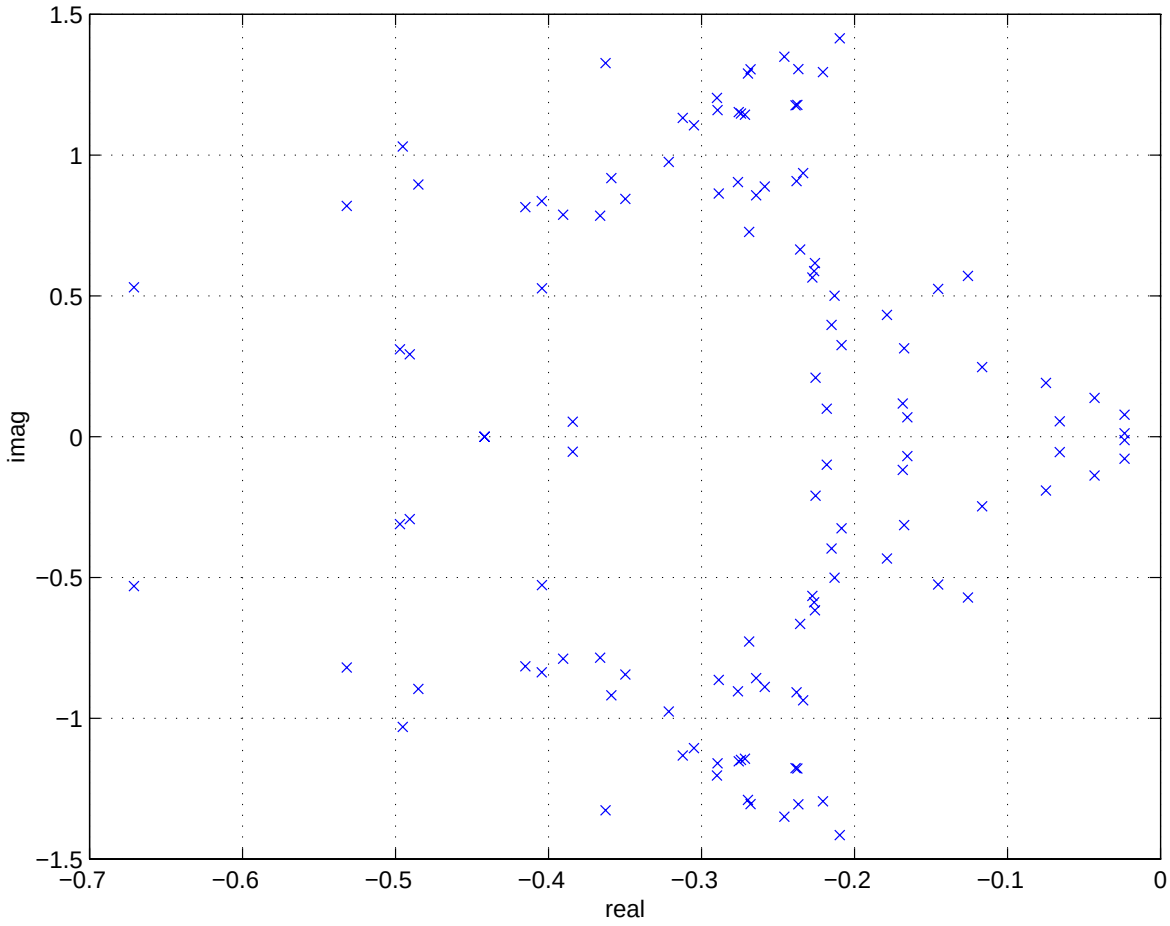

Figure 4-3: Eigenvalue spectrum for POD reduced-order aerodynamic system. Six modes per interblade phase angle (total 120 modes).

the original system since the Arnoldi vectors provide a good approximation of the eigenvectors of a sparse matrix [47]. While the POD model is valid only over the frequency range sampled to obtain the snapshots and taking more basis vectors does not add any further information (as shown by the POD eigenvalues in Figure 4-2), as we take more vectors in the Arnoldi basis we expect to obtain a model which represents a greater portion of the system dynamics. The eigenvalues towards the left of the plot fall into a distinctive parabolic shape which is typically associated with convective modes [41] and will be discussed in a subsequent section.

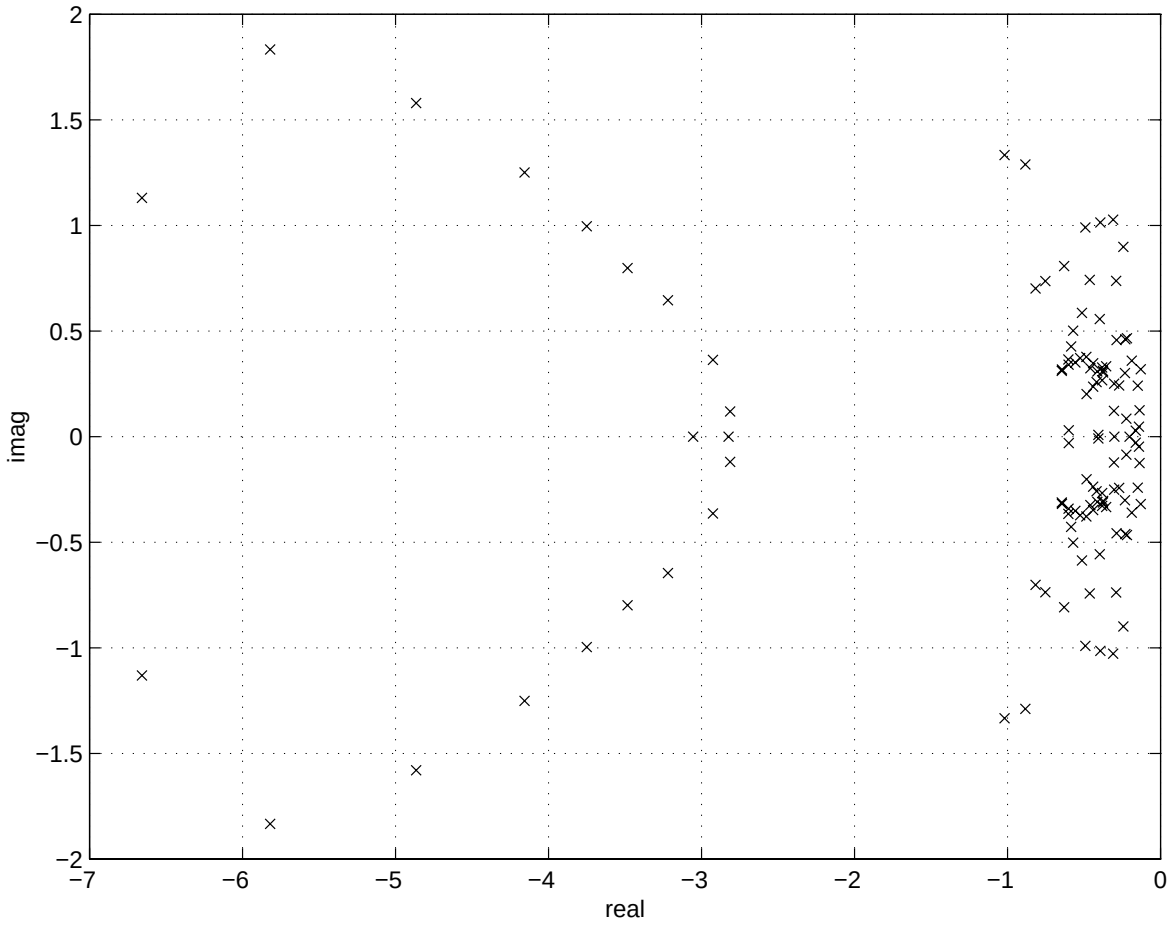

Figure 4-4: Eigenvalue spectrum for Arnoldi reduced order aerodynamic system. Six modes per interblade phase angle (total 120 modes). All basis vectors computed about $s = 0$.

4.2 Aerodynamic Forced Response

One question which must be addressed in the POD approach is that of choosing the sample frequencies. It is necessary to ensure that the appropriate range of frequencies are sampled, and also that sufficient samples are taken over this range. This question does not arise with the Arnoldi method, however it is still necessary to determine how many basis vectors must be included in the reduced-order model to obtain an accurate representation of the relevant system dynamics. Forced response of the cascade to a pulse input in plunge is a good way of answering both of these questions, since a pulse contains a continuous spectrum of temporal frequencies. Comparison of reduced-order model results with the full simulation code will determine both the required size of the reduced-order models, and also whether enough sample frequencies were used to construct the POD basis vectors.

The input takes the form

$$h(t) = e^{-g(t-t_0)^2} \tag{4.1}$$

where g is a parameter which determines how sharp the pulse is and thus the value of the highest significant frequency present. To determine the frequency content, a Fourier transform of (4.1) can be performed, also yielding a Gaussian:

$$H(\omega) = \frac{1}{2\sqrt{\pi g}} e^{i\omega t_0} e^{\frac{-\omega^2}{4g}}. \tag{4.2}$$

Since the linearised CFD simulation code is implemented in the time domain, for a general input the entire rotor would have to be considered. As mentioned, this is not a feasible computation. We are limited to solving the large system on just one or two blade passages. Accordingly, all twenty blades were supplied with the same input, which results in a motion containing only an interblade phase angle of zero. Since the solution will be the same in all passages, the time-domain linearised simulation can be performed on just a single passage. The input in blade plunge displacement is shown in Figure 4-5 for $g = 0.01$. The significant frequency content for this value of g is for $\omega < 0.56$ ($k < 0.68$). Above this frequency, the magnitude of the components are less than 0.001, and therefore deemed to be insignificant. This range of frequencies is well within that sampled by the POD.

The forced response calculated by each of the reduced-order models is plotted in Figures 4-6 and 4-7 and in each case is compared to the linearised CFD simulation code. We can see that with just six modes, both models do a very good job of predicting the response. Although the POD model calculates the force more accurately with four modes, with six modes it slightly underpredicts the force at the peaks, while the Arnoldi model is very close to the linearised simulation response. To

construct the POD model, twenty snapshots were obtained for $\sigma = 0°$ (ten matrix factorisations). In comparison, all the Arnoldi vectors were computed at a single frequency point ($s = 0$) and so could be obtained with a single matrix factorisation. For the cases shown here, the POD reduced-order model was a factor of ten times more expensive to compute than the Arnoldi reduced-order model (ten matrix factorisations versus one). Moreover, the Arnoldi model is as good, if not slightly better.

To further demonstrate the utility of the Arnoldi method, a pulse input with a value of $g = 0.1$ was considered. This pulse contains significant reduced frequencies in the range $k = 0$ to $k \simeq 1.6$, which is slightly outside the range sampled by the POD ($k = 0 \ldots 1.22$). By computing twelve Arnoldi basis vectors, a good agreement with the CFD result could be obtained (note that very little computational effort is required to compute these extra vectors since the matrix factorisation has already been obtained). For the POD model, it was found that taking more than eight basis vectors from the existing snapshot database created an unstable model. This is most likely due to numerical conditioning - beyond the first eight modes, the POD eigenvalues become relatively very small and numerical errors start to become significant. This is apparent through a gradual loss of orthogonality in the higher modes. To obtain a higher number of useful basis vectors, we would need to obtain more snapshots and repeat the POD analysis. For the purposes of comparing the existing available data, the POD reduced-order model was constructed using just eight modes which gives the best possible result for this snapshot collection. The forced response computed with the CFD code is plotted in Figure 4-8 along with results from the Arnoldi reduced-order model with twelve modes and the POD reduced-order model with eight modes. We see a much better agreement for the Arnoldi reduced-order model, although, again, both models do a reasonable job with the POD underpredicting the peak responses. To improve the reduced-order model performance, for the POD it would be necessary to include the higher frequency range when obtaining the snapshots, which will significantly increase the required number of system solves. For the Arnoldi, it would be possible to obtain a lower order model by deriving some of the Arnoldi vectors about a non-zero frequency point (in this case a value near $s = 1.6$ might be appropriate).

A case was then considered where just one blade was forced with the pulse input, while all others were held fixed. This motion contains all possible interblade phase angles. The response for each blade was computed using the Arnoldi reduced-order model with six modes for $\sigma = 0°$ and ten modes for all other σ. The inputs and response of each blade are shown in Figure 4-9. This computation was too expensive to be carried out with the linearised simulation code. It is clear from the plot that the largest force is generated on the disturbed blade and its nearest neighbours, as might be expected intuitively. We can see that beyond the two closest blades the force generated is very small.

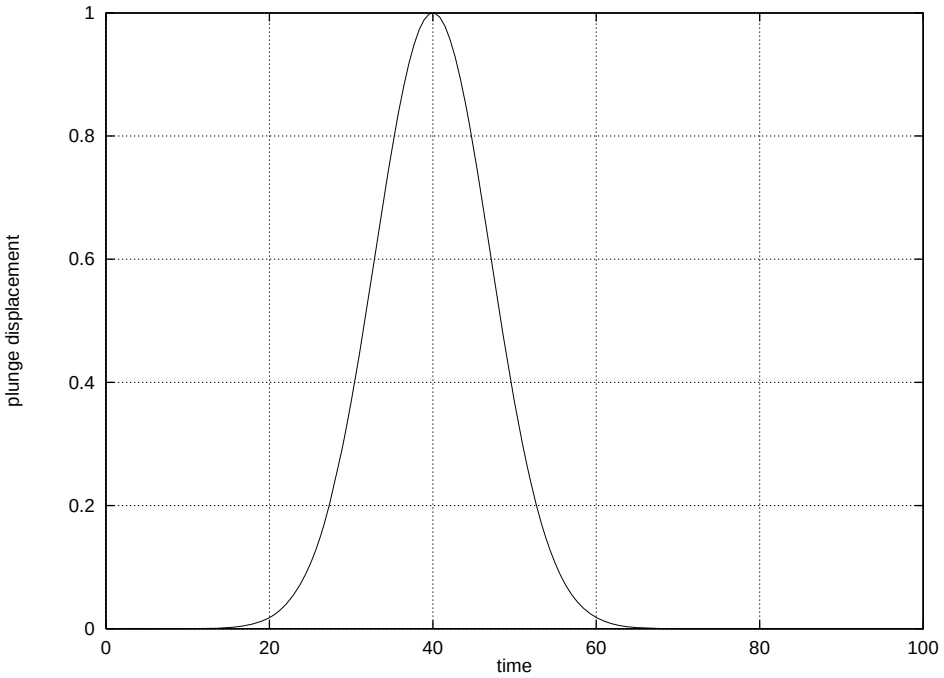

Figure 4-5: Pulse input in plunge, $g = 0.01$.

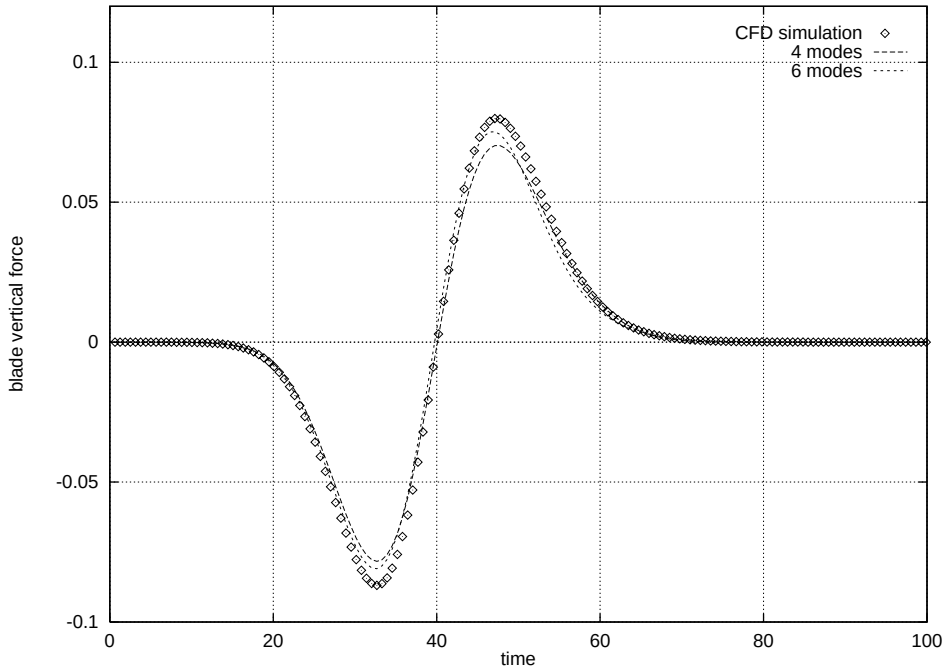

Figure 4-6: Pulse response for POD reduced-order model and linearised simulation code. $\sigma = 0°$, $g = 0.01$, $M = 0.82$.

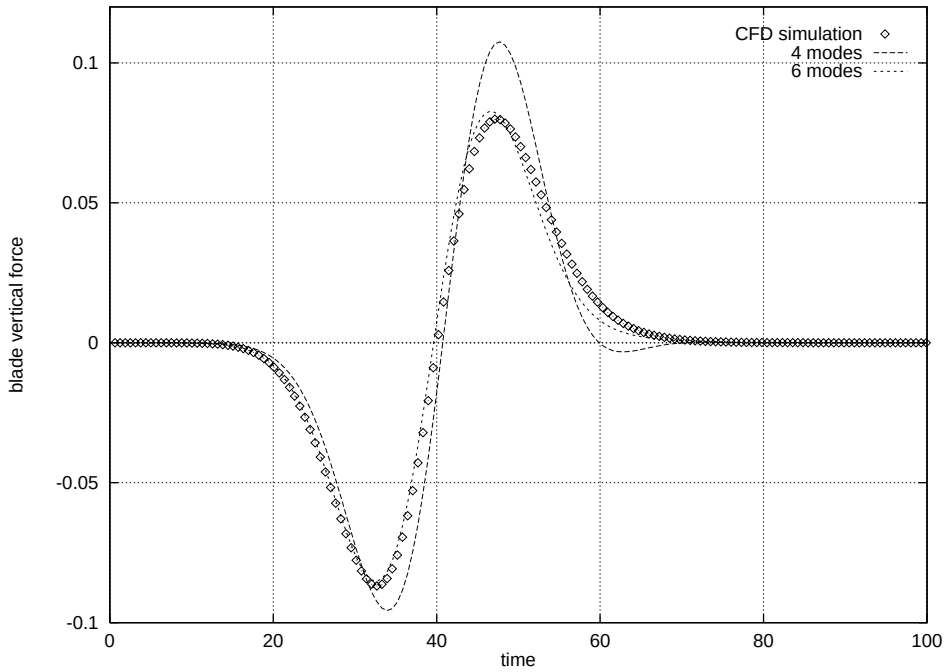

Figure 4-7: Pulse response for Arnoldi reduced-order model and linearised simulation code. $\sigma = 0°$, $g = 0.01$, $M = 0.82$.

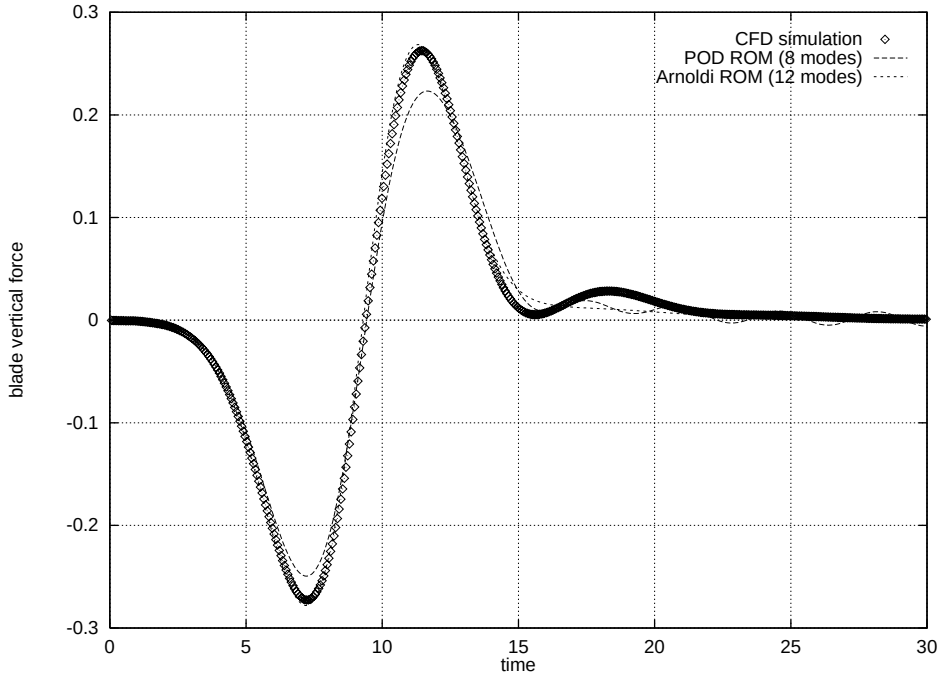

Figure 4-8: Pulse response for Arnoldi reduced-order model with 12 modes, POD reduced-order model with 8 modes and linearised simulation code. $\sigma = 0°$, $g = 0.1$, $M = 0.82$.

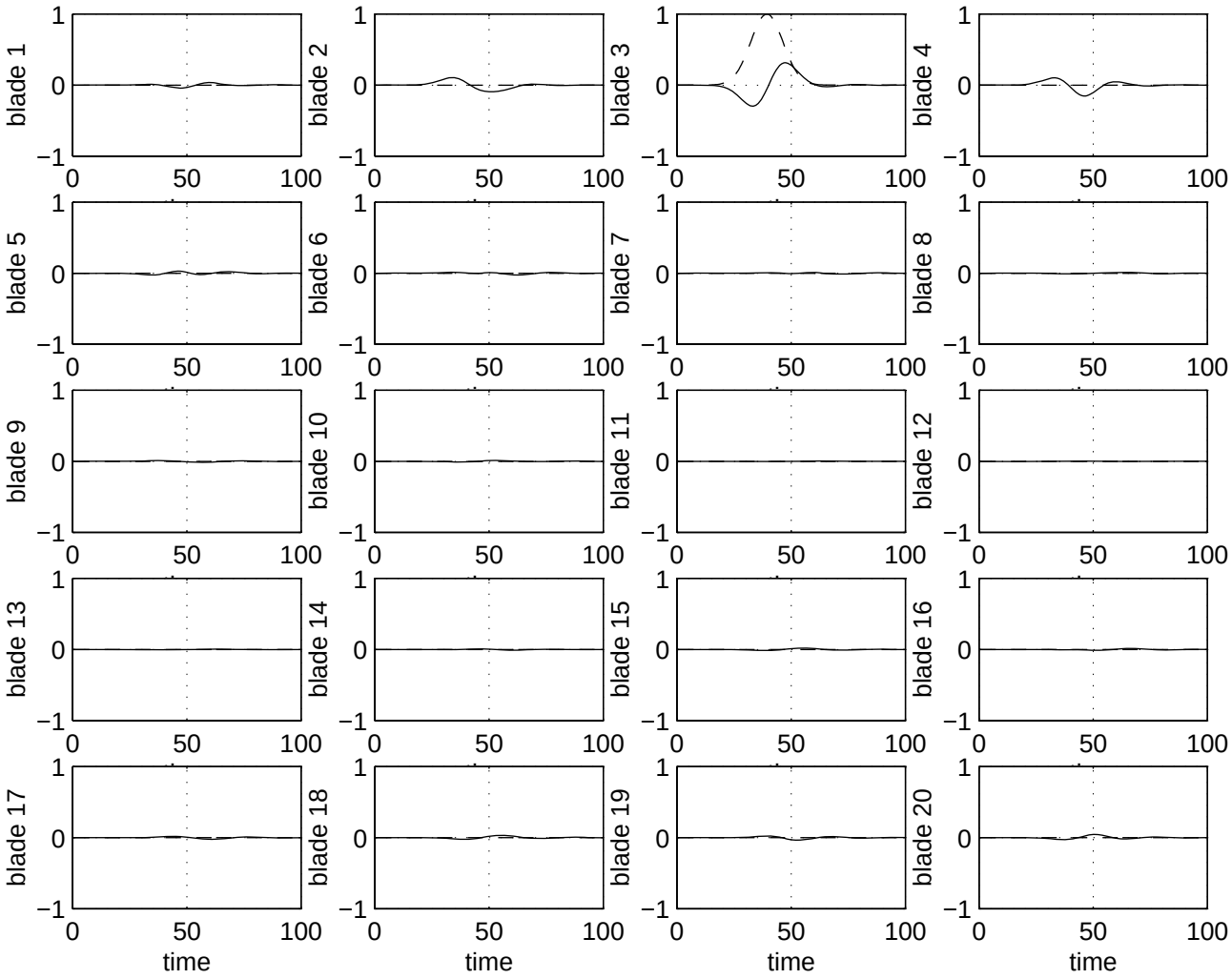

Figure 4-9: Pulse displacement input (dashed line) and blade lift force response (solid line) for Arnoldi reduced-order model. Six modes for $\sigma = 0°$ and ten modes for all other interblade phase angles (total 196 modes). $g = 0.01$, $M = 0.82$.

4.3 Coupled Aerodynamic/Structural Reduced-Order Model

To illustrate the incorporation of the reduced-order models to an aeroelastic framework, the aerodynamic systems were coupled to a mass-spring-damper structural system as described in Chapter 2. Recall the structural equations written as a first order system (2.50). For plunge only, the structural equations for each blade can be written

$$\frac{d}{dt}\begin{bmatrix} h_j \\ \dot{h}_j \end{bmatrix} = \begin{bmatrix} 0 & 1 \\ -(kM)^2 & -2kM\zeta \end{bmatrix}\begin{bmatrix} h_j \\ \dot{h}_j \end{bmatrix} + \begin{bmatrix} 0 \\ \frac{2M^2}{\pi\mu}C_l^j \end{bmatrix}, \tag{4.3}$$

or, as in (2.50), $\dot{\mathbf{u}} = S\mathbf{u}+T\mathbf{y}$. This structural model is then coupled to the reduced-order state-space system (3.38) (with no static corrections) as follows :

$$\begin{bmatrix} \dot{\mathbf{v}} \\ \dot{\mathbf{u}} \end{bmatrix} = \begin{bmatrix} A & B \\ TC & S \end{bmatrix}\begin{bmatrix} \mathbf{v} \\ \mathbf{u} \end{bmatrix} + \begin{bmatrix} E \\ 0 \end{bmatrix} d. \tag{4.4}$$

To determine aeroelastic stability, the eigenvalues of this coupled system are evaluated. For forced response analysis, the structural and aerodynamic equations can be solved simultaneously using (4.4) to determine the blade displacement and velocity and the aerodynamic forces and moments acting.

If static corrections are used, the coupling between the aerodynamic and structural models is a little more complicated, since in (3.47) the input vector $\tilde{\mathbf{u}}$ contains more quantities than the structural state vector $\mathbf{u}$. Since the forcing term $\overline{B}\tilde{\mathbf{u}}$ only involves $\dot{\mathbf{q}}$ and $\ddot{\mathbf{q}}$ and the output term $\overline{D}\tilde{\mathbf{u}}$ only involves $\mathbf{q}$ and $\dot{\mathbf{q}}$, (3.47) could be rewritten as

$$\dot{\mathbf{v}} = \overline{A}\mathbf{v} + \tilde{B}\dot{\mathbf{u}} + \overline{E}\dot{d} \qquad\qquad \mathbf{y} = \overline{C}\mathbf{v} + \tilde{D}\mathbf{u} + \overline{F}d, \tag{4.5}$$

where $\mathbf{u} = [\mathbf{q}\ \dot{\mathbf{q}}]^T$ is now the structural state vector, and the matrices $\tilde{B}$ and $\tilde{D}$ correspond directly to $\overline{B}$ and $\overline{D}$ in (3.47) but with the appropriate columns of zeros removed. The coupled system can then be written

$$\begin{bmatrix} \dot{\mathbf{v}} \\ \dot{\mathbf{u}} \end{bmatrix} = \begin{bmatrix} I & -\tilde{B} \\ 0 & I \end{bmatrix}^{-1}\begin{bmatrix} \overline{A} & 0 \\ T\overline{C} & S+T\tilde{D} \end{bmatrix}\begin{bmatrix} \mathbf{v} \\ \mathbf{u} \end{bmatrix} + \begin{bmatrix} \overline{E}\dot{d} \\ \overline{F}d \end{bmatrix}. \tag{4.6}$$

To provide an example of an aeroelastic system, an Arnoldi reduced-order aerodynamic model with 196 aerodynamic states was coupled to a structural model with a reduced frequency of $k = 0.25$, no structural damping ($\zeta = 0$) and a mass ratio of $\mu = 100$. These structural parameters are typical for a rotor blade. The eigenvalues of the coupled system (4.4) are shown in 4-10 along with the original

aerodynamic eigenvalues. We observe some movement of the original aerodynamic eigenvalues due to interaction with the structure, and also the introduction of forty structural modes with frequencies around $kM = 0.205$. A zoom of these structural eigenvalues is shown in Figure 4-11. The number above each structural eigenvalue identifies the nodal diameter to which it corresponds. For a nodal diameter ℓ, the corresponding interblade phase angle is $\sigma_\ell = 2\pi\ell/r$ (here we have $r = 20$ blades). If we consider just the structural equation (4.3) with no aerodynamics, the resulting solution is the same for all blades, and is a damped (in the general case with structural damping) sinusoidal motion at the blade natural frequency. This so-called *in-vacuo* mode has all structural eigenvalues at the conjugate points $-\zeta kM \pm ikM\sqrt{1-\zeta^2}$. Coupling in the aerodynamics to equation (4.3) causes the structural eigenvalues to move from this point, and so the response of the coupled system contains a range of frequencies around the damped natural frequency $kM\sqrt{1-\zeta^2}$. The amount of eigenvalue scattering, and hence the range of frequencies present in the response, depends on the amount of coupling between the aerodynamics and the structure. By examining the forcing term in equation (4.3) we see that there are several factors which affect this coupling. We first non-dimensionalise time in (4.3) by $t = t'/kM$, so that the equation of motion for blade j can be written

$$h_j'' + 2\zeta h_j' + h_j = \frac{2C_l^j}{\pi\mu k^2} \tag{4.7}$$

and the blade natural frequency is now unity. The size of the forcing term is affected by both the aerodynamics and the structural properties of the blades. For systems with a high degree of aerodynamic coupling, a small motion of the blade will create a large force and the C_l^j term will be relatively large. The structural parameters enter through the natural reduced frequency k and the blade mass ratio μ. For a massive blade (high values of μ), the aerodynamics do not have a significant effect, and the structural eigenvalues will be tightly clustered around the natural frequency. In the limit $\mu \to \infty$ (an extremely massive blade) the aerodynamics will have no effect on the structure, and the response will be in the in-vacuo mode. Similarly, we see a higher degree of coupling for low values of natural frequency. Figure 4-11 shows that in this case, even though the blade natural frequency is fairly low, a small degree of aerodynamic coupling is present in the system. For the most part, the eigenvalues fall very close to the natural frequency. Even the $\ell = 8$ mode, which exhibits the most coupling, has a frequency shift of less than 4%.

We can gain some insight to the motion of the structural eigenvalues by considering the work per cycle of the cascade. The work per cycle was calculated for each interblade phase angle over the frequency range $k = 0$ to $k = 1.2$ and is plotted in Figure 4-12. The work per cycle represents the aerodynamic damping and hence the relative motion of the real parts of the structural eigenvalues. The relevant aerodynamic damping to consider is that in the region near the natural frequency.

Three slices of the work per cycle surface near $k = 0.25$ are shown in Figure 4-13. This figure shows that for reduced frequencies near $k = 0.25$, modes six through twelve (interblade phase angles 108° though 216°) have the most negative values of work per cycle, and the corresponding eigenvalues in Figure 4-11 are the most highly damped. Similarly, the work per cycle analysis predicts that the interblade phase angles close to $\sigma = 0°$ are lightly damped, as is also the case in the eigenvalue spectrum.

To demonstrate forced response prediction, a time-marching simulation of the coupled system was run with $k = 0.25$ and $\zeta = 0$. An initial plunge displacement was applied to one of the blades, then the structural and aerodynamic response for the entire rotor was computed. Figure 4-14 shows the resulting displacement and vertical component force for each blade. Clearly the disturbed blade (blade 3) exhibits the largest response, and induces some motion in nearby blades. The resulting motion is decaying, although slowly since the coupled system is lightly damped.

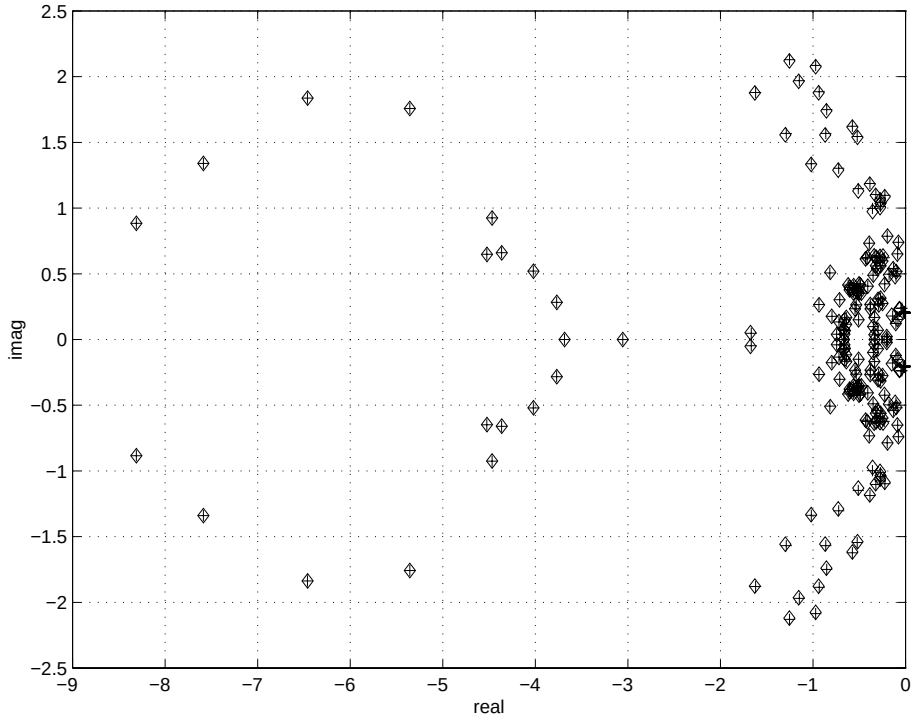

Figure 4-10: Eigenvalue spectrum for Arnoldi reduced-order model. Purely aerodynamic eigenvalues (diamonds) and coupled aerodynamic/structural system (plus signs). 196 aerodynamic states, 40 structural states. $M = 0.82$, $\mu = 100, k = 0.25, \zeta = 0$.

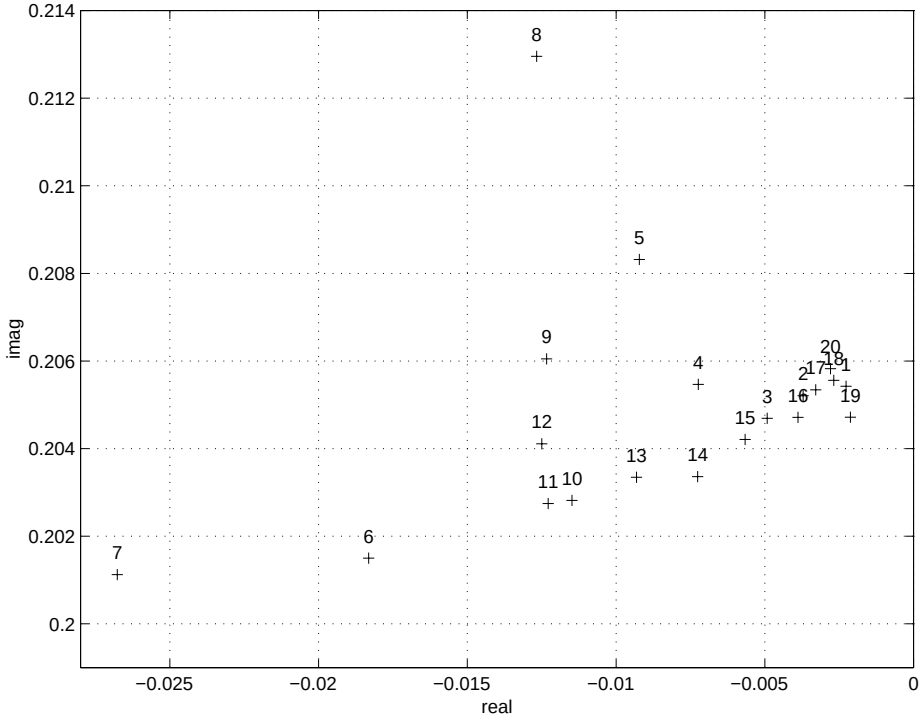

Figure 4-11: Zoom of structural eigenvalues. Eigenvalues are numbered by nodal diameter. $M = 0.82$, $\mu = 100, k = 0.25, \zeta = 0$.

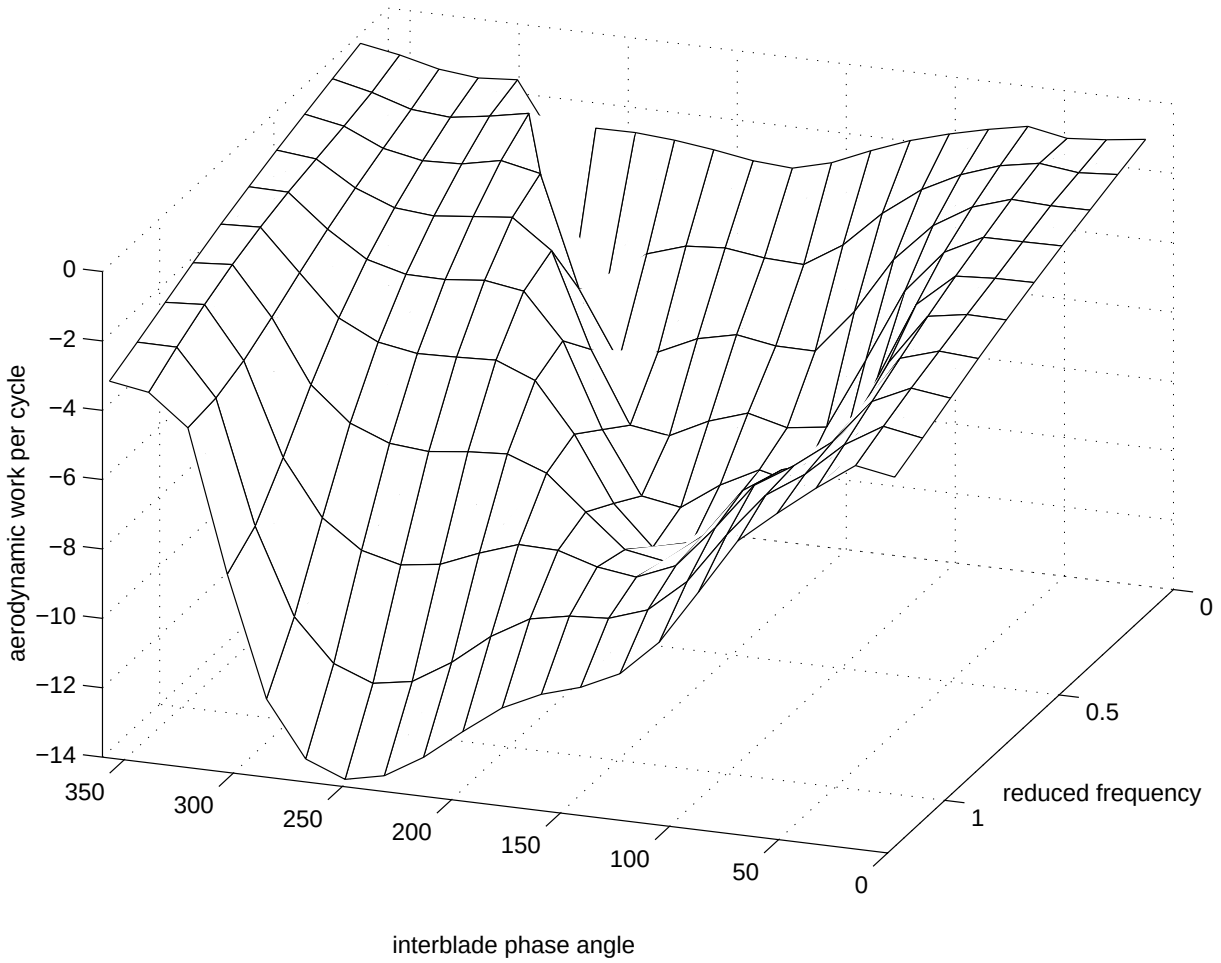

Figure 4-12: Aerodynamic work per cycle as a function of interblade phase angle and reduced frequency for transonic rotor.

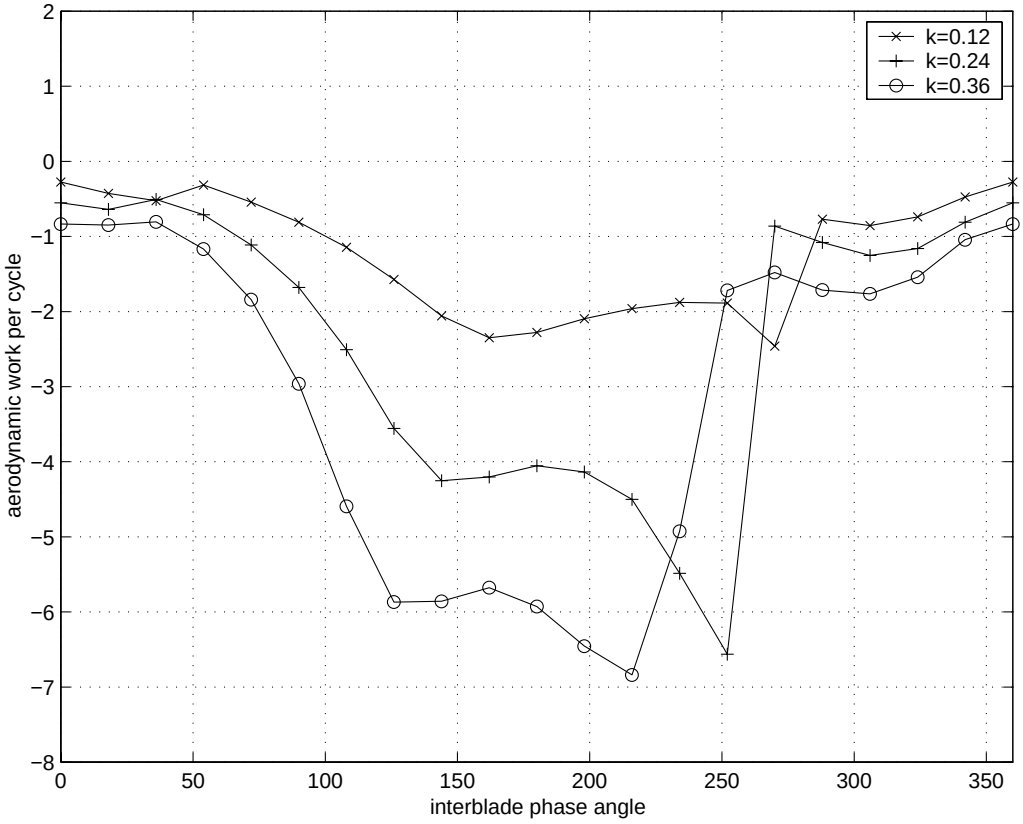

Figure 4-13: Aerodynamic work per cycle as a function of interblade phase angle for reduced frequencies of $k = 0.12, 0.24, 0.36$.

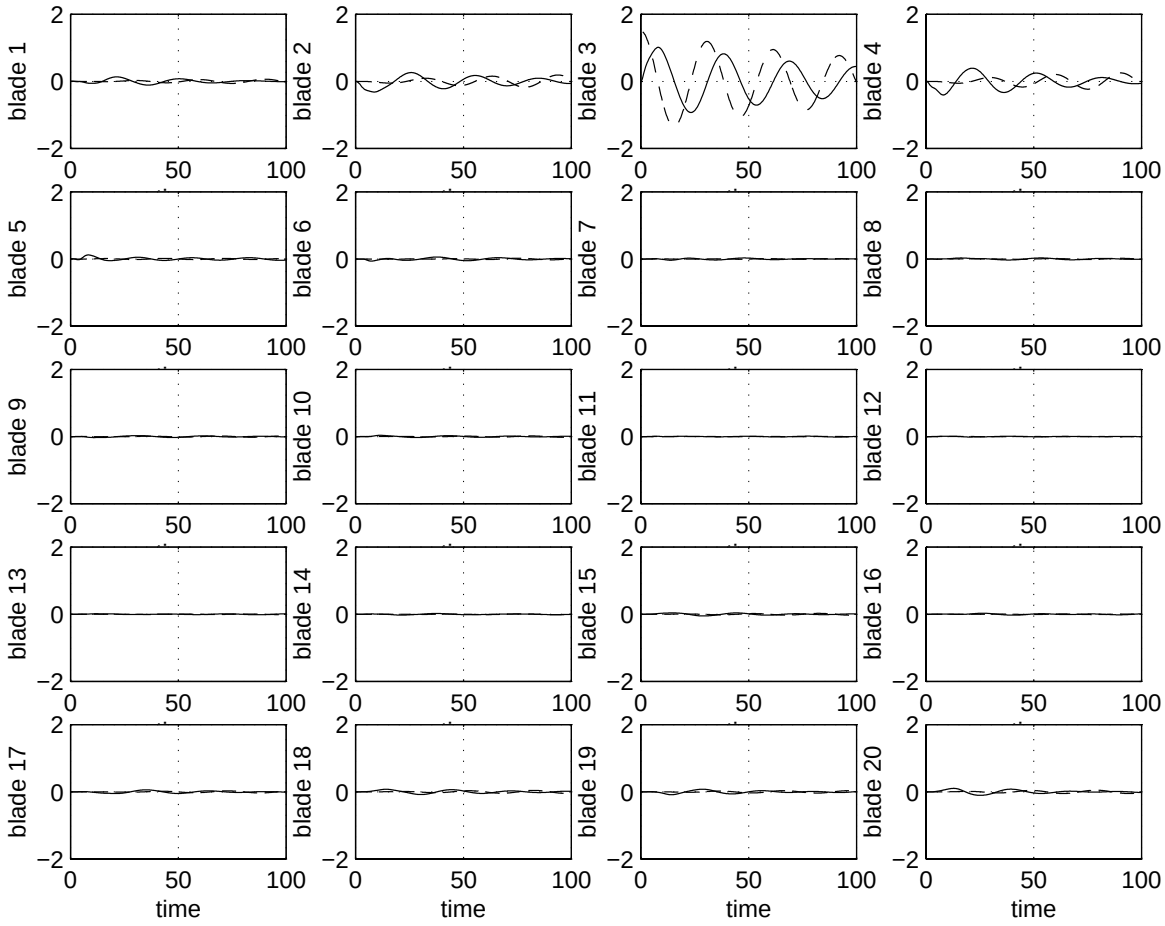

Figure 4-14: Coupled system response to an initial plunge displacement input at blade 3 : blade displacement (dashed line) and blade vertical force (solid line). $\mu = 100, k = 0.25, \zeta = 0$.

4.4 Comparison of POD with Influence Coefficient Model

In this section, results from a POD reduced-order model will be compared to an influence coefficient model. The two approaches are very similar in that both models are derived by considering solutions of the CFD system at frequencies of interest. In fact, the influence coefficient model is a simplified reduced-order model with just a single snapshot at the blade natural frequency. Since with the POD we are increasing the cost of deriving the model by considering several frequencies, it is desirable to determine how much additional accuracy is gained. If the influence model is able to capture the relevant dynamics to the desired level of accuracy, then there would be no reason to develop a more costly reduced-order model. The ability of each model to capture the dynamics of the coupled system relevant to predicting flutter and forced response will be assessed. This is achieved by considering the stability margins of the resulting aeroelastic systems (eigenvalues) and also the forced response to an axial velocity disturbance at the passage inlet.

The aeroelastic influence coefficient model has a very simple form. We simply replace the aerodynamic forces on the right-hand side of (4.3) with the appropriate coefficients. Thus the equation for blade j becomes

$$\ddot{h}_j + 2\zeta kM\dot{h}_j + (kM)^2 h_j = \frac{2M^2}{\pi\mu}\left[\sum_{k=1}^{r}\left(\gamma_{jk}h_k + \epsilon_{jk}\dot{h}_k\right) + \beta_{j\ell}d_\ell\right] \tag{4.8}$$

where γ_{jk}, ϵ_{jk} and $\beta_{j\ell}$ are the influence coefficients calculated at the assumed frequency. γ_{jk} and ϵ_{jk} represent the force generated on blade j due to a unit plunge displacement and unit plunge velocity respectively of blade k. Similarly, $\beta_{j\ell}$ represents the force generated on blade j due to a unit disturbance in the ℓth nodal diameter.

The case chosen for analysis has structural parameters $\mu = 100$, $k = 0.12$ and $\zeta = 0$ which are typical for a compressor rotor blade. The natural frequency of the blade is thus $\omega_n = kM = 0.1$. A POD model was generated with snapshots taken at frequencies 90, 95, 100, 105, 110, 150, and 200 percent of the blade structural frequency. Aerodynamic influence coefficients were calculated at the blade natural frequency. The eigenvalues of the aerodynamic reduced-order model with four POD modes per blade passage (a total of 80 aerodynamic states), and the coupled aeroelastic reduced-order model (with a total of 120 states) were computed and are shown in Figure 4-15. Once again, when the structural model is coupled in, we see some movement of the original aerodynamic eigenvalues, plus the introduction of forty structural modes near the natural frequency $w_n = 0.1$. A zoom of these structural eigenvalues is shown in Figure 4-16, along with the eigenvalues for the influence coefficient model. The numbers on the plot indicate the number of nodal diameters associated with

each eigenmode. For ℓ nodal diameters, the corresponding interblade phase angle is $\sigma_\ell = 2\pi\ell/20$. For each interblade phase angle, Figure 4-16 shows two eigenvalues : that for the reduced-order model (the diamonds) and that for the influence coefficient model evaluated at the blade natural frequency (the plus signs). We notice that there is not a particularly high degree of aerodynamic coupling in the system, since for most modes the eigenvalues do not move far from the natural frequency of 0.1. The real and imaginary parts of these eigenvalues are also plotted in Figure 4-17 for each mode. For the most part, the agreement between the two models is very good. Figure 4-17 shows that there are two regions where the damping of the modes is not predicted accurately by the influence coefficient model. The first is for the modes whose frequency is far from the natural frequency (modes fifteen through seventeen), while the second is when the damping is high (modes eight through eleven). These cases both represent situations where the actual response conditions are not close to those assumed in the influence coefficient calculation. When the frequency of the eigenvalue changes significantly, we would not expect the influence coefficients to capture the dynamics accurately, because effectively they have been evaluated at the wrong point. Also, because the influence coefficient model assumes undamped sinusoidal motion, it cannot capture the system dynamics accurately when a high degree of damping is present, even if the frequency shift is very small.

To obtain a better estimation of the dynamics, each influence coefficient should be re-evaluated at the frequency corresponding to its eigenvalue, although some error will still exist for the highly damped modes. Coefficients were recalculated at $\omega_c = 0.09$ and the resulting eigenvalue for the $\ell = 15$ mode is plotted on Figure 4-16 as an asterisk. The Figure shows that the new eigenvalue has moved much closer to that predicted by the reduced-order model. In Figure 4-17 we can see that the damping of the $\ell = 15$ mode for the $\omega_c = 0.09$ model now agrees very closely with the reduced-order model, but that the damping prediction for the other modes is much worse, since $\omega = 0.09$ is a worse choice of sample frequency for them. If a greater degree of aerodynamic coupling, and thus more scatter in the modal frequencies existed, the influence coefficient model would not accurately capture a significant portion of the system dynamics. However the reduced-order model is able to accurately model the system even when a high degree of coupling exists.

To determine the accuracy of the reduced-order model, the blade force response was calculated for sinusoidal blade motion over a range of frequencies, and is plotted as solid lines in Figure 4-18 for interblade phase angles of 90°, 180° and 270°. The points on each of the plots are the force calculated using the linearised CFD model at frequencies corresponding to the POD snapshot sample points. These values represent the truth model. For interblade phase angles of 90° and 180° the reduced-

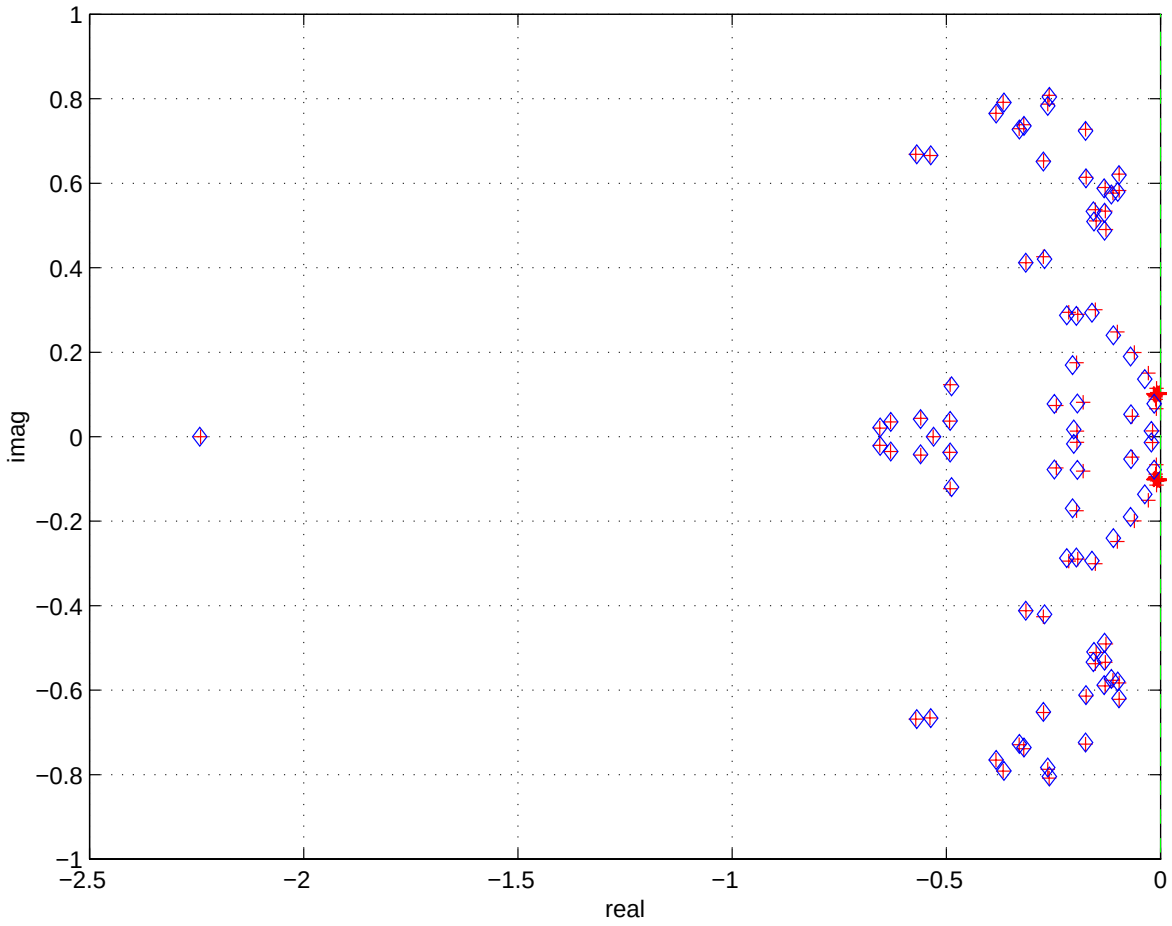

Figure 4-15: Eigenvalues for POD reduced-order model. Purely aerodynamic eigenvalues (diamonds) and coupled aerodynamic/structural system (plus signs). 80 aerodynamic states, 40 structural states. $\mu = 100$, $k = 0.12$, $\zeta = 0$.

order model does an excellent job of capturing the system dynamics over the entire frequency range. For 270°, a local resonance exists near $\omega = 0.15$ which is not fully captured by the reduced-order model. If more POD modes were included in the model, we would expect to then capture these dynamics more accurately. The dotted lines on the three plots represent the value of the force which would be predicted using the influence coefficient model derived at $\omega_c = 0.1$. Although this model is exact at this particular frequency, since the dynamics are assumed to be constant it does not capture any of the important variations with frequency. In addition, the assumption of a sinusoidally time-varying motion in the influence coefficient model is extremely restrictive. The reduced-order model can resolve any general motion, provided the relevant frequency range is sampled by the snapshots.

The response of the aeroelastic system to a sinusoidally time-varying axial velocity disturbance at

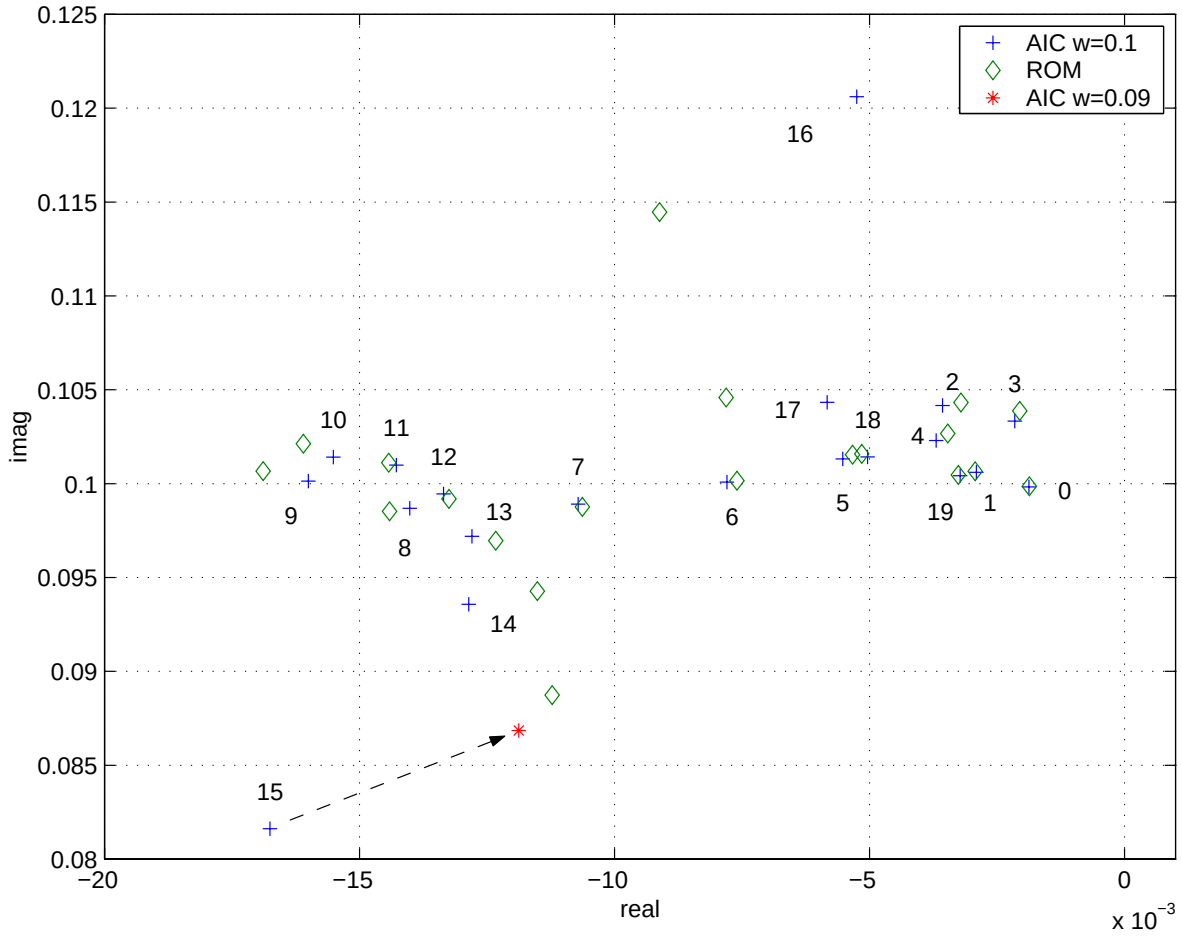

Figure 4-16: Structural eigenvalues for reduced-order model and aerodynamic influence coefficient model evaluated at $\omega_c = \omega_n = 0.1$. Also shown is the $\ell = 15$ eigenvalue for influence coefficients evaluated at $\omega = 0.09$. Structural parameters : $\mu = 100$, $k = 0.12$, $\zeta = 0$. Eigenvalues are numbered by their nodal diameter.

the inlet was then calculated. This disturbance was considered to be in the $\ell = 15$ spatial mode, whose dynamics were not well captured by the original influence coefficient model. Figures 4-19 and 4-20 show the blade displacement and force response over a range of frequencies for the reduced-order model and the influence coefficients calculated at $\omega_c = 0.1$ and 0.09. The $\omega = 0.1$ influence coefficient model underpredicts the response and also predicts the peak amplitude to be at the wrong frequency. This is because both the damping and the frequency of the eigenvalue were incorrect. The recalculated influence coefficients and the reduced-order model agree much more closely, although the reduced-order model predicts a slightly more damped response at lower frequencies. Even when the eigenvalue is predicted accurately, the influence coefficient model only predicts the forced response

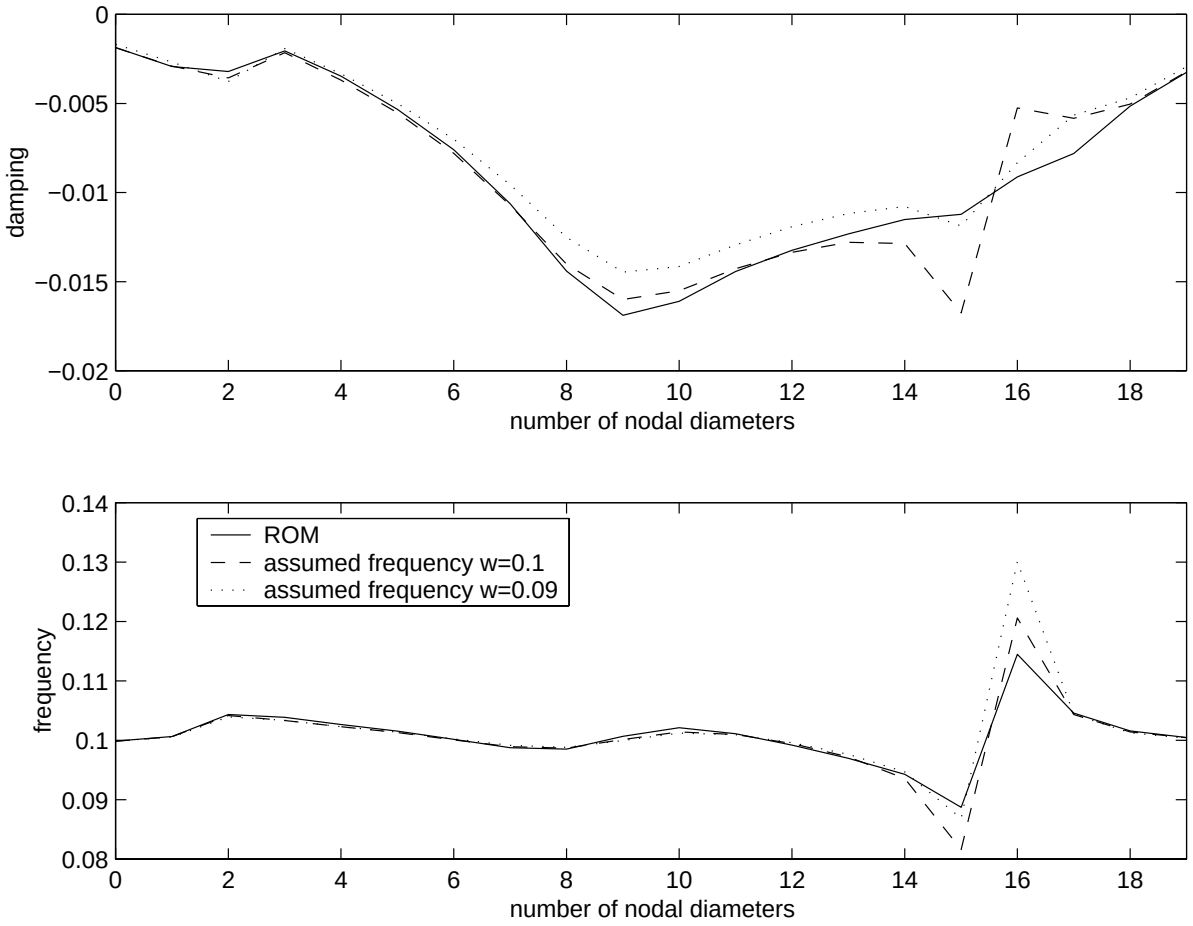

Figure 4-17: Damping and frequency of structural modes for reduced-order model and influence coefficient models at $\omega_c = 0.1$ and $\omega_c = 0.09$. $\mu = 100$, $k = 0.12$, $\zeta = 0$.

exactly at the assumed frequency where $\beta_{j\ell}$ in (4.8) was evaluated. As we move away from the assumed frequency, an error will be incurred in the forced response calculation. This can be seen in Figures 4-19 and 4-20 since the reduced-order model and influence coefficient model at an assumed frequency of 0.09 agree at the assumed frequency but differ away from it. Moreover, if the inlet disturbance were not sinusoidal in time, the influence coefficient model would be even less accurate.

We note the interesting fact that the force on the blades goes to zero at the blade natural frequency, yet it is still possible to have a non-zero displacement response. This can be seen by considering the structural equation (4.3). For no structural damping, response at $\omega = kM$ is in the blade alone mode, and the forcing term is zero.

In summary, these results demonstrate that for prediction of flutter and forced response, the situ-

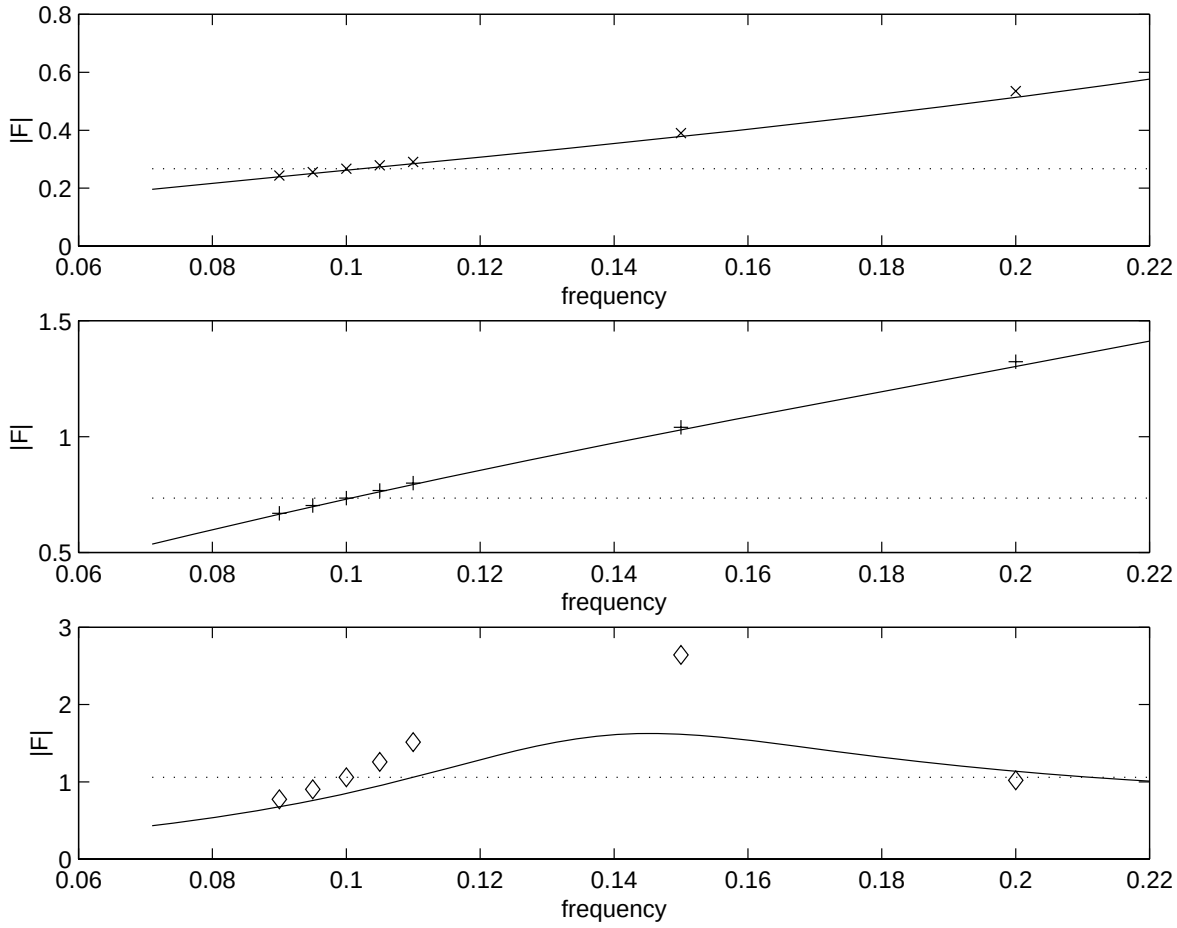

Figure 4-18: Blade force response amplitude to imposed sinusoidal motion. Reduced-order model prediction (solid lines), influence coefficient model prediction (dotted lines) and CFD solution (crosses, plus signs and diamonds). From the top : $\sigma = 90°$, $\sigma = 180°$ and $\sigma = 270°$.

ation is often such that a simple assumed-frequency method cannot model the relevant dynamics accurately. If a significant frequency shift from the blade natural frequency occurs (here a 10% shift was significant), or a moderate amount of aerodynamic damping is present, the stability margin of the aeroelastic system can be predicted inaccurately. In the case of a frequency shift, the influence coefficients could be recalculated at the new frequency, however this must be applied iteratively to each mode, and also cannot account for the presence of aerodynamic damping. Even when the eigenvalue is predicted correctly, the forced response calculated using the influence coefficient model is only precise at the assumed frequency. If the frequency of the disturbance varies from this point, a significant error may be incurred. Moreover, this error will be even greater if the disturbance is not sinusoidal.

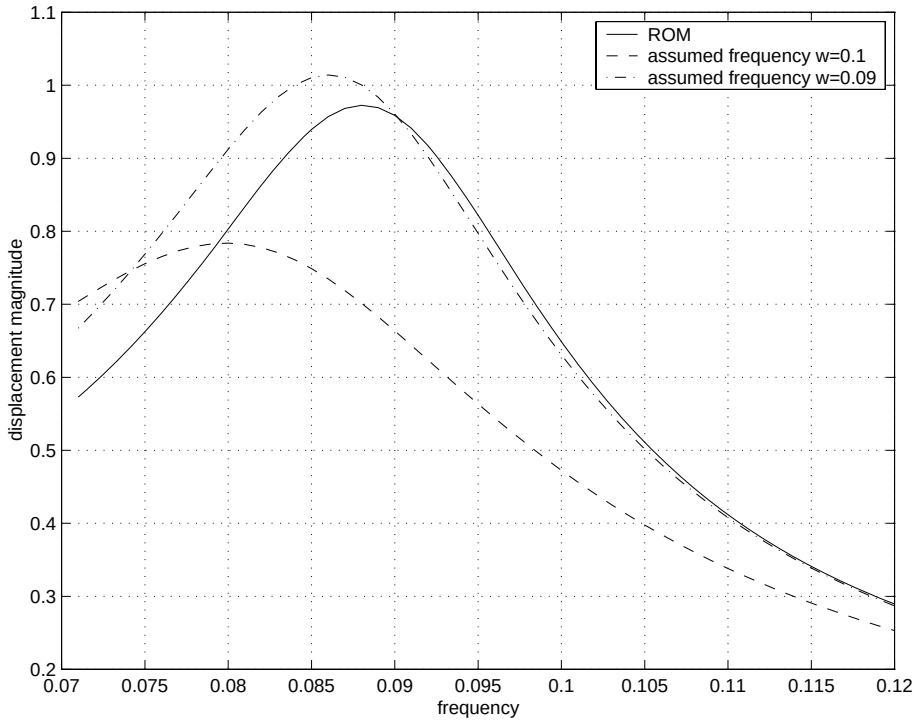

Figure 4-19: Blade displacement response amplitude to a sinusoidal axial velocity disturbance at the passage inlet. $\sigma = 270°$.

In terms of cost, the POD model used here required seven system solves for each interblade phase angle to obtain the snapshots, while the influence coefficients required just one. We have therefore traded computational expense for a model which predicts the relevant dynamics more accurately over a range of inputs. Although seven times more expensive than the assumed-frequency approach, the POD reduced-order model is still very cheap to compute when compared with other high-fidelity analyses (such as CFD models). We also note that if the Arnoldi approach were used, basis vectors could be computed about the blade natural frequency. The Arnoldi model would therefore require approximately the same computation cost (one matrix factorisation per interblade angle) as the influence coefficient model, yet it would provide high-fidelity dynamics. In future research, Arnoldi models about non-zero frequency points will be developed and applied to problems such as that presented here.

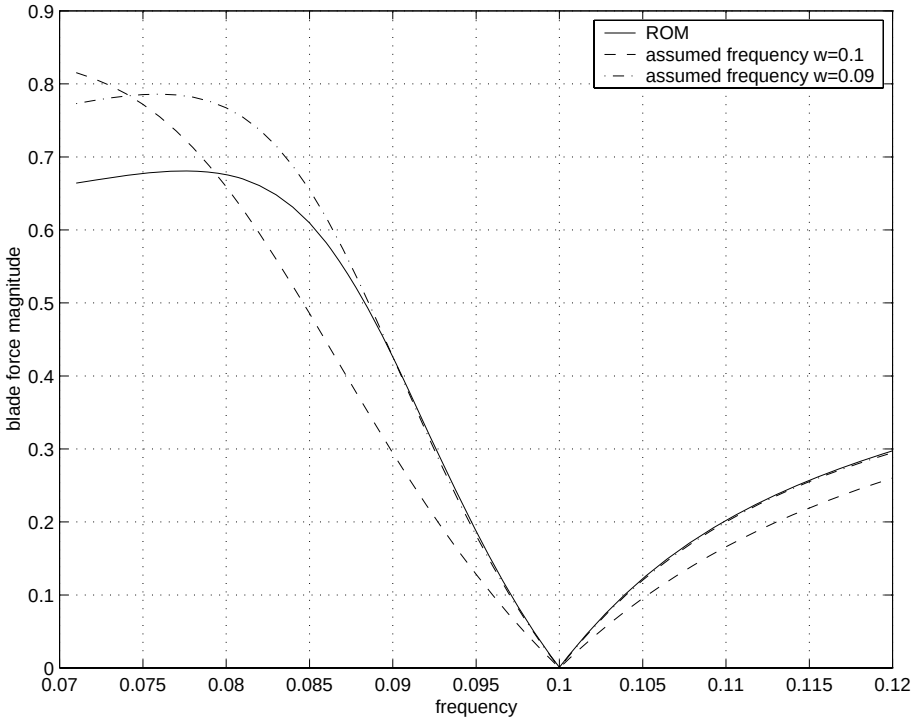

Figure 4-20: Blade force response amplitude to a sinusoidal axial velocity disturbance at the passage inlet. $\sigma = 270°$.

4.5 Physical Mode Identification

The eigenmodes of the large linear system (2.24), if they were available, could provide useful insight to physical mechanisms present in the flow. The Arnoldi-based reduction produces a model which should approximate the important eigenmodes of the original system, and thus may also allow some insight to be gained. The aerodynamic eigenvalues of the Arnoldi reduced-order model for the transonic twenty-blade rotor were shown in Figure 4-4. The most noticeable feature of the spectrum is the parabolic distribution towards the left of the plot. This parabolic shape has also been observed in the eigenmodes of the flow around a circular cylinder [41] and was identified with convection in the wake. The physical nature of these modes can be determined by animating them in time.

Consider an eigenvector $\mathbf{V}$ and corresponding eigenvalue λ of the reduced-order system (3.38). The flow vector corresponding to this eigenmode can be constructed by considering the projection (3.33), where the modal coefficients v_i are given by the components of the eigenvector $\mathbf{V}$. The perturbation flow solution can therefore be written as a linear combination of q basis vectors:

$$\mathbf{U}'(t) = Re\{\sum_{j=1}^{q} V_j \mathbf{\Psi}_j e^{\lambda t}\}. \tag{4.9}$$

For a complex eigenvalue $\lambda = -\mu + i\omega$, the flow solution therefore varies sinusoidally in time with a decaying amplitude, and this perturbation can be written

$$\mathbf{U}'(t) = Re\{e^{-\mu t}\sum_{j=1}^{q} V_j \mathbf{\Psi}_j e^{i\omega t}\}. \tag{4.10}$$

The eigenmodes which fall in the parabolic cluster have a special relationship between their frequency and damping. For an eigenvalue $\lambda = -\mu + i\omega$, the frequency varies with the square root of the damping, $\omega \sim \pm\sqrt{-\mu}$. In [41] this relationship is identified with travelling waves which solve the linear convection-diffusion equation. In one dimension, this equation roughly models the convection and dissipation of a perturbation in the wake. For the case of plunging blades considered here, the parabolic eigenvalues are thought to be associated with the shedding of vorticity off the blades.

These eigenvalues are shown in Figure 4-21 along with their corresponding nodal diameter. The parabola contains eigenvalues for all interblade phase angles except zero, and the lowest modes $\ell = 1$ and $\ell = 19$ do not conform to the parabola shape. The damping is a minimum for $\sigma = 180°$ and increases steadily for the lower modes. The mode corresponding to $\ell = 2$ ($\sigma = 36°$) was selected for analysis. The flow solution was computed at various instants in time using (4.10) with a unit amplitude that does not decay in time. The perturbation vorticity contours for the solution at

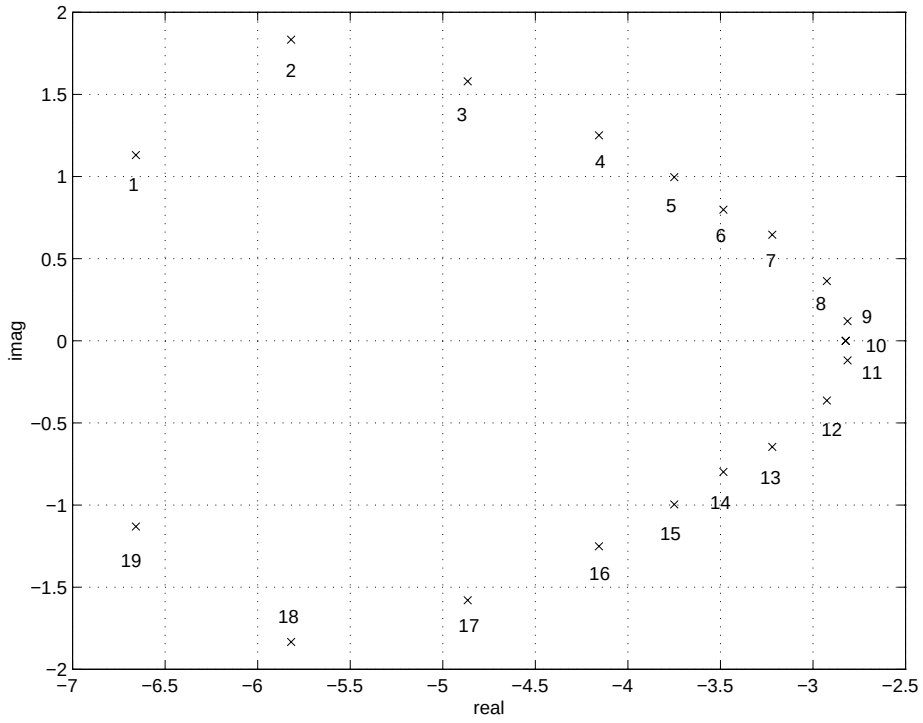

Figure 4-21: Parabolically distributed eigenvalues for Arnoldi reduced order aerodynamic system with 120 aerodynamic states total.

$\omega t = 0$ are shown in Figure 4-22. This figure shows that the vorticity in the eigenmode is confined predominantly to the shock and wake regions, and in particular we can see the region of intense vorticity at the blade trailing edge. More detail of the flow field can be obtained by inspecting the perturbation velocity flow vectors in the wake. These vectors are shown in Figures 4-23 and 4-24 for the flow at $\omega t = 0$ and $\omega t = \frac{\pi}{2}$. At $t = 0$ we can see the area of shed vorticity contained within the partial ellipse near the blade trailing edge where the flow undergoes an abrupt change in direction (recall that the actual flow has a mean velocity superimposed). The path along which this direction change occurs is denoted by the dotted line, and roughly parallels the mean flow velocity direction in that region. In Figure 4-24, the region of shed vorticity is again denoted by an ellipse and can be seen to have convected away from the blade in the direction of the mean flow velocity. The edge of this region has has travelled a distance of approximately $x = 0.65c$ between Figures 4-23 and 4-24.

The reduced frequency of this eigenmode is

$$k = \frac{\omega c}{V} = 2.23,$$

and the corresponding wavelength is

$$L = \frac{V}{f} = \frac{2\pi c}{k} = 2.8c. \tag{4.11}$$

In one quarter of a period ($\omega t = 0$ to $\omega t = \frac{\pi}{2}$) we therefore expect the vorticity to convect a distance $\frac{L}{4} = 0.7c$. This is indeed observed in Figures 4-23 and 4-24.

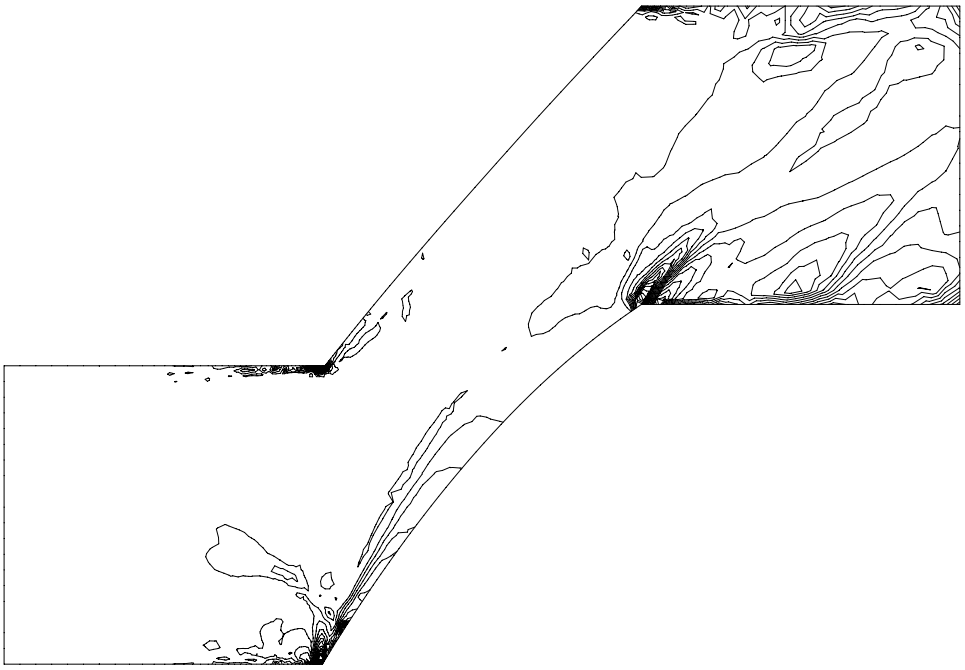

Figure 4-22: Perturbation vorticity contours for a flow solution at $\omega t = 0$ constructed from eigenmode with $\lambda = -5.82 + 1.83i$.

The decaying nature of these eigenmodes can be explained by considering their time evolution. Initially, we have seen that some vorticity is shed from the blade trailing edge. This vorticity will have a particular direction associated to it (which depends on the initial condition exciting the eigenmode). As time proceeds, the shed vorticity convects downstream and induces a velocity at the blade trailing edge. The magnitude of this induced velocity is proportional to the reciprocal of the distance of the first vortex from the trailing edge. This induced velocity will cause another vortex to be shed, with a smaller amplitude than the first vortex, and in the opposite direction. This second vortex then convects downstream and subsequently induces a velocity at the trailing edge, and thus a third vortex. This process continues, with vortices of alternating sign and decaying amplitude being shed a distance of $L/2$ apart (where L is the wavelength defined in (4.11)).

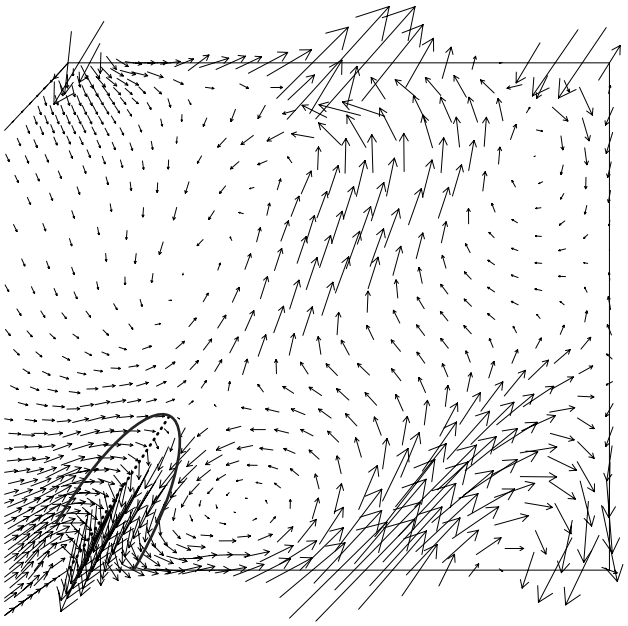

Figure 4-23: Perturbation velocity vectors for a flow solution at $\omega t = 0$ constructed from eigenmode with $\lambda = -5.82 + 1.83i$.

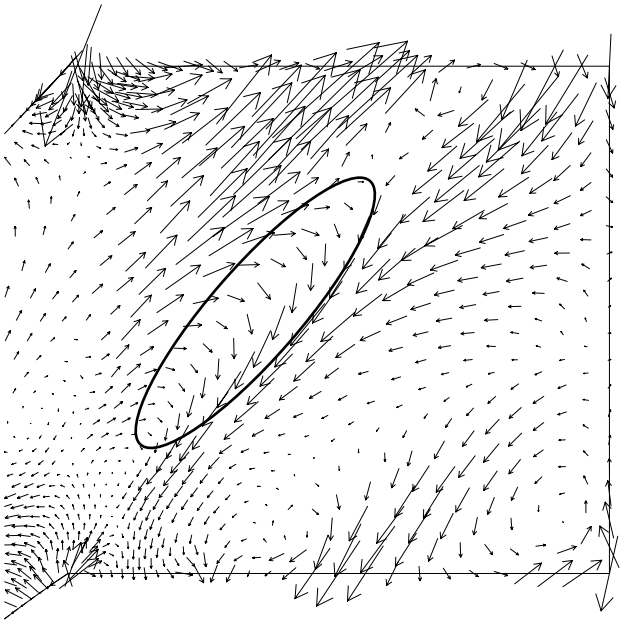

Figure 4-24: Perturbation velocity vectors for a flow solution at $\omega t = \frac{\pi}{2}$ constructed from eigenmode with $\lambda = -5.82 + 1.83i$.

Chapter 5

Mistuning

In typical analyses of bladed discs, the problem is assumed to be tuned, that is all blades are assumed to have identical geometries, mass and stiffness characteristics. In reality, both the manufacturing process and engine wear create a situation where the blades differ slightly from one another. These blade to blade variations are known as mistuning. Even a small amount of mistuning can lead to a large asymmetric forced response [11]. Mode shapes may become spatially localised, causing a single blade to experience deflections much larger than those predicted by a tuned analysis [57] [58]. Mistuning effects must be included in the analysis if the aeroelastic response is to be computed accurately.

The introduction of mistuning typically increases the amplitude of the forced response, so the ideal state would be to have a perfectly tuned bladed disc. However there will always be some degree of *random mistuning* present due to limitations in the manufacturing process or due to engine wear. One can choose some *intentional mistuning* pattern so as to minimise the effect of these random variations. The idea behind robust design is that the worst case behaviour under uncertainty at the intentionally mistuned point is better than the worst case behaviour under uncertainty at the tuned point [49].

Reduced-order models have been developed for structural analysis of mistuned turbomachinery components. Modal information is obtained from large finite element models of the bladed disc and systematically reduced to obtain computationally inexpensive models [34] [33]. Although these reduced-order structural models accurately predict the vibratory response of the blades, the aerodynamic models used in such analyses are extremely inadequate. It has been noted that the mistuned forced response amplitude varies considerably with the degree of aerodynamic coupling [33]. In [30]

blade response to an inlet total pressure distortion was measured in an integrally bladed disk, or blisk. It was found that unsteady aerodynamic effects not modelled in the analysis dominated the response.

Clearly there is a need for higher fidelity aerodynamic models which are suitable for incorporation into the mistuning analysis framework. One option would be to resolve the full Euler or Navier Stokes equations directly, however such models typically have hundreds of thousands of states even in two dimensions, which is not practical for implementation into a mistuned aeroelastic model. Instead, a typical approach is to derive aerodynamic influence coefficients from a CFD model for a specific flow, as described in Chapter 3. Although strictly only valid at a single point in the complex plane, these aerodynamics are assumed to represent the blade response for all flows. It was shown in Chapter 4 that these models do not perform well when the frequency of the eigenvalue moves far from the blade natural frequency, or when a significant amount of aerodynamic damping is present. In a mistuned bladed disk, a high degree of aerodynamic coupling may be observed [30], so that the response contains a range of frequencies and damping, thus reducing the validity of the assumed single-frequency aerodynamics. To accurately capture the system dynamics, a model is required which is valid over a range of frequencies and damping. The aerodynamic reduced-order models developed in this research fit the requirements well. They are developed in the time domain, and consider the entire bladed disc with a reasonable number of states. The aerodynamics are accurately captured over a range of frequencies and the models can be easily coupled to a structural model. Although just structural mistuning will be demonstrated here, models could also be developed for aerodynamic mistuning (variations in, for example, blade shape, thickness, incidence).

5.1 Mistuning Analysis via Symmetry Considerations

Since the reduced-order models have been developed in the time domain for the full rotor, it would be very simple to incorporate structural mistuning into the aeroelastic framework presented in this thesis. For a given pattern of mistuning, the mass and stiffness matrices in the structural equations (2.46) would be evaluated for each blade. The coupled system (4.4) could then be analysed in the same way as for a tuned system.

A framework for mistuning as a design tool has been developed in [50]. Rather than specifying the mistuning pattern, the problem is cast as a constrained optimisation. Given certain goals, it is then possible to find a mistuning pattern which represents an optimal design point. A critical component in performing this analysis accurately is a high-fidelity aerodynamic model. The results

presented in Chapter 4 suggest that a influence coefficient approach will be insufficient, especially in the mistuning context where a high degree of aerodynamic coupling may be present. Typically, the eigenvalues of a mistuned system are expected to exhibit a sufficiently high degree of scatter so that assumed-frequency models do not provide accurate results. The low-order aerodynamic models developed in this thesis have been incorporated into the framework described in [50] and used to provide high-fidelity mistuning results. The results presented in this chapter were generated using the software package MAST (Mistuning Analysis by Symmetry Techniques), which given any linear bladed disc model, computes an approximation of stability and forced response for arbitrary mistuning.

Consider a linearised bladed disc model of the form (2.2), but which allows for mistuning in the blade structural parameters. If the vector $\mathbf{z}$ contains the mistuning for each blade, then (2.2) can be written

$$\dot{\mathbf{s}} = M(\mathbf{z})\mathbf{s} + \mathbf{E}_\ell(\mathbf{z})d_\ell. \tag{5.1}$$

For example, if we consider stiffness mistuning, then the stiffness for blade i is given by

$$k_i = k_0(1 + z_i), \tag{5.2}$$

where k_0 is the nominal or tuned stiffness.

As for the tuned results already presented, stability of the system can be assessed by considering the eigenvalues $\lambda(\mathbf{z})$ of $M(\mathbf{z})$, and describes the change in damping or flutter boundaries with mistuning. Forced response is determined by assuming a sinusoidally time-varying flow

$$\mathbf{s}(t) = \overline{\mathbf{s}}(\mathbf{z})e^{i\omega t} \tag{5.3}$$

and computing

$$\overline{\mathbf{s}}(\mathbf{z}) = [i\omega - M(\mathbf{z})]\,\mathbf{E}_\ell(\mathbf{z}). \tag{5.4}$$

Since forced response essentially determines high cycle fatigue or blade life, it is crucial to understand how mistuning affects the response. For a specific mistuning $\mathbf{z}^*$, it is simple to evaluate stability and forced response, however this approach is not practical for design or analysis since given a set of r different blades, the number of possible mistuning combinations grows as $r!$.

The idea behind the work in [50] is to provide a functional approximation to the mistuned eigenvalues for stability analysis

$$\lambda(\mathbf{z}) \simeq F(\mathbf{z}), \tag{5.5}$$

and to $\overline{\mathbf{s}}(\mathbf{z})$ for forced response

$$\overline{\mathbf{s}}(\mathbf{z}) \simeq G(\mathbf{z}). \tag{5.6}$$

The functions $F(\mathbf{z})$ and $G(\mathbf{z})$ are valid for any (small) mistuning and allow sensitivity studies, robustness analysis and optimisation.

5.2 Reduced-Order Models for Mistuning Analysis

The aerodynamic reduced-order models described in Chapter 3 are written in mixed coordinates. The structural states $\mathbf{u}$ and outputs $\mathbf{y}$ are in blade coordinates, while the aerodynamic states $\mathbf{v}$ are in interblade phase angle coordinates. In order to fit into the mistuning framework developed in [50], all quantities must be expressed in blade coordinates. The transformation from travelling to standing waves is again used [10]. As a result the block diagonal state-space matrix A in (3.38) becomes block circular. For a fixed spatial forcing mode l, the aerodynamic equations (3.38) will now have the form

$$\frac{d}{dt}\begin{bmatrix} \mathbf{v}_1 \\ \mathbf{v}_2 \\ \vdots \\ \mathbf{v}_r \end{bmatrix} = \begin{bmatrix} A_1 & A_2 & \dots & A_r \\ A_r & A_1 & A_2 & \dots \\ & \ddots & & \\ A_2 & A_3 & \dots & A_1 \end{bmatrix}\begin{bmatrix} \mathbf{v}_1 \\ \mathbf{v}_2 \\ \vdots \\ \mathbf{v}_r \end{bmatrix} + \begin{bmatrix} B_1 & B_2 & \dots & B_r \\ B_r & B_1 & B_2 & \dots \\ & \ddots & & \\ B_2 & B_3 & \dots & B_1 \end{bmatrix}\begin{bmatrix} \mathbf{u}_1 \\ \mathbf{u}_2 \\ \vdots \\ \mathbf{u}_r \end{bmatrix}$$

$$+ \quad Re\begin{bmatrix} \bar{\mathbf{e}} \\ p_\ell \bar{\mathbf{e}} \\ \vdots \\ p_\ell^{r-1}\bar{\mathbf{e}} \end{bmatrix} d_\ell(t) \tag{5.7}$$

and

$$\begin{bmatrix} \mathbf{y}_1 \\ \mathbf{y}_2 \\ \vdots \\ \mathbf{y}_r \end{bmatrix} = \begin{bmatrix} C_1 & C_2 & \dots & C_r \\ C_r & C_1 & C_2 & \dots \\ & \ddots & & \\ C_2 & C_3 & \dots & C_1 \end{bmatrix} \begin{bmatrix} \mathbf{v}_1 \\ \mathbf{v}_2 \\ \vdots \\ \mathbf{v}_r \end{bmatrix}, \tag{5.8}$$

where $p_\ell = e^{\frac{2\pi i \ell}{r}}$ and $\mathbf{v}_j$ now contains the aerodynamic states for blade j (as opposed to states for interblade phase angle σ_j).

We now consider the structural system (4.3) describing the plunging motion of each blade which is written for each blade j as

$$\dot{\mathbf{u}}_j = S(z_j)\mathbf{u}_j + Ty_j, \tag{5.9}$$

where the structural matrix S now depends on the mistuning vector. This structural system is coupled with the aerodynamic model (5.7, 5.8) to obtain the dynamics for blade 1,

$$\begin{aligned} \begin{bmatrix} \dot{\mathbf{v}}_1 \\ \dot{\mathbf{u}}_1 \end{bmatrix} &= \begin{bmatrix} A_1 & B_1 \\ TC_1 & S(z_1) \end{bmatrix} \begin{bmatrix} \mathbf{v}_1 \\ \mathbf{u}_1 \end{bmatrix} + \begin{bmatrix} A_2 & B_2 \\ TC_2 & 0 \end{bmatrix} \begin{bmatrix} \mathbf{v}_2 \\ \mathbf{u}_2 \end{bmatrix} + \cdots + \begin{bmatrix} A_r & B_r \\ TC_r & 0 \end{bmatrix} \begin{bmatrix} \mathbf{v}_r \\ \mathbf{u}_r \end{bmatrix} \\ &+ Re \begin{bmatrix} \bar{e} \\ 0 \end{bmatrix} d_\ell. \end{aligned} \tag{5.10}$$

Noting that the dynamics for all other blades follow from symmetry, the complete system can be written

$$\begin{bmatrix} \dot{\mathbf{s}}_1 \\ \dot{\mathbf{s}}_2 \\ \cdot \\ \cdot \\ \cdot \\ \dot{\mathbf{s}}_r \end{bmatrix} = \begin{bmatrix} M_1(z_1) & M_2 & \dots & M_r \\ M_r & M_1(z_2) & M_2 & \dots \\ & \cdot & & \\ & \cdot & & \\ & \cdot & & \\ M_2 & M_3 & \dots & M_1(z_r) \end{bmatrix} \begin{bmatrix} \mathbf{s}_1 \\ \mathbf{s}_2 \\ \cdot \\ \cdot \\ \cdot \\ \mathbf{s}_r \end{bmatrix} + Re \begin{bmatrix} \mathbf{E}_\ell \\ p_\ell \mathbf{E}_\ell \\ \cdot \\ \cdot \\ \cdot \\ p_\ell^{r-1} \mathbf{E}_\ell \end{bmatrix} d_\ell, \tag{5.11}$$

where

$$M_1(z_i) = \begin{bmatrix} A_1 & B_1 \\ TC_1 & S(z_i) \end{bmatrix}, \tag{5.12}$$

$$M_j = \begin{bmatrix} A_j & B_j \\ TC_j & 0 \end{bmatrix} \qquad j = 2, 3, \ldots, r \tag{5.13}$$

and

$$E_\ell = \begin{bmatrix} \overline{e} \\ 0 \end{bmatrix}. \tag{5.14}$$

Equation (5.11) is a special case of equation (5.1) and has the symmetry properties described in [50].

5.3 Mistuning Analysis of Transonic Rotor

The case considered for mistuned analysis is the twenty-blade DFVLR transonic cascade discussed in Chapter 4. The blades were considered to move in unsteady plunging motion, with a tuned natural reduced frequency chosen to be $k = 0.122$. The POD reduced-order model from section 4.4 was used with 80 aerodynamic states. An axial velocity defect was also admitted at the cascade inlet with twenty possible disturbance spatial frequencies included in the model.

5.3.1 Reduced-Order Aerodynamic Model

To demonstrate the effects of mistuning on the rotor response, structural parameters are chosen so as to obtain a very lightly damped system. The case chosen has a blade mass ratio of $\mu = 100$ and a structural damping of $\zeta = -0.0186$. Note that a small negative value of structural damping has been chosen. Clearly this is not physical, however it is used to establish a system which is very lightly damped, and which therefore will exhibit a large sensitivity to mistuning. Such a mode may actually exist in many physical systems, so it is important to determine the possible implications in a mistuning context and to understand their sources.

For consistency with MAST analysis, time is further non-dimensionalised by $t = t'/kM$ so that the tuned natural frequency of the blades is unity. The resulting mistuned version of equation (4.3) is

$$h_j'' + 2(1 + z_j)\zeta h_j' + (1 + z_j)^2 h_j = -\frac{2C_l^j}{\pi\mu k^2}, \tag{5.15}$$

where the mistuning z_j is a percent change in the natural frequency of blade j. The tuned structural eigenvalues for this system are plotted in Figure 5-1. The frequencies fall close to the damped natural frequency of $\sqrt{1-\zeta^2} = 1.00$. The $\ell = 0$ structural mode is barely stable, and the $\ell = 3$ mode is very lightly damped.

We now apply a random mistuning to the structural frequencies of the blades, generated by a normal distribution with a zero average and a 4% variance. The random mistuning pattern considered is shown in Figure 5-2 along with the mistuned and tuned structural eigenvalues. It can be seen that the lightly damped mistuned eigenvalues are to the left of the tuned ones, and so this mistuning pattern stabilises the system, which is true for most mistuning [3]. As noted in [7], the centroid of the structural eigenvalues cannot be altered by a zero-average mistuning. In Figure 5-2 we see that while the lightly damped modes are stabilised, the highly damped eigenvalues shift to the right in order to maintain the position of the centroid. The degree of scattering of the eigenvalues about the centroid is dependent on the amount of coupling between the aerodynamics and the structure. Figure 5-2 also shows that the mistuning reduces the influence of the aerodynamic coupling and moves the eigenvalues towards the centroid, as also discussed in [7].

The system is forced in the ninth nodal diameter mode ($\ell = 9$) which corresponds to the most highly damped tuned eigenvalue in Figure 5-1. The forced response is shown in Figure 5-3 for the tuned case (solid line) and the mistuned case (dotted lines). When the system is tuned, forcing in the ninth spatial mode excites a response in only that mode, and all blades have the same response amplitude, thus the tuned forced response is a single highly damped smooth line. When the system is mistuned, the spatial modes no longer decouple, and forcing in the ninth spatial mode excites all of the structural eigenvalues, including the very lightly damped $\ell = 0$ and $\ell = 3$ modes. Each blade also now exhibits a different response amplitude. Because the lightly-damped modes are now present in the response, we see sharp peaks in the mistuned Bode plot at the frequencies corresponding to the relevant eigenvalues. Here, several blades have a large peak near $\omega = 1$ which corresponds to the very lightly damped $\ell = 0$ mode. We also see a smaller peak for one blade near $\omega = 1.05$ which corresponds to the $\ell = 3$ mode.

Although the random mistuning appears to be beneficial in that it stabilises the system, it creates a situation where the forced response amplitude may rise to unacceptable levels, and also introduces high loading on some individual blades. This might create a problem in practice if a disturbance is known to exist in a particular spatial mode whose eigenvalue is highly damped. A tuned analysis would predict a low forced response amplitude, while in reality small blade to blade variations exist, and the actual response may contain components of the lightly damped modes as demonstrated by Figure 5-3.

The idea behind robust design is to find an intentionally mistuned design point for the blades where the forced response due to random mistuning will be more acceptable than that shown in Figure

5-3. The intentional mistuning is chosen so as to optimise the following objective :

$$\text{Maximise } \Delta\zeta(\mathbf{z}) \text{ subject to } ||\mathbf{z}||_\infty \leq 0.1 \text{ and } \sum z_i = 0. \tag{5.16}$$

This means that we are finding the zero-average mistuning which provides the maximum increase in stability - it drives the least stable eigenvalue pair as far to the left as possible, subject to a constraint on the size of the mistuning. The optimal solution was determined in [50] and is shown in Figure 5-4. The corresponding eigenvalue plot shows that the least stable $\ell = 0$ and $\ell = 3$ eigenvalues have been pushed a significant amount to the left.

We now consider a random mistuning about this intentionally mistuned point. The optimal plus random mistuning pattern is shown in Figure 5-5 along with the corresponding eigenvalues. Once again, we force in the ninth spatial mode and compute the response of the tuned and mistuned systems. The Bode plots shown in Figure 5-6 demonstrate that although the forced response of the mistuned system (dotted lines) is higher than that of the tuned system (solid line), the worst-case amplitude has been significantly reduced compared with that shown in Figure 5-3 for the same random mistuning pattern. The sensitivity of the forced response to random mistuning has been significantly decreased by the introduction of intentional mistuning.

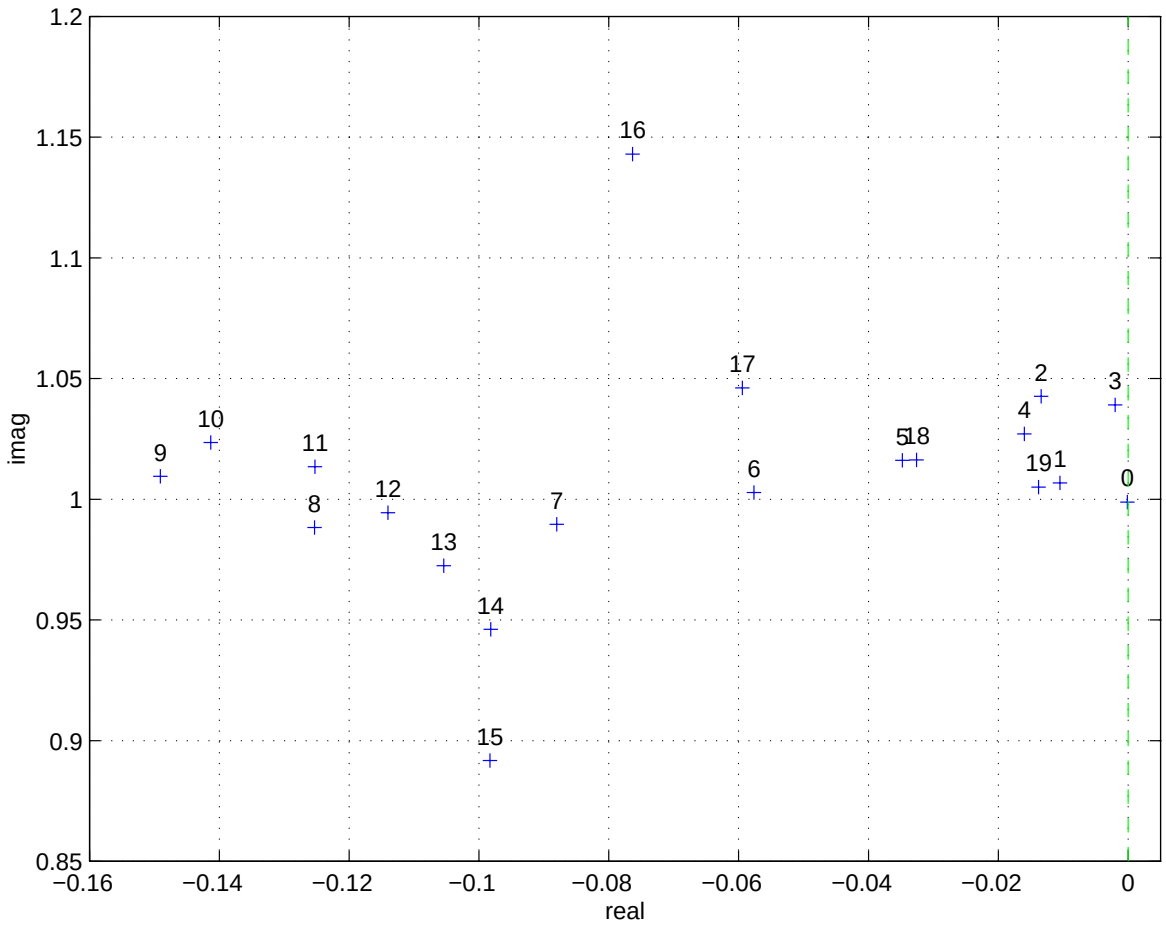

Figure 5-1: Tuned structural eigenvalues for reduced-order model. $k = 0.122$, $\mu = 100$, $\zeta = -0.0186$. Eigenvalues are numbered by their nodal diameter.

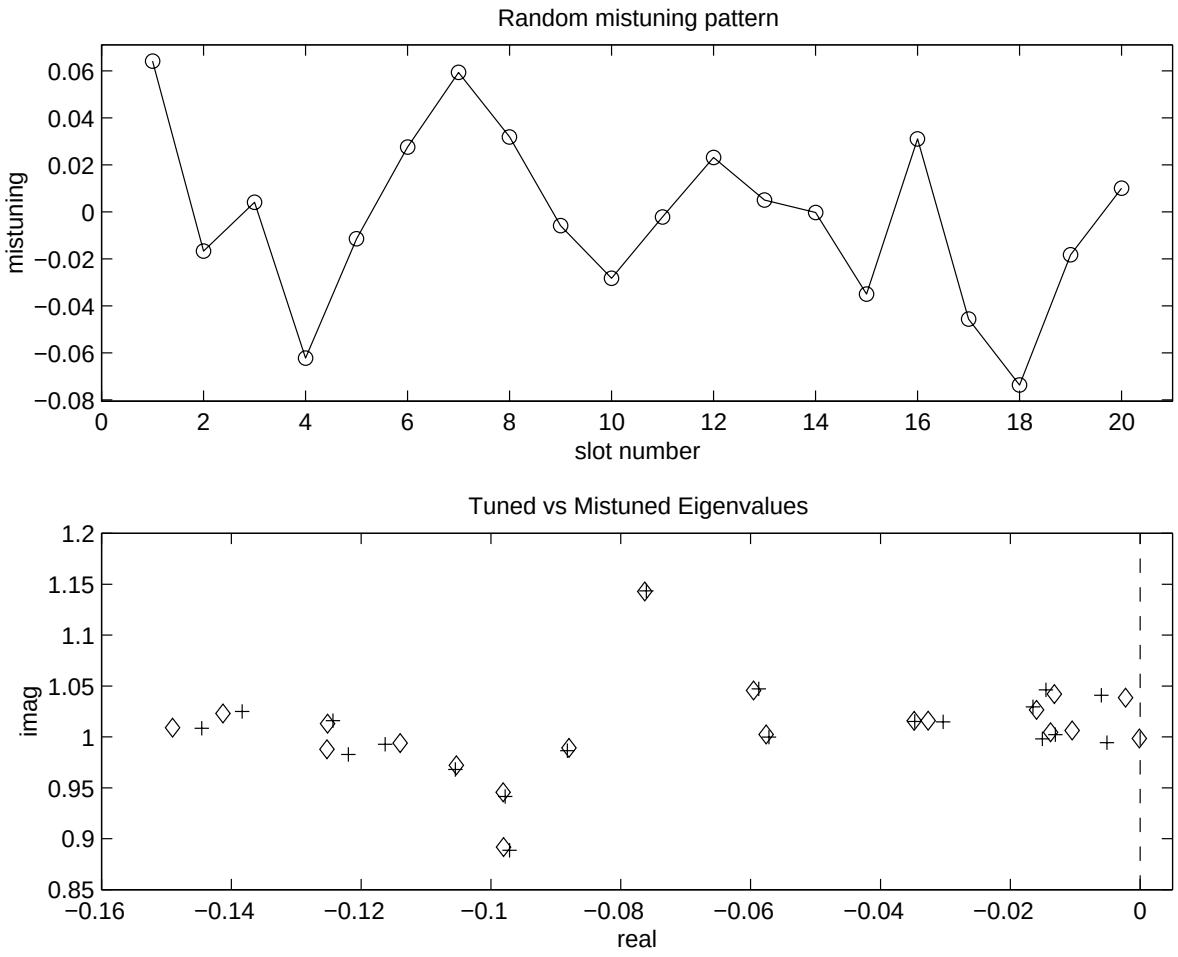

Figure 5-2: Random mistuning of DFVLR rotor. Top: random mistuning pattern. Bottom: tuned eigenvalues (diamonds), mistuned eigenvalues (plus signs).

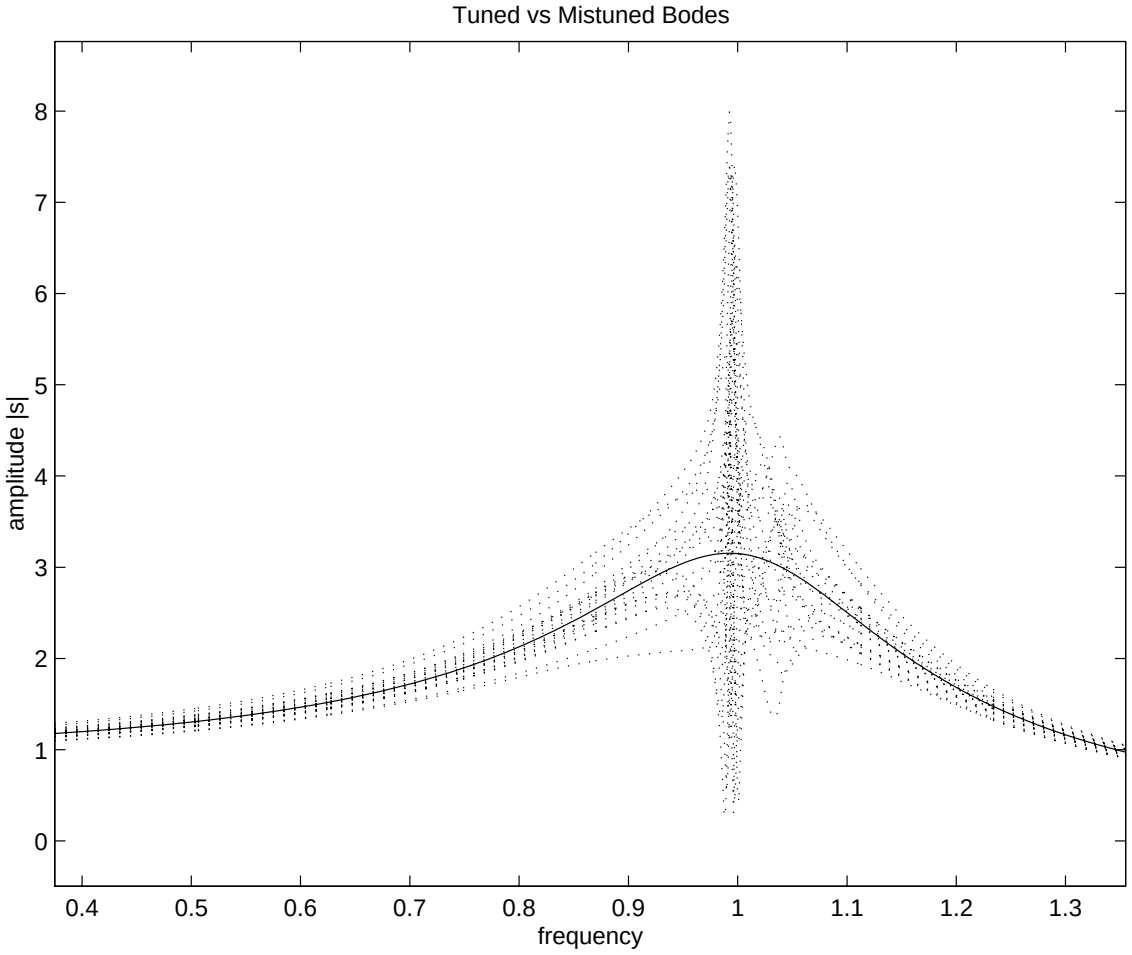

Figure 5-3: Random mistuning of DFVLR rotor. Forced response of tuned system (solid line) and mistuned system (dotted lines) to an inlet disturbance in the ninth spatial mode.

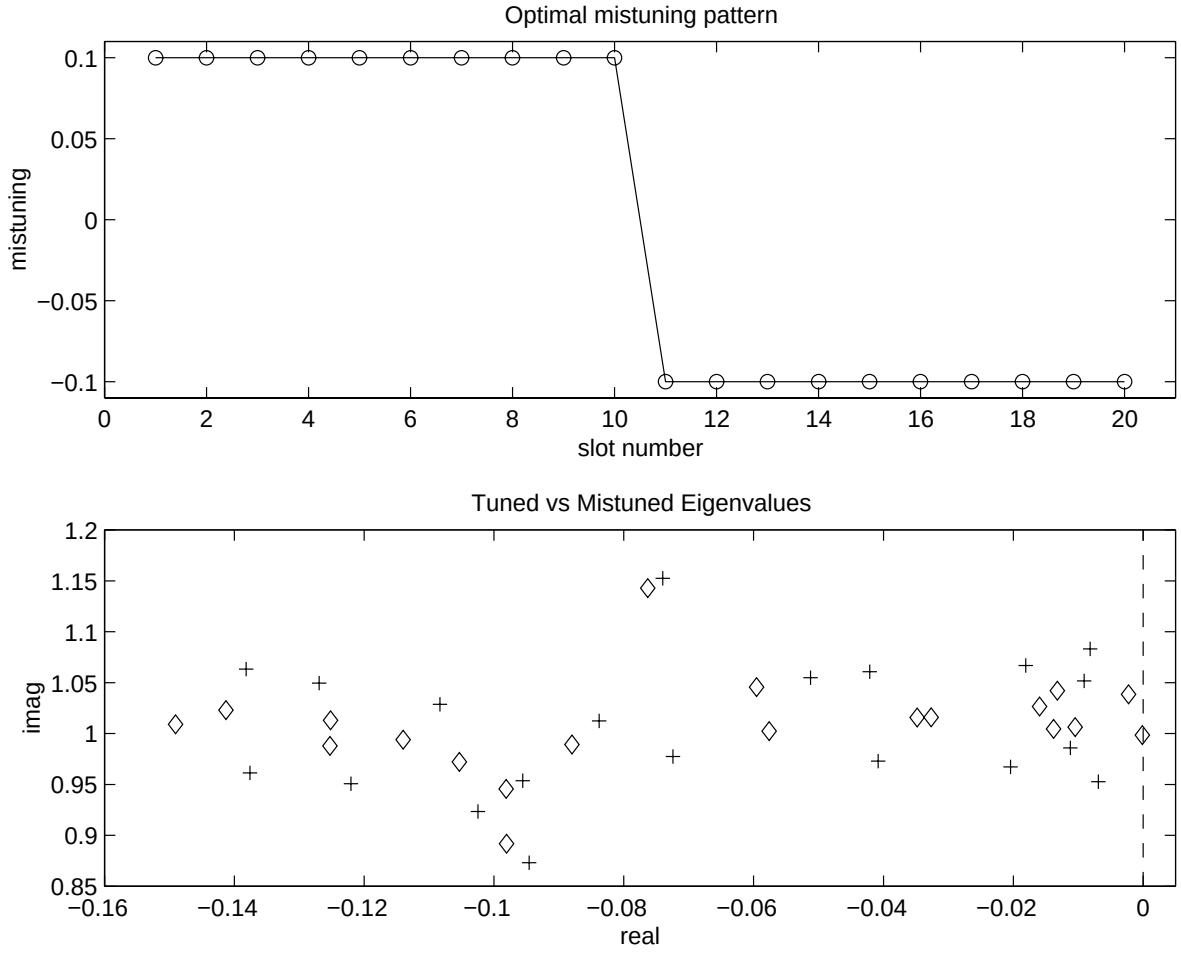

Figure 5-4: Optimal mistuning of DFVLR rotor. Top: optimal mistuning pattern. Bottom: tuned eigenvalues (diamonds), mistuned eigenvalues (plus signs).

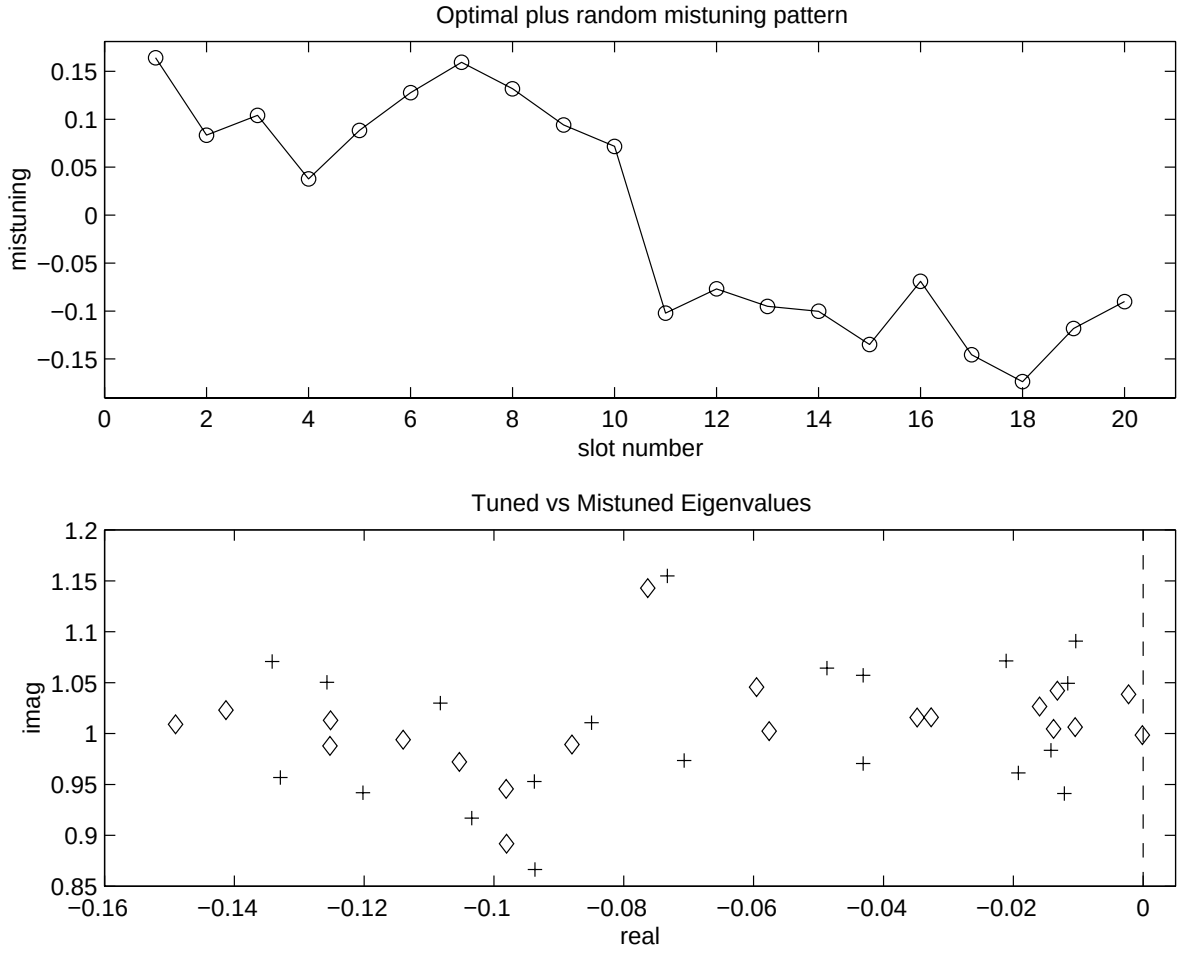

Figure 5-5: Optimal plus random mistuning of DFVLR rotor. Top: optimal plus random mistuning pattern. Bottom: tuned eigenvalues (diamonds), mistuned eigenvalues (plus signs).

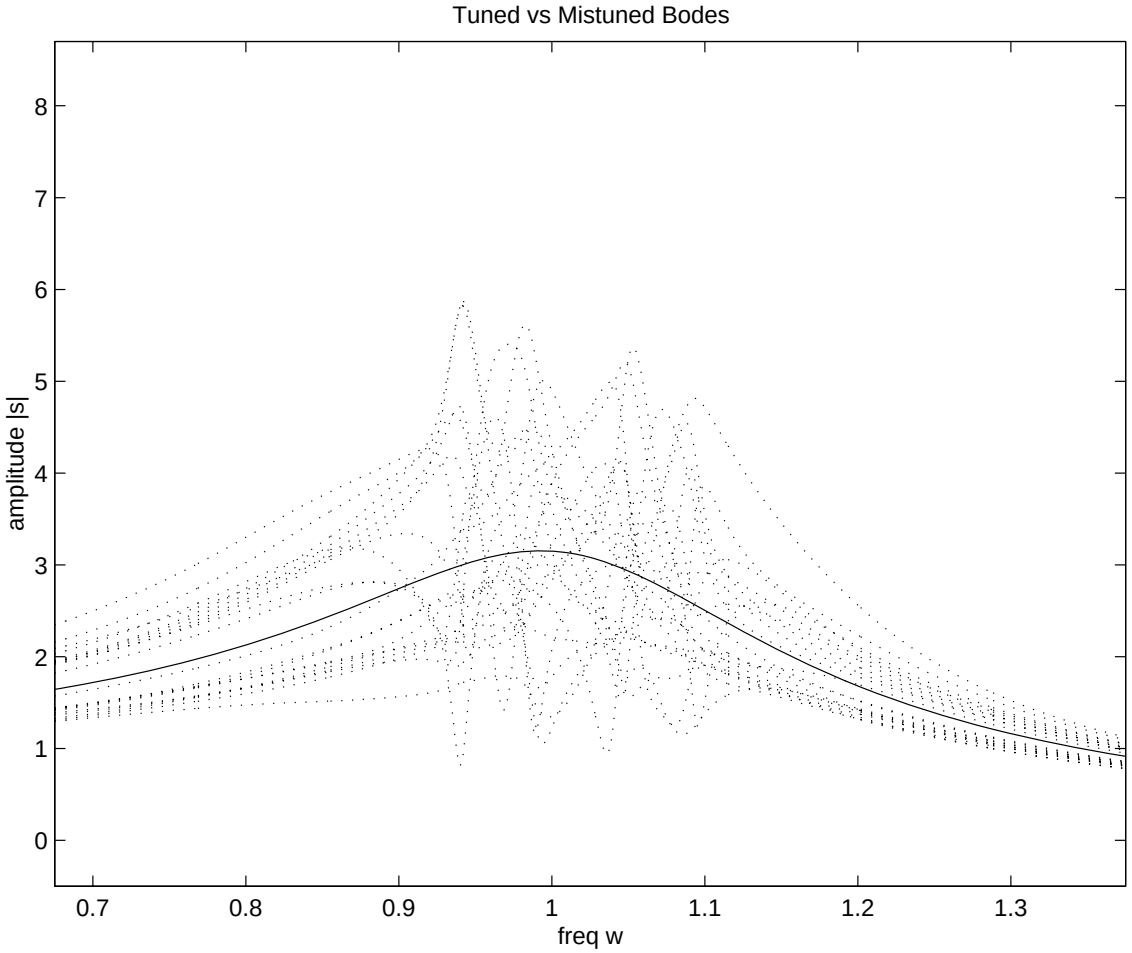

Figure 5-6: Optimal plus random mistuning of DFVLR rotor. Forced response of tuned system (solid line) and mistuned system (dotted lines) to an inlet disturbance in the ninth spatial mode.

5.3.2 Aerodynamic Influence Coefficient Model

In the analysis above, the aerodynamic forces C_l^j in equation (5.15) are represented by the reduced-order model which is valid over a range of frequencies and forcing inputs. Currently most analyses use aerodynamic influence coefficient models such as that described in Chapter 3. The results presented here will show that when mistuning is present, the coupling between the aerodynamics and structural dynamics may be too large for an influence coefficient model to accurately capture the system behaviour.

An identical random mistuning pattern was applied to the influence coefficient model with the same structural parameters described above, and the eigenvalues and forced response of the system were evaluated. Figure 5-7 shows the tuned and mistuned eigenvalues for the reduced-order model and the influence coefficient model. We notice that the mistuning causes the eigenvalues of the influence coefficient model to move much more than those of the reduced-order model. In Figure 5-8 the tuned and mistuned eigenvalues for each model are compared. In the mistuned case, there is a greater error in the influence coefficient eigenvalues. In section 4.4 it was shown that the influence coefficient model does not predict the correct eigenvalue when the frequency shifts significantly from the natural frequency or when a significant amount of aerodynamic damping is present. The influence coefficient model is therefore expected to provide a much worse estimate of the eigenvalues when mistuning is present, since the interblade phase angles no longer decouple. In the tuned system, only the aerodynamics for one interblade phase angle contribute to the placement of each eigenvalue. If a particular mode happens to have an eigenvalue that falls close to the natural frequency with a small amount of damping (corresponding to the case of low aerodynamic coupling), then the influence coefficient model does an excellent job of predicting the eigenvalue position. This can be seen in the top plot of Figure 5-8 where the eigenvalues satisfying the above requirements agree closely with the reduced-order model. However in the mistuned system, the interblade phase angles do not decouple and all dynamics are relevant in computing each eigenvalue. Therefore, if *any* modes exist whose influence coefficients are not representative for the tuned system, the eigenvalues for the mistuned system will be inaccurate and the stability margin of the system will be mispredicted. This can be seen in the lower plot of Figure 5-8 where the difference between the reduced-order model and the influence coefficient model eigenvalues is significant for *all* modes.

In Figure 5-9 the Bode plots are shown for each model in response to an inlet disturbance forcing in the ninth spatial mode. The influence coefficient model in fact does a very good job of predicting the response, even when mistuning is present. The peak tuned response amplitude is slightly higher than that predicted by the reduced-order model, since the tuned influence coefficient eigenvalue is

less highly damped. The mistuned response is computed surprisingly accurately by the influence coefficient model, despite the errors in the mistuned eigenvalue predictions. Inspection of the mistuned eigenvalues in Figure 5-8 shows that the frequencies of the lightly damped $\ell = 0$ and $\ell = 3$ modes is computed accurately, therefore the peaks of the forced response in Figure 5-9 occur at the correct frequency. The damping of these two modes is predicted to be higher than it should, however this may be compensated by the fact that the tuned $\ell = 9$ damping is underpredicted, thus resulting in almost the correct forced response amplitude.

The two modes whose frequencies do move significantly from the natural frequency are $\ell = 15$ and $\ell = 16$. As was shown in section 4.4, when this frequency shift occurs, the influence coefficients do not model the dynamics accurately. This is demonstrated by the difference in position for the uppermost and the lowermost eigenvalue between the reduced-order model and influence coefficient model in both plots in Figure 5-8. When the forced response is calculated for one of these modes, the influence coefficient model no longer predicts the amplitude accurately. Figure 5-10 shows the forced response calculated for the two models for inlet disturbance forcing in the fifteenth spatial mode. We notice first that the tuned forced response predictions differ. This is because the damping of the $\ell = 15$ eigenvalue is incorrectly predicted by the influence coefficient calculation at the blade natural frequency. Figure 5-8 shows that the damping of the eigenvalue is significantly overpredicted by the influence coefficient model, which is consistent with the lower forced response amplitude. When mistuning is introduced into the system, the influence coefficient model does not capture the true amplitudes of the peaks associated with lightly damped modes.

5.4 Mistuning Summary

Random mistuning is an important consideration in the design of bladed disks, since it will always exist to some degree in practice. Although random mistuning in general stabilises the system, it may cause a severe increase in the blade forced response amplitude. The introduction of intentional mistuning can add sufficient damping to the lightly damped modes so that this forced response sensitivity is reduced. The intentionally mistuned bladed disk then represents a robust design.

When a low degree of aerodynamic coupling is present in the system, the structural eigenvalues fall close to the blade natural frequency and an aerodynamic influence coefficient model can accurately capture the dynamics. However if any significant amount of coupling or a large amount of aerodynamic damping exists, which will be true for many bladed disks in practice, these simple models are no longer sufficient. Moreover, when mistuning is present the interblade phase angles do not

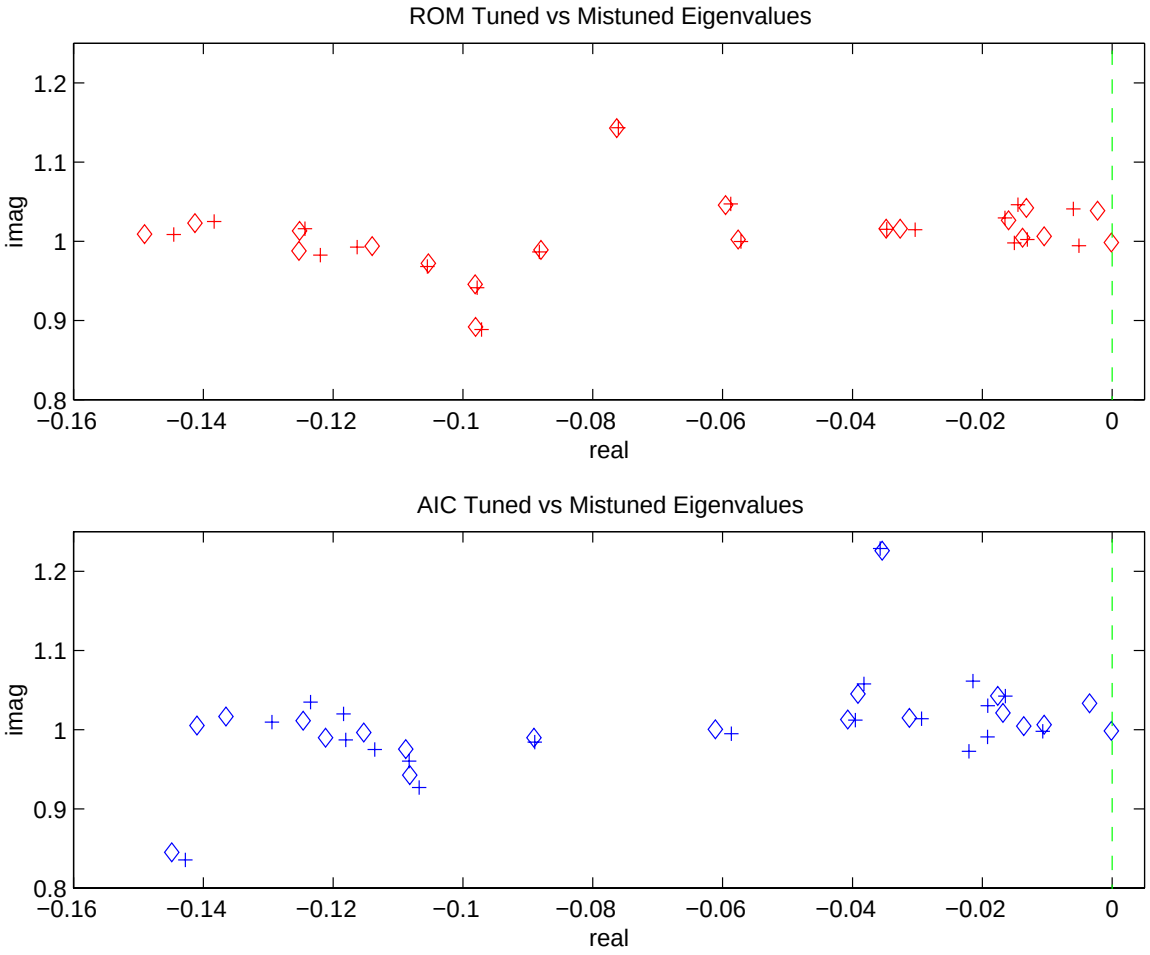

Figure 5-7: Random mistuning of DFVLR transonic rotor. Top: reduced-order model eigenvalues; tuned (diamonds) and mistuned (plus signs). Bottom: influence coefficient model eigenvalues; tuned (diamonds) and mistuned (plus signs).

decouple and the influence coefficient models are even less accurate. In the presence of mistuning, both the forced response and the system stability margin can be predicted inaccurately. For the results presented in this chapter, a relatively low amount of aerodynamic coupling exists, however the influence coefficient model is still seen to fail in some cases. In practice, experimental results have shown that a large degree of coupling exists for mistuned disks, and the single frequency models are inadequate. The reduced-order models developed in this research have been shown to fit very well into the mistuning framework. They can be easily incorporated into the mistuned aeroelastic system, and capture the system dynamics well over a range of frequencies. The reduced-order models could be further developed to include aerodynamic mistuning.

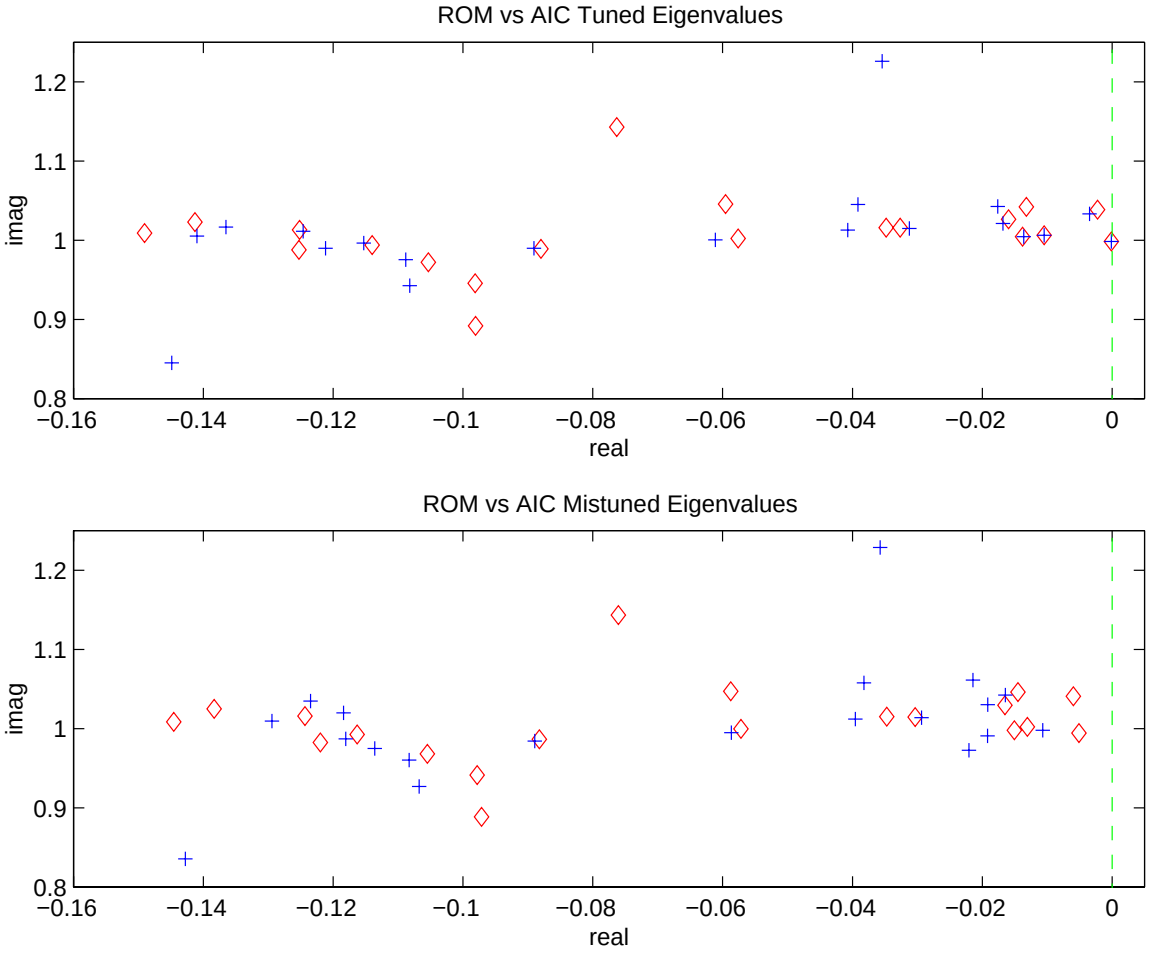

Figure 5-8: Random mistuning of DFVLR transonic rotor. Top: tuned eigenvalues; reduced-order model (diamonds) and influence coefficient model (plus signs). Bottom: mistuned eigenvalues; reduced-order model (diamonds) and influence coefficient model (plus signs).

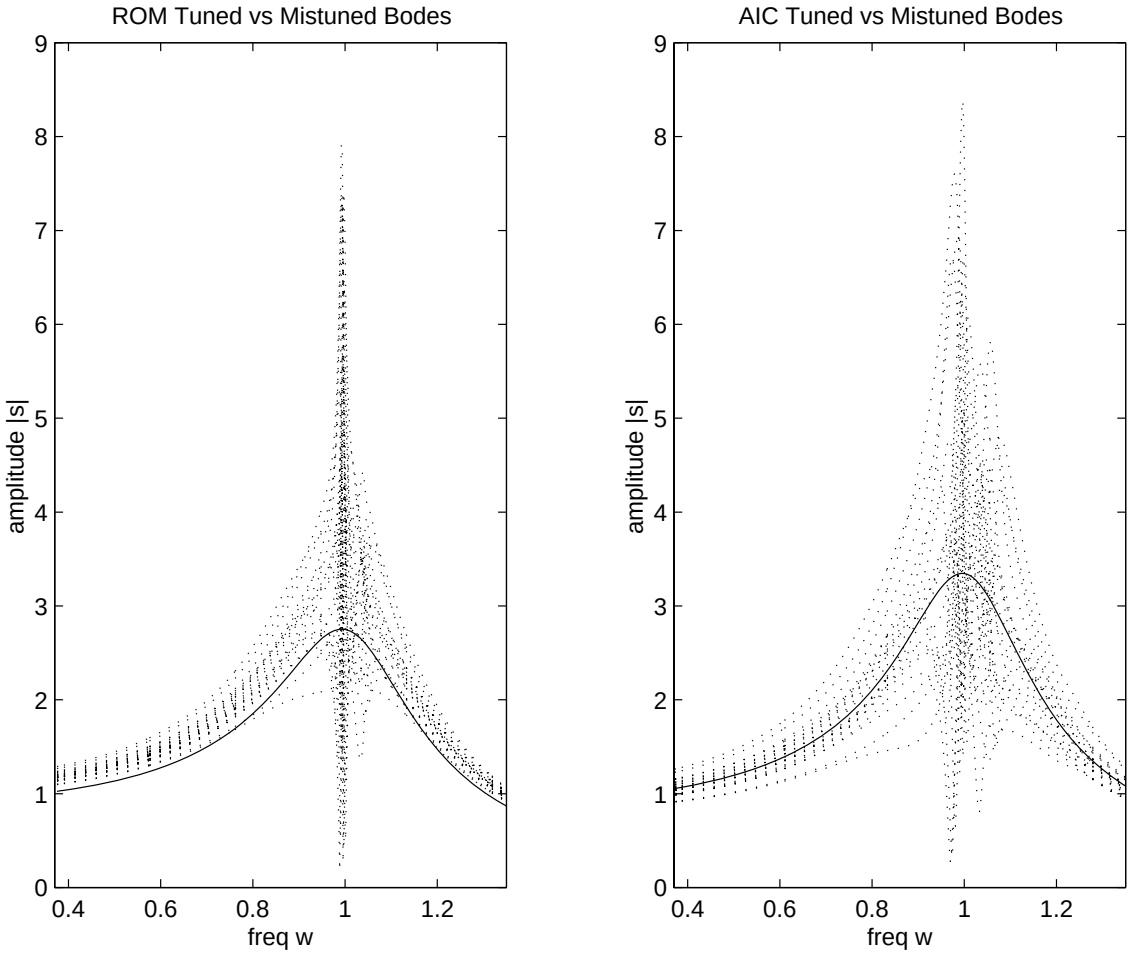

Figure 5-9: Random mistuning of DFVLR transonic rotor. Forced response to inlet disturbance in the $\ell = 9$ mode for reduced-order model (left) and influence coefficient model (right). Solid line denotes the tuned response, dotted lines are the mistuned response.

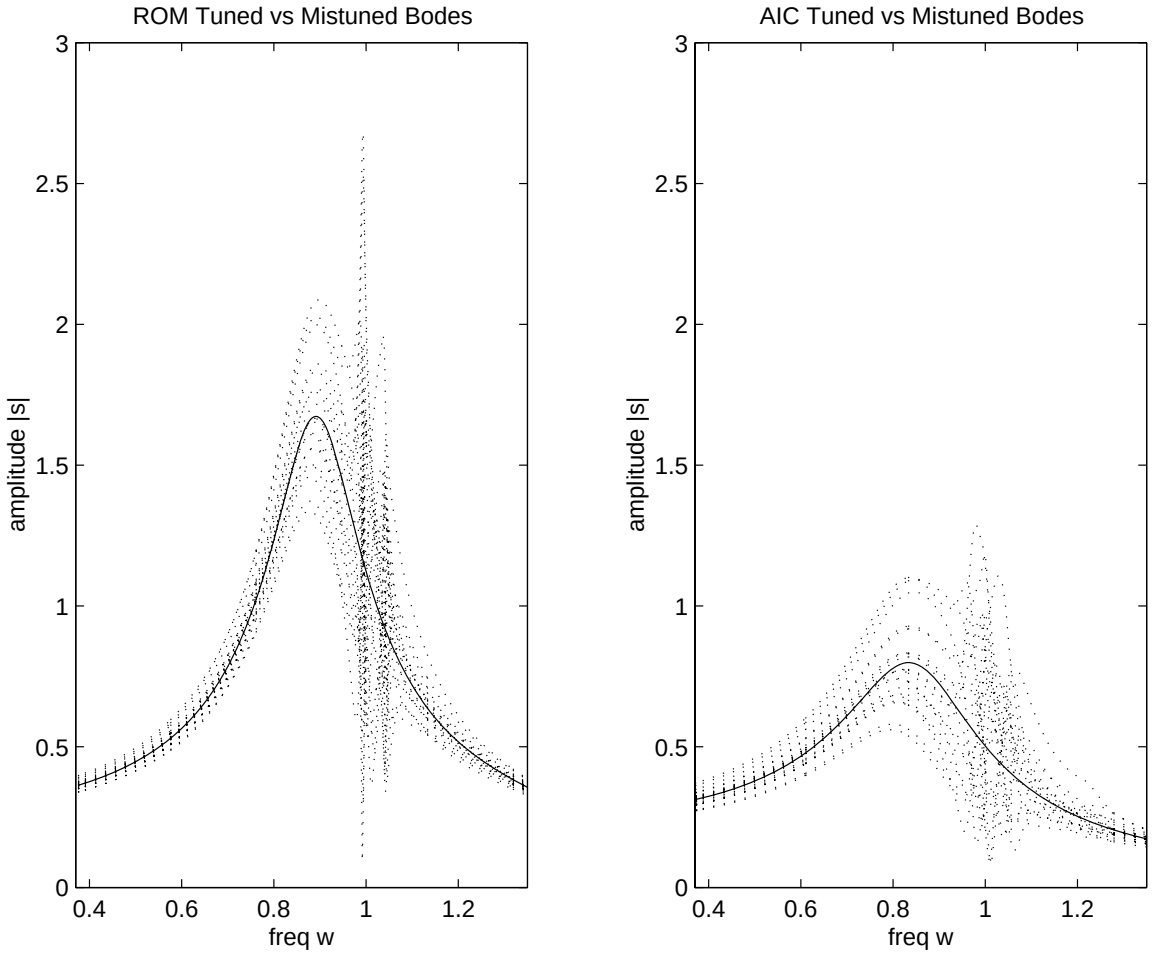

Figure 5-10: Random mistuning of DFVLR transonic rotor. Forced response to inlet disturbance in the $\ell = 15$ mode for reduced-order model (left) and influence coefficient model (right). Solid line denotes the tuned response, dotted lines are the mistuned response.

Chapter 6

Multiple Blade Row Analysis

We consider two types of blade row. In addition to the rotors described in the previous analyses, we consider stators, or stationary blade rows, in which the blades are assumed to be rigid. The size and nature of the reduced order models developed here lend themselves naturally to analysis of several blade rows. State-space systems can be derived for each blade row, with sizes on the order of ten states per blade passage. Because the models are developed in the time-domain, it is then straightforward to couple these systems and capture inter-blade row effects. Even with several blade rows included in the analysis, the size of the model is small enough that unsteady simulations and control analyses can be performed.

6.1 Blade Row Coupling

Adjacent blade rows will be coupled via the characteristic perturbation waves travelling between them. Assuming subsonic axial conditions, at a passage inlet there are incoming waves in the following three characteristic quantities

$$\begin{aligned} c_1 &= p' - \overline{c}^2 \rho' \\ c_2 &= \overline{\rho}\ \overline{c}\ u'_t \\ c_3 &= p' - \overline{\rho}\ \overline{c}\ u'_n, \end{aligned} \tag{6.1}$$

which describe respectively entropy, vorticity and downstream running pressure waves. At the passage exit, we have an upstream running pressure wave given by

$$c_3 \quad = \quad p' - \overline{\rho}\ \overline{c}\ u'_n. \tag{6.2}$$

Note that $c_4 = p' + \overline{\rho}\ \overline{c}\ u'_n$ at the rotor inlet is equivalent to c_3 at the stator exit since the characteristics are defined in terms of normal vectors which always point out of the computational domain. Here the coupling between a rotor and an upstream stator will be described. Additional blade rows could be added in an analogous way. Consider the reduced-order model for the rotor which has aerodynamic states $\mathbf{v}_r$ and can be written

$$\dot{\mathbf{v}}_r = A_r \mathbf{v}_r + B_r \mathbf{u}_r + E_1 \mathbf{w}_1 + E_2 \mathbf{w}_2 + E_3 \mathbf{w}_3, \tag{6.3}$$

where $\mathbf{w}_1$, $\mathbf{w}_2$, and $\mathbf{w}_3$ are vectors containing the incoming characteristic perturbation quantities c_1, c_2 and c_3 respectively at each grid point in the rotor inlet plane. These quantities are matched to the flow at the stator exit, and can be written in terms of the stator aerodynamic state variables $\mathbf{v}_s$

$$\mathbf{w}_1(t) = C_{rs}(t) C_{s_1} \mathbf{v}_s(t), \qquad \mathbf{w}_2(t) = C_{rs}(t) C_{s_2} \mathbf{v}_s(t), \qquad \mathbf{w}_3(t) = C_{rs}(t) C_{s_3} \mathbf{v}_s(t). \tag{6.4}$$

Here C_{s_j} are constant matrices depending on the mean flow which relate the state variables $\mathbf{v}_s$ to the values of the characteristics at each point in the stator exit plane. For example, for a node k at the stator exit, the kth row of C_{s_1} contains the component of each basis vector corresponding to the value of c_1 at k. C_{s_2} and C_{s_1} are determined similarly, using the components of the basis vectors corresponding to c_2 and c_3 at the appropriate points. C_{rs} is an interpolation matrix which varies with time, and determines the flow at the rotor inlet at a given instantaneous configuration of the stator/rotor combination. For example, consider the instantaneous configuration shown in Figure 6-1. The value of c_1 at a point j in the rotor inlet plane would be contained in the jth component of $\mathbf{w}_1$ and could be written as a linear combination of the values of c_1 at the points k and $k-1$ in the stator exit plane, that is

$$c_1^j = \overline{\alpha} c_1^k + (1 - \overline{\alpha}) c_1^{k-1}, \tag{6.5}$$

where the constant $\overline{\alpha}$ is determined from the ratio of the lengths $l_{j,k}$ and $l_{j,k-1}$. The jth row of C_{rs} is therefore all zeroes except for a value of $\overline{\alpha}$ in the kth column and a value of $1 - \overline{\alpha}$ in the $(k-1)$th column.

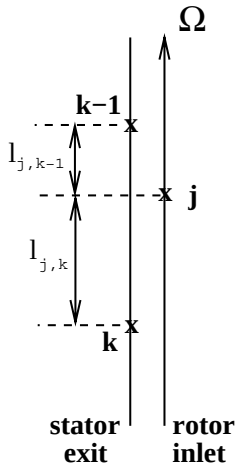

Figure 6-1: Instantaneous configuration of rotor and stator. Grid point j is in the rotor inlet plane, while points k and $k-1$ are in the stator exit plane.

Likewise, the incoming characteristic wave at the stator exit can be written in terms of the rotor aerodynamic state variables as follows.

$$\mathbf{w}_4(t) \quad = \quad C_{sr}(t) C_{r_4} \mathbf{v}_r(t), \tag{6.6}$$

where the matrices C_{sr} and C_{r_4} are defined in an analogous manner to those described above for the rotor inlet, and the corresponding state-space system for the stator is

$$\dot{\mathbf{v}}_s = A_s \mathbf{v}_s + + E_4 \mathbf{w}_4. \tag{6.7}$$

The stator is assumed to be rigid, so there is no forcing vector $\mathbf{u}$ as there is for the rotor.

The systems (6.3) and (6.7) can be combined to form a large set of equations which can be time-marched simultaneously

$$\begin{bmatrix} \dot{\mathbf{v}}_r \\ \dot{\mathbf{v}}_s \end{bmatrix} = \begin{bmatrix} A_r & \sum_{j=1}^{3} E_j C_{rs} C_{s_j} \\ E_4 C_{sr} C_{r_4} & A_s \end{bmatrix} \begin{bmatrix} \mathbf{v}_r \\ \mathbf{v}_s \end{bmatrix} + \begin{bmatrix} B_r \mathbf{u}_r \\ 0 \end{bmatrix}. \tag{6.8}$$

We note that since the matrix in (6.8) depends on the instantaneous stator/rotor configuration, it varies with time. Moreover, the coefficients of the matrix are periodic with the rotor rotation frequency.

6.2 GE Low Speed Compressor

The multi-stage compressor analysed here is the GE low-speed research compressor which has four repeating stages [51]. In the actual rig, each rotor has 54 blades and each stator has 74 vanes. In the analysis presented here we consider a simpler case with sixteen and twenty blades in the rotor and stator respectively. The geometry of the stage is shown in Figure 6-2 for a quarter of the full wheel (five stator blades and four rotor blades). The axial spacing between the stator and rotor is 47.5% of the rotor axial chord. The third stage of the compressor will be considered for analysis here. The velocity triangles at the inlet and exits of each blade row are shown in Figure 6-3. Mach numbers for the rotor are in the relative reference frame, while for the stator they are absolute.

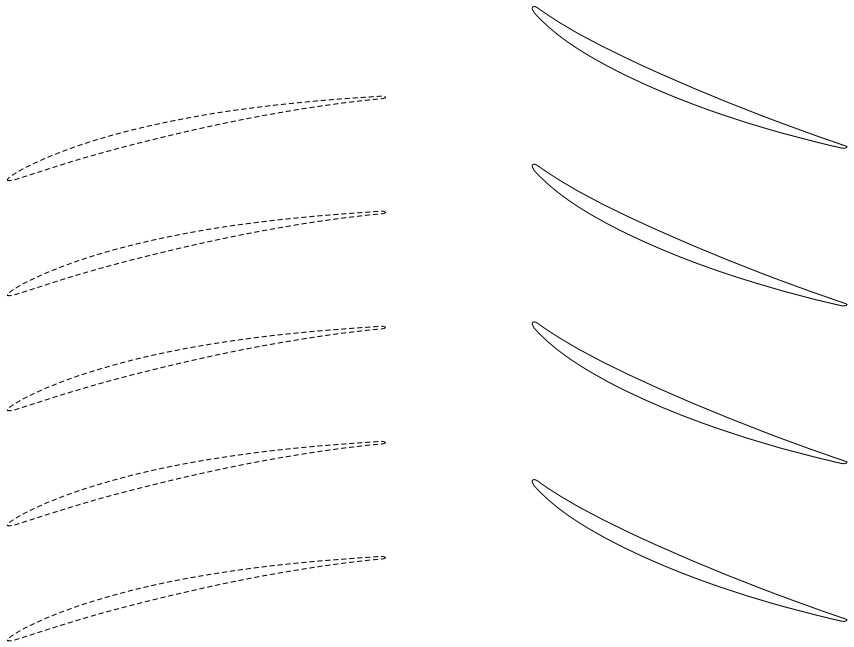

Figure 6-2: Stator and rotor geometry for a single stage of the GE low-speed compressor.

6.2.1 Steady-State Solutions

The steady-state flow for the rotor has an inlet Mach number of 0.165 at a flow angle of 59.3°. The computed steady-state Mach contours are shown in Figure 6-4. Figure 6-5 shows the Mach contours for the steady-state flow through the stator, which has an inlet Mach number of 0.123 at an angle of 47.3°.

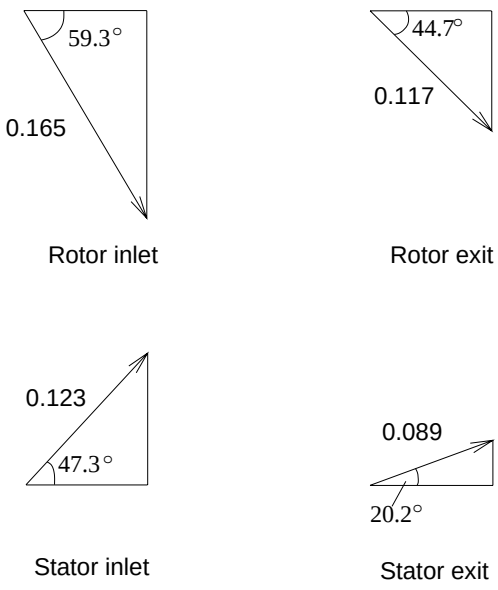

Figure 6-3: Velocity triangles for third stage of GE low-speed compressor. Relative Mach numbers for rotor, absolute Mach numbers for stator.

6.2.2 Unsteady Analysis

The low-speed compressor was analysed in unsteady plunging motion. Reduced-order models were constructed for the rotor and the stator using the Arnoldi method described in Chapter 3. In all cases the Arnoldi vectors were derived about $s = 0$. For the rotor, there are five relevant input vectors; namely blade plunge displacement, blade plunge velocity and perturbations in the three incoming inlet characteristic waves. For the stator there is just one input, which is the perturbation in the incoming pressure wave. For the sixteen blade rotor, a total of 248 aerodynamic modes were chosen (eight modes for $\sigma = 0$ and sixteen modes for all other interblade phase angles). For the stator, which has twenty blades, four modes for the zero interblade phase angle and six modes for all others were taken, for a total of 118 stator states. The coupled stator/rotor system therefore has 366 aerodynamic states.

We compare the coupled system (6.8) with the system for the rotor alone (6.3). For previous cases, a single blade row was analysed by considering forced response (time history of forces) and stability (eigenvalues of the system). The crucial difference between the coupled system (6.8) and the single blade row state-space systems analysed previously is that the system matrix no longer has constant coefficients. For the coupled system, the interpolation matrices C_{rs} and C_{sr} vary with time and are in fact periodic with the rotor rotation frequency. Rather than being fixed, each eigenvalue

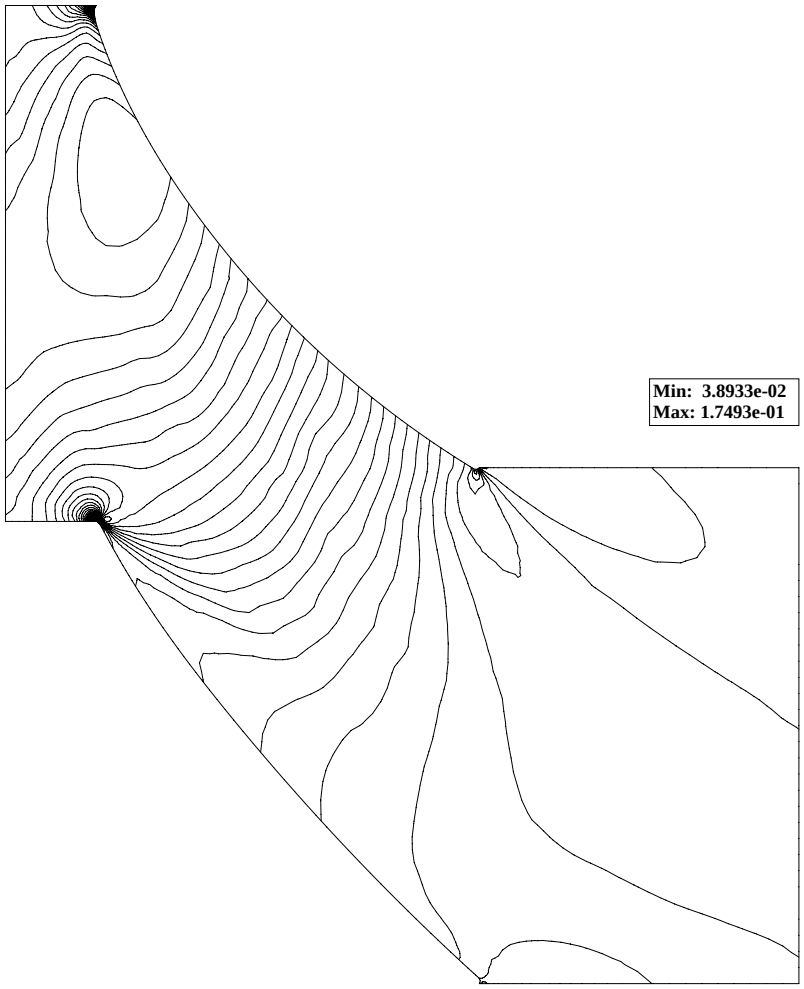

Figure 6-4: Mach contours for GE low-speed compressor, third stage rotor. $M = 0.165$, $\alpha = 59.3°$.

of the matrix now forms a locus in the complex plane. Previously, an eigenvalue in the right half plane indicated an unstable system. In the time-varying system, it is possible for an eigenvalue to cross into the right half plane for part of the cycle (resulting in local growth), but for the overall system to be stable if the time spent in the right half plane is sufficiently short. The stability of the stator/rotor system is best determined by performing time simulations.

The aerodynamic eigenvalues of the individual rotor and stator state space systems are plotted in Figure 6-6. The eigenvalues of the coupled stator/rotor system at a particular time instant are also plotted for comparison. A smaller region of this plot near the origin is shown in Figure 6-7. From Figures 6-6 and 6-7, we can see that coupling the stator has a significant impact on the aerodynamics. Although the eigenvalues of the coupled system will vary with time, the magnitude of these variations is not expected to be very large compared with the differences between the coupled

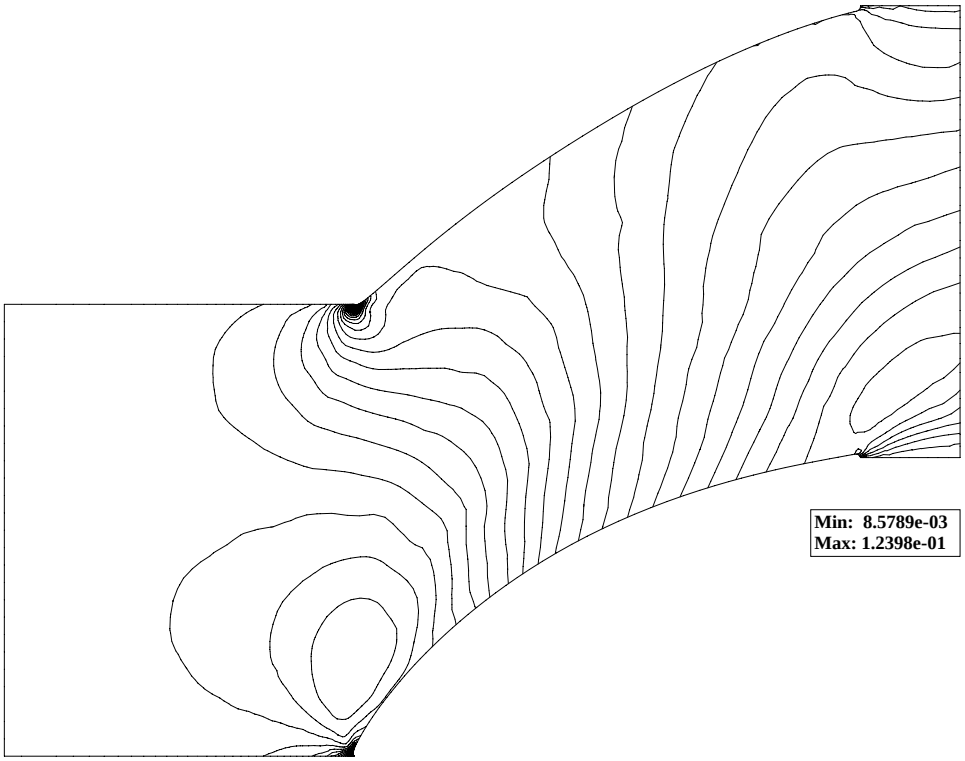

Figure 6-5: Mach contours for GE low-speed compressor, third stage stator. $M = 0.123$, $\alpha = 47.3°$.

and isolated blade row spectra.

The aerodynamic system was forced with a pulse input in plunge at one blade and all other blades fixed. This motion excites all possible interblade phase angles in the rotor. The resulting lift forces on each of the rotor blades were calculated using both the rotor-alone reduced-order model and the coupled stator/rotor system, and are plotted in Figure 6-8. To give an indication of the time scales on these plots, we note that the non-dimensional period for one rotor revolution is $T_r = 316$. The dotted line denotes the (specified) position of the rotor blade, the solid line is the force calculated using the coupled model, and the dashed line is the force evaluated for the rotor alone. From Figure 6-8 it appears that there is a small difference between the two force calculations. In Figure 6-9 the response for just the first blade is plotted, which shows that the stator does have a fairly significant effect. The magnitude of the peak response is roughly the same, but for the rotor-alone calculation, the force on the blade dies away smoothly as the pulse passes. With the stator included in the analysis, even after the pulse has passed through the system, we see oscillations due to the unsteady effect of the passing blades. These oscillations can be seen to have a period of approximately $T = 15$, which corresponds to one twentieth of the rotor revolution period.

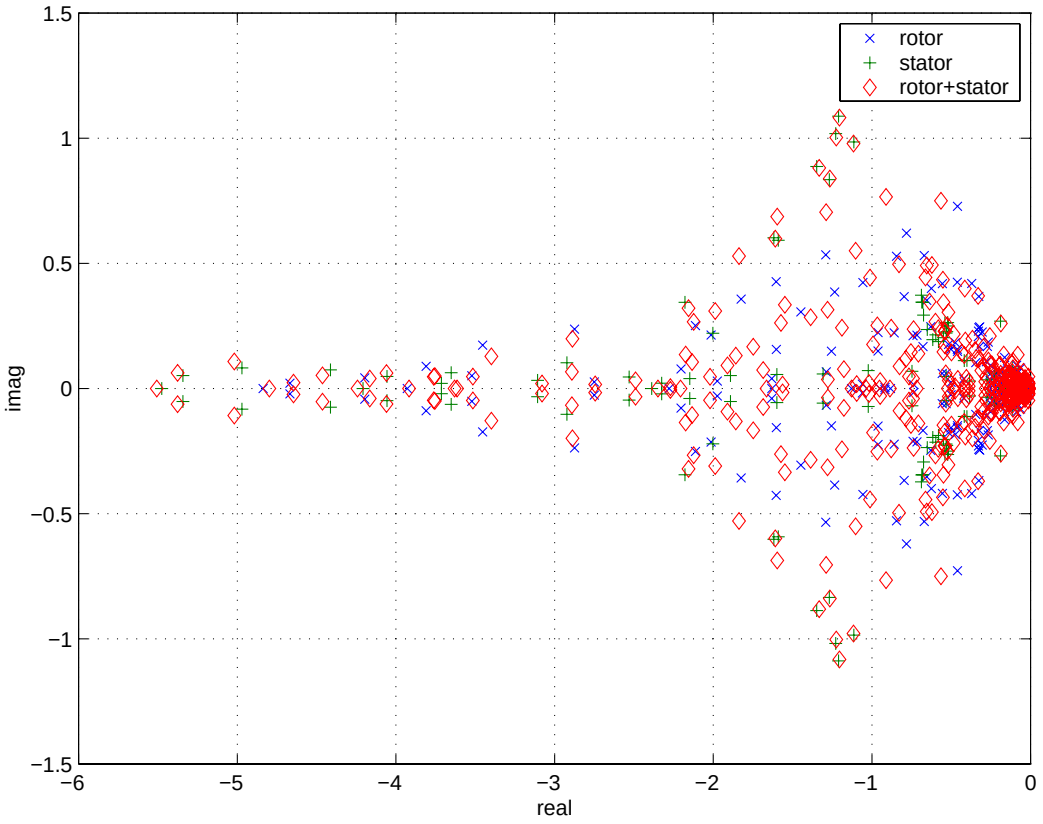

Figure 6-6: Aerodynamic eigenvalues for reduced-order models : rotor alone (crosses, 248 states), stator alone (plus signs, 118 states) and coupled system (diamonds, 366 states).

Next, a structural model for the rotor blades was coupled to the system. This model has the same form as (4.3). Two structural modes per blade are added with eigenvalues near $-\zeta kM \pm ikM$, where M is the Mach number at the rotor inlet (in this case $M = 0.165$). In Figure 6-10, a plot of these structural eigenvalues is shown for the rotor-alone model with structural parameters $\mu = 100$, $k = 0.5$ and $\zeta = 0.13$. For these parameters, the blade-alone eigenvalues would be at $-0.011 \pm 0.0825i$. For the stator/rotor system, when the structural model (4.3) is coupled in, the equations take the form

$$\begin{bmatrix} \dot{\mathbf{v}}_r \\ \dot{\mathbf{v}}_s \\ \dot{\mathbf{u}}_r \end{bmatrix} = \begin{bmatrix} A_r & \sum_{j=1}^{3} E_j C_{rs} C_{s_j} & B_r \\ E_4 C_{sr} C_{r_4} & A_s & 0 \\ TC & 0 & S \end{bmatrix} \begin{bmatrix} \mathbf{v}_r \\ \mathbf{v}_s \\ \mathbf{u}_r \end{bmatrix}, \tag{6.9}$$

where the matrix C defines the forces on the rotor blades, $\mathbf{y}_r = C\mathbf{x}_r$. The matrix in (6.9) was evaluated at a series of time instants for the structural parameters described above, and the eigenvalues were determined. The loci of the structural eigenvalues are plotted as dots in Figure 6-10. The variations within the loci are small, however for some modes we notice a significant difference between the position of the locus and the rotor-alone structural eigenvalue. For almost all modes,

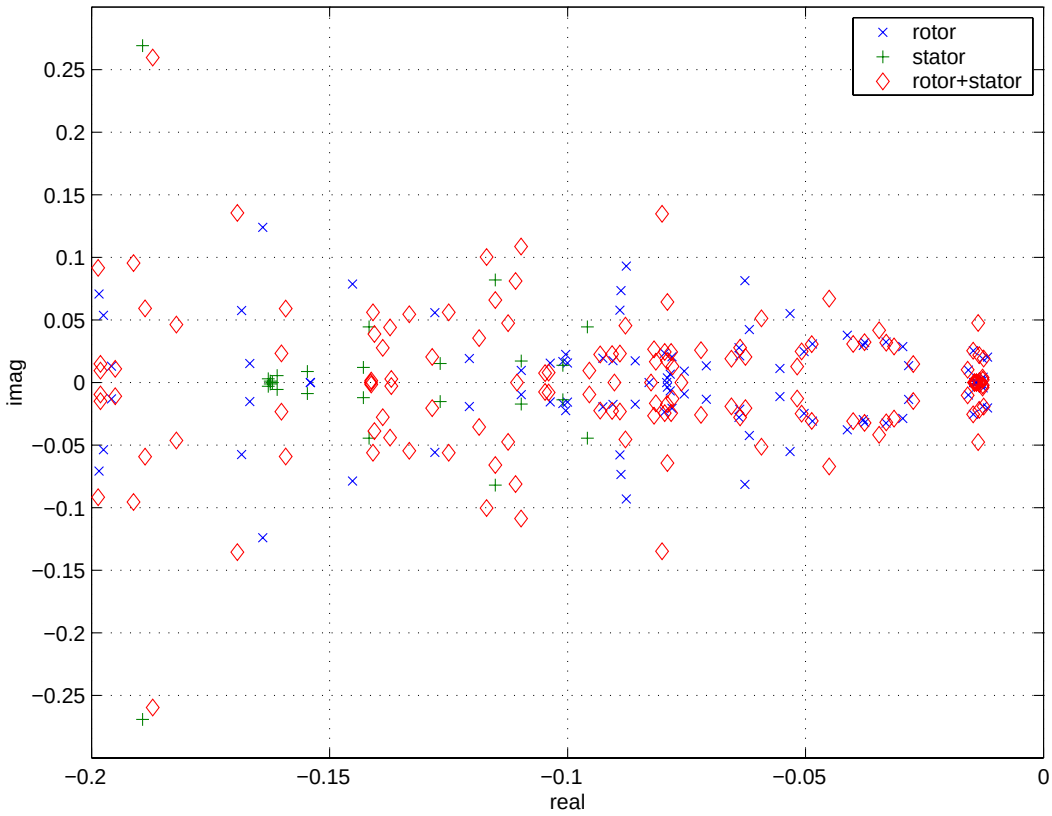

Figure 6-7: Zoom of aerodynamic eigenvalues for rotor and stator reduced-order models.

the addition of the stator model is destabilising, which suggests that an isolated blade row analysis could significantly underpredict the response. The structural eigenvalue corresponding to $\ell = 15$ ($\sigma = 337.5°$) is barely stable for the rotor-alone system, however for the coupled system its locus lies entirely in the right half plane. We therefore have the serious case that the rotor-alone predicts a barely stable system, but with the effect of the stator included the system is unstable. The locus for the unstable eigenvalue is plotted on 6-11.

A time simulation of the coupled system was performed where an initial plunge displacement was applied to the first blade. The resulting motion and force were calculated for each blade and are plotted in Figures 6-12 and 6-13 respectively, along with the calculations for the rotor-alone aeroelastic system. We now see some significant variations between the force calculations. For all blades, the rotor-alone model predicts a smaller response than the coupled analysis. This is consistent with the destabilising effect of the stator on the eigenvalues. In some cases, the rotor-alone model predicts that the amplitude of the oscillations is barely decaying, while the coupled model predicts a relatively rapid growth rate, due to the destabilised $\ell = 15$ eigenvalue. The response for one of the blades is plotted in Figure 6-14 and clearly shows the rapid increase in displacement amplitude. In

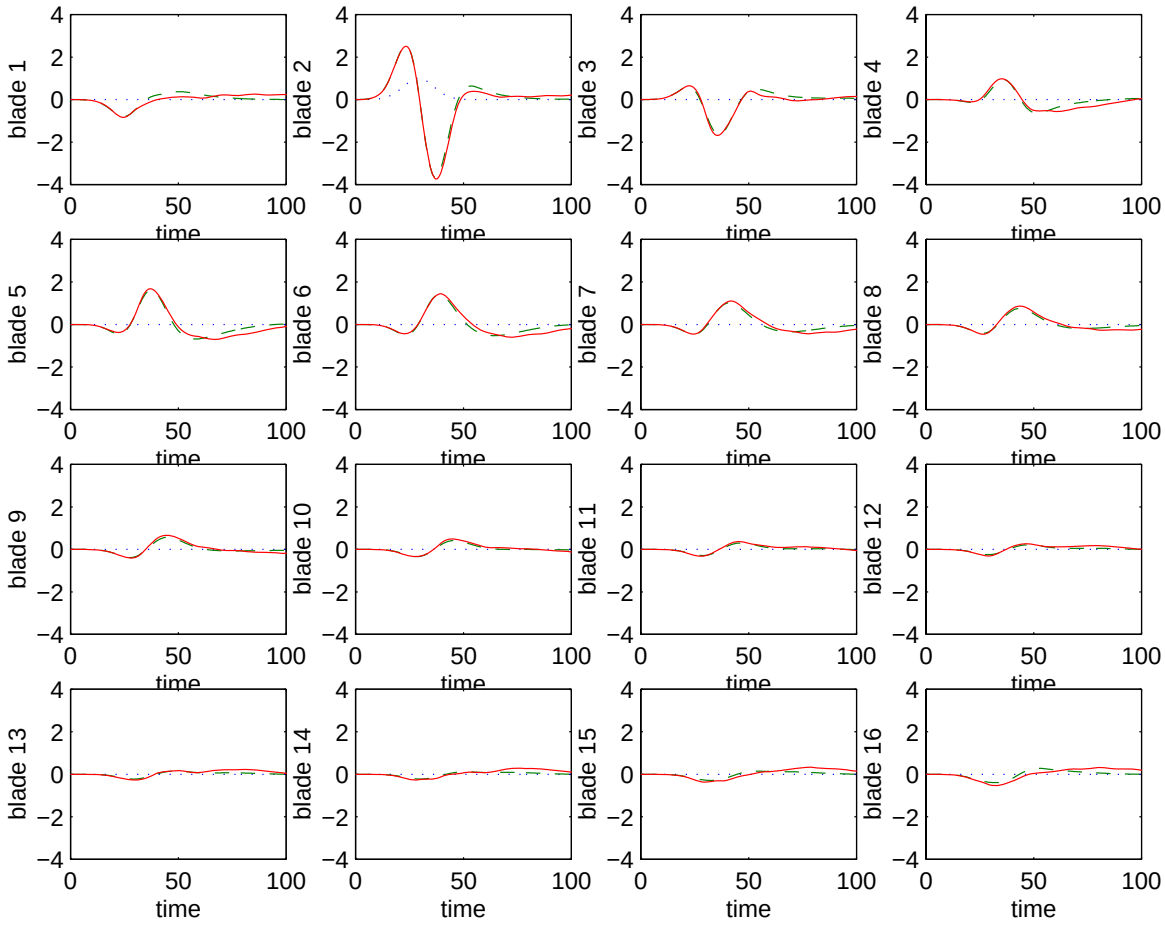

Figure 6-8: Aerodynamic response to pulse displacement input at blade 2. Blade plunge displacement (prescribed, dotted line), rotor alone blade vertical force (dashed line) and rotor/stator system blade vertical force (solid line).

this example, the stator clearly has an important influence and should be included in an aeroelastic analysis.

6.3 Summary

A low-order aeroelastic model has been derived for two blade rows in a subsonic compressor. The model has less than four hundred aerodynamic states, which is reasonable for time marching simulations and the evaluation of eigenvalues. Stability cannot be defined in the same way as for the rotor-alone model by computing the system eigenvalues, since the coefficient matrix varies with time. However, the eigenvalues of the matrix can be computed at various time instants over the rotor revolution period, and loci determined for the eigenvalues. A time simulation can also be performed

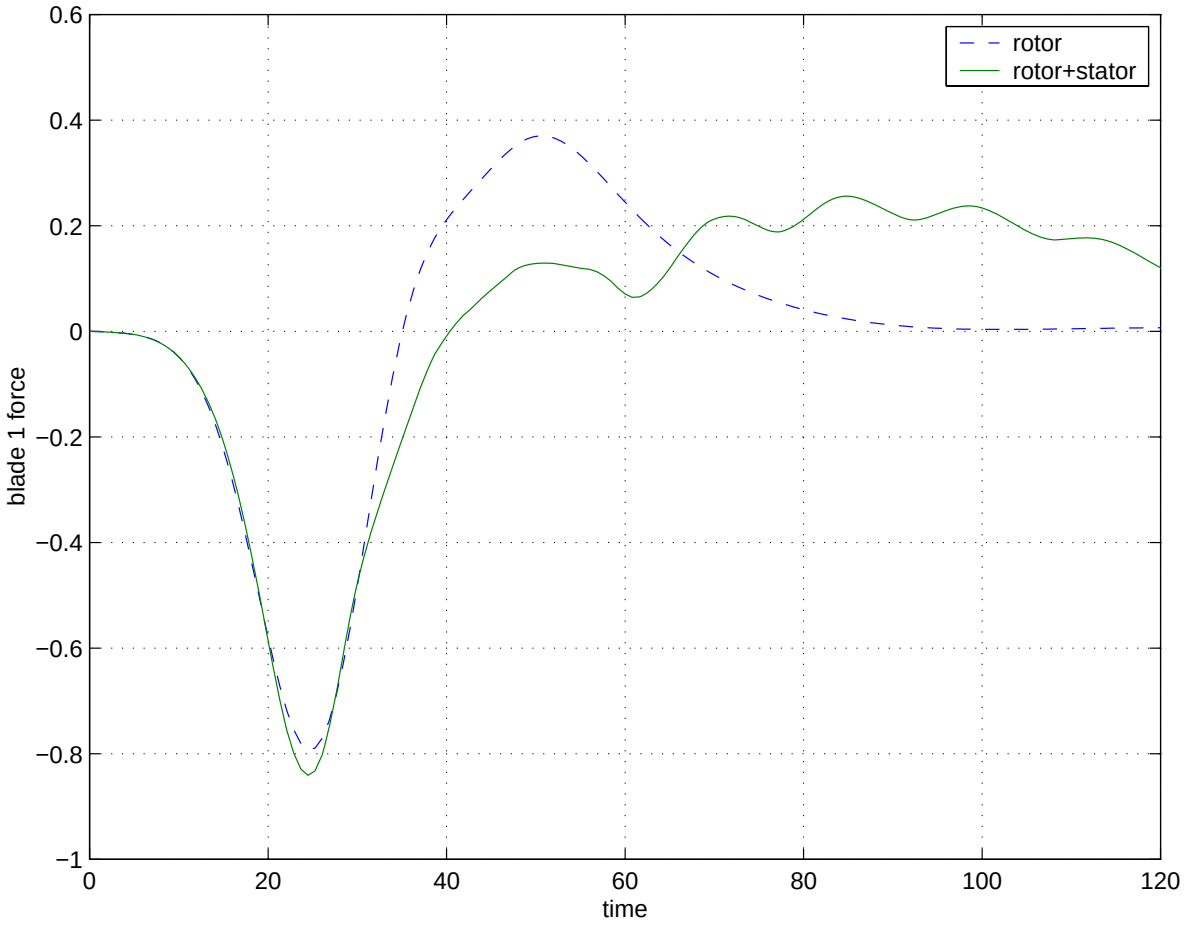

Figure 6-9: Aerodynamic response of blade 1 to pulse displacement input at blade 2. Rotor-alone model (dashed line) and rotor/stator coupled model (solid line).

by applying an initial perturbation to the rotor. The stability of the system can be characterised by considering the resulting aeroelastic response.

For the case presented here, inter-blade row effects are shown to be very significant. For most modes, the addition of the upstream stator has a destabilising effect. As a result, the response amplitude of the coupled stator/rotor aeroelastic system is much larger than that predicted by the isolated rotor analysis. The degree of inter-blade row coupling will vary between problems, depending on the flow conditions and the distance between adjacent blade rows. The model developed in this chapter provides a means of quantifying the effect. For a given problem, preliminary analysis can be performed to determine whether deriving models for an isolated blade row is sufficient, or whether upstream and downstream blade rows should be included to accurately capture the system dynamics. If the addition of an upstream blade row is destabilising, as in the example presented here, it is especially important that it is included in the analysis. Moreover, if viscous effects were included in

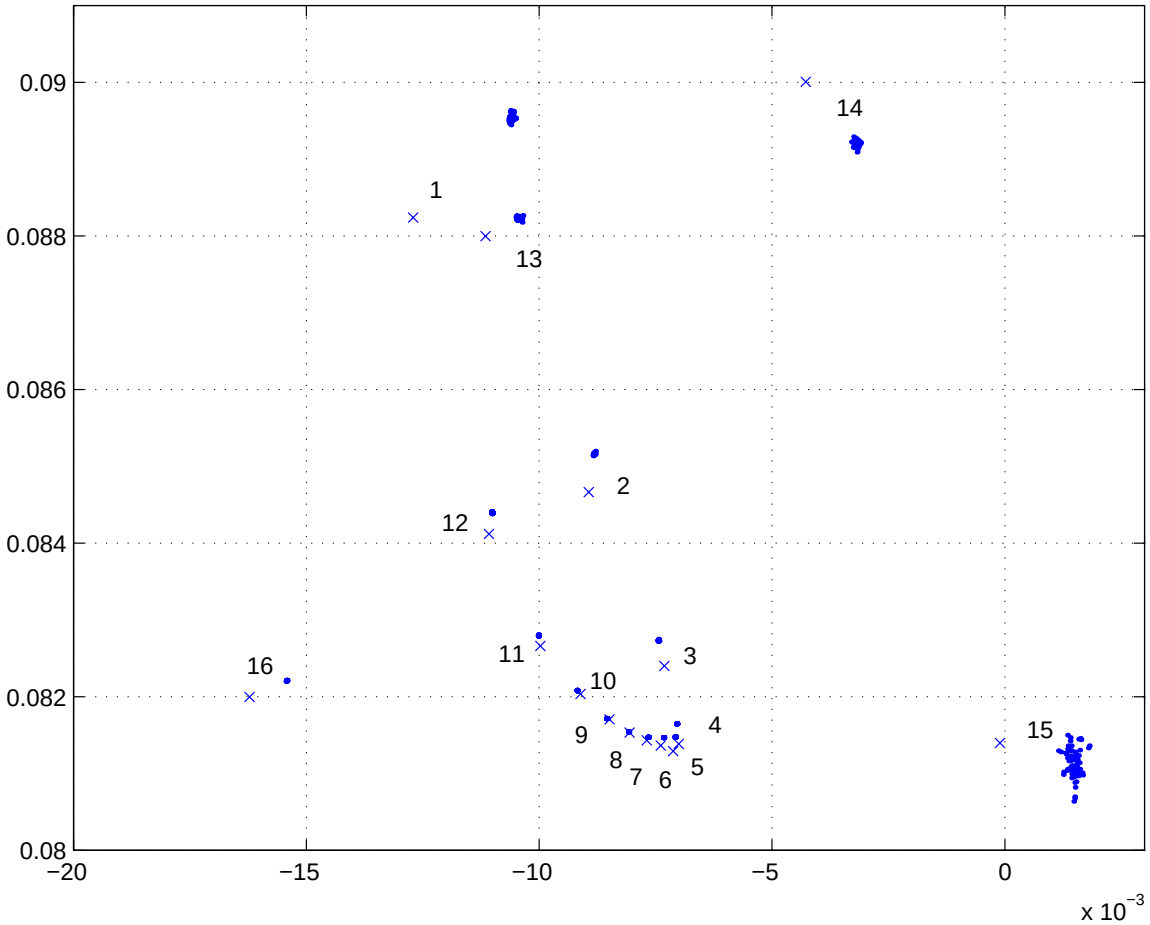

Figure 6-10: Structural eigenvalues : rotor-alone system (crosses) and periodic loci for coupled stator/rotor model (dots). Eigenvalues are numbered by their nodal diameter ($\sigma_\ell = 2\pi\ell/16$). $\mu = 100$, $k = 0.5$, $\zeta = 0.13$.

the model, we would expect the influence of the upstream blade row to be even greater due to the presence of the viscous wakes. We might also expect a transonic stage, where shocks are present, to exhibit a higher degree of inter-blade row coupling. The amount of influence seen here for an inviscid, low subsonic stage suggests that in general, inter-blade row effects are very important and should be included in aeroelastic analyses.

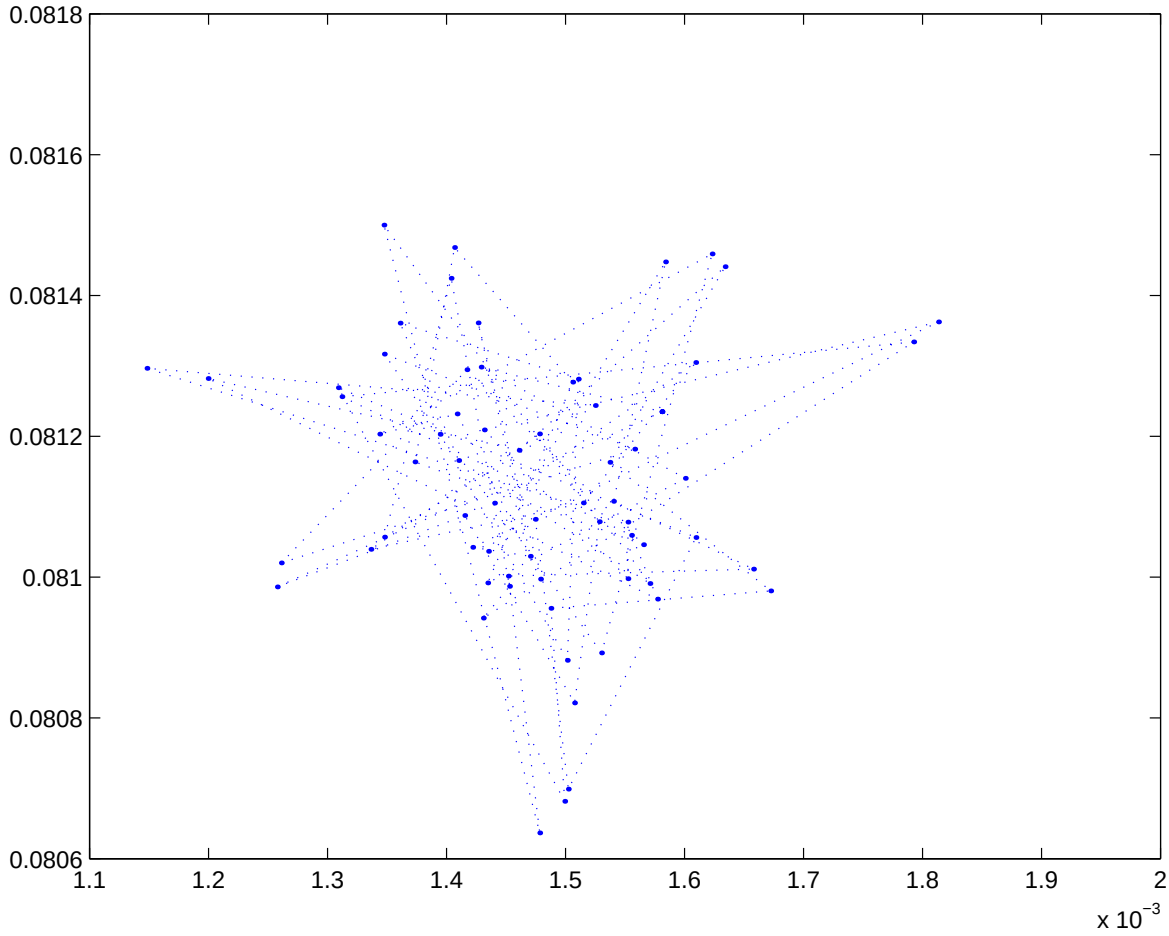

Figure 6-11: Periodic locus of structural eigenvalue for $\ell = 15$ mode.

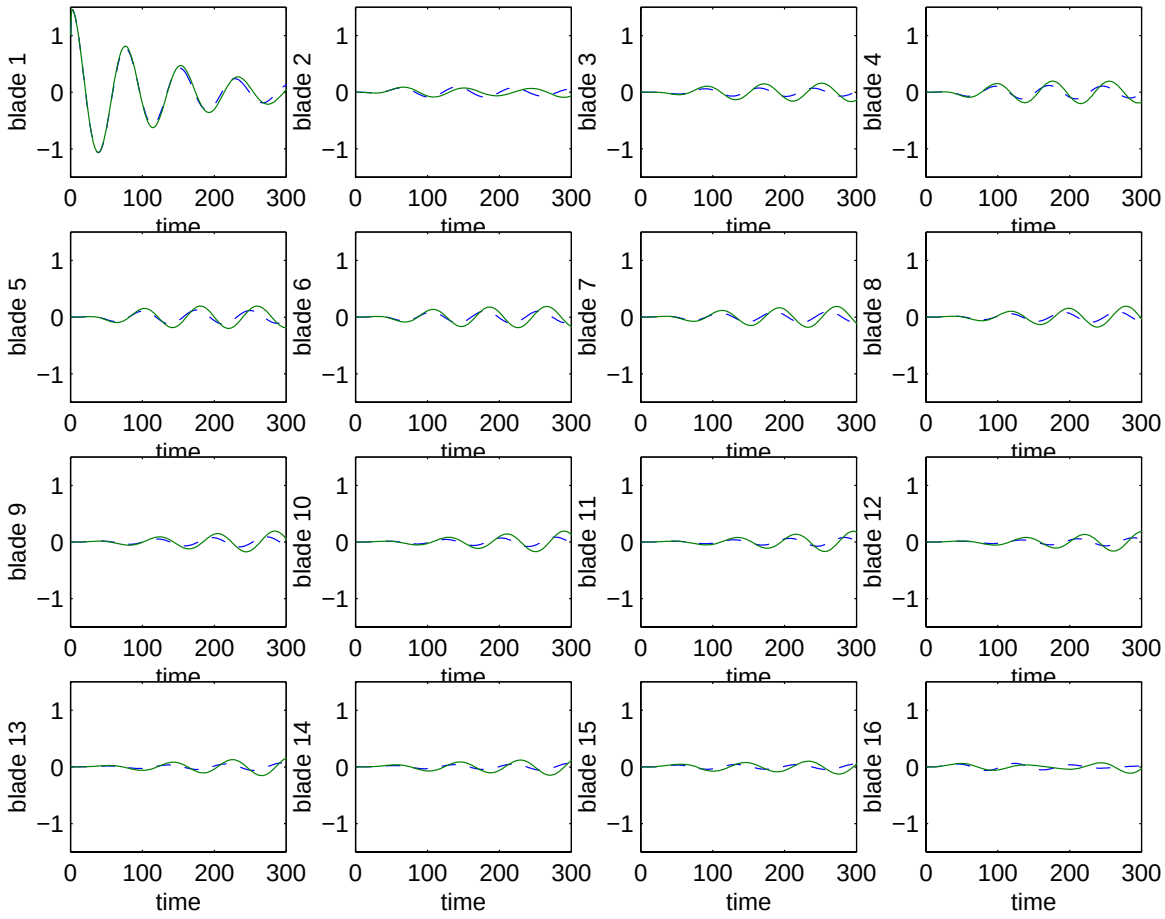

Figure 6-12: Response due to an initial plunge displacement at blade 1. Blade displacement calculated with rotor-alone model (dashed lines) and coupled stator/rotor model (solid lines). $\mu = 100$, $k = 0.5$, $\zeta = 0.13$.

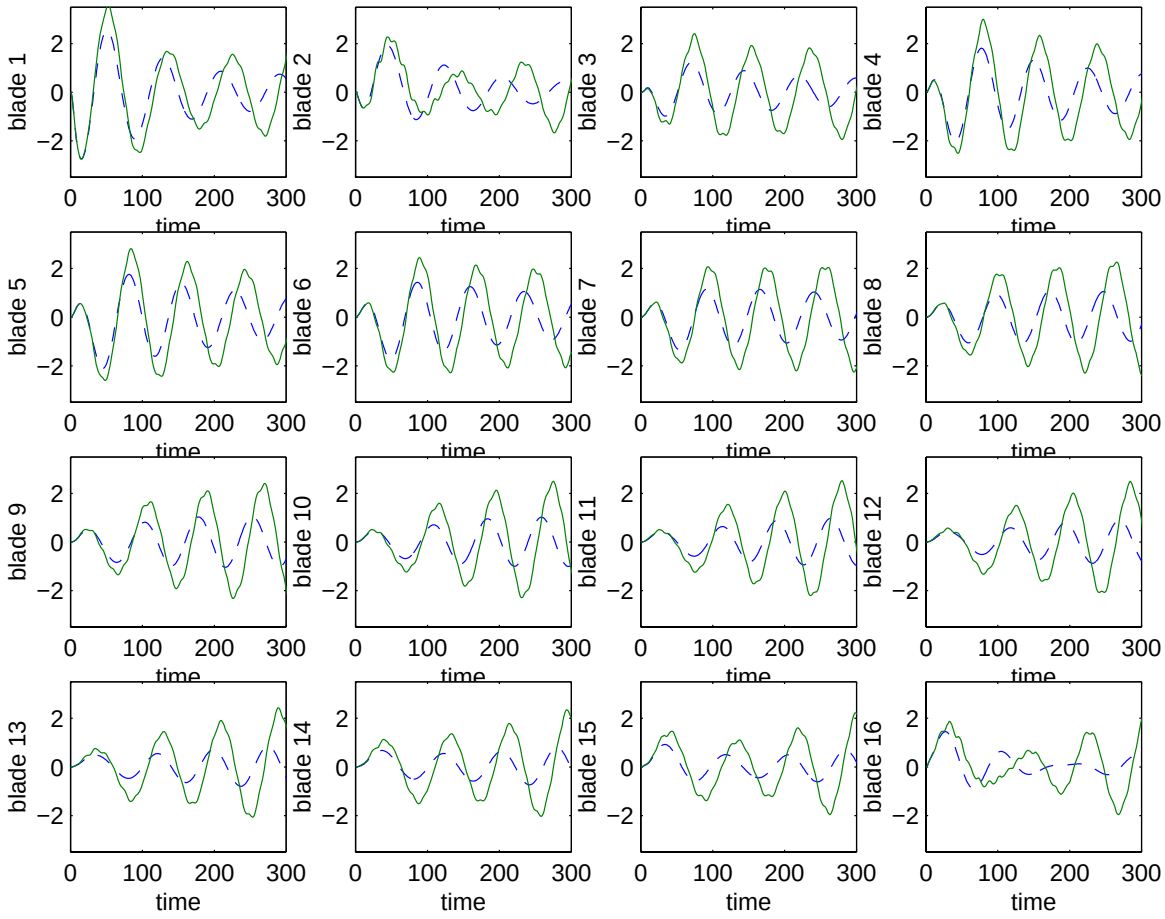

Figure 6-13: Response due to an initial plunge displacement at blade 1. Blade force calculated with rotor-alone model (dashed lines) and coupled stator/rotor model (solid lines). $\mu = 100$, $k = 0.5$, $\zeta = 0.13$.

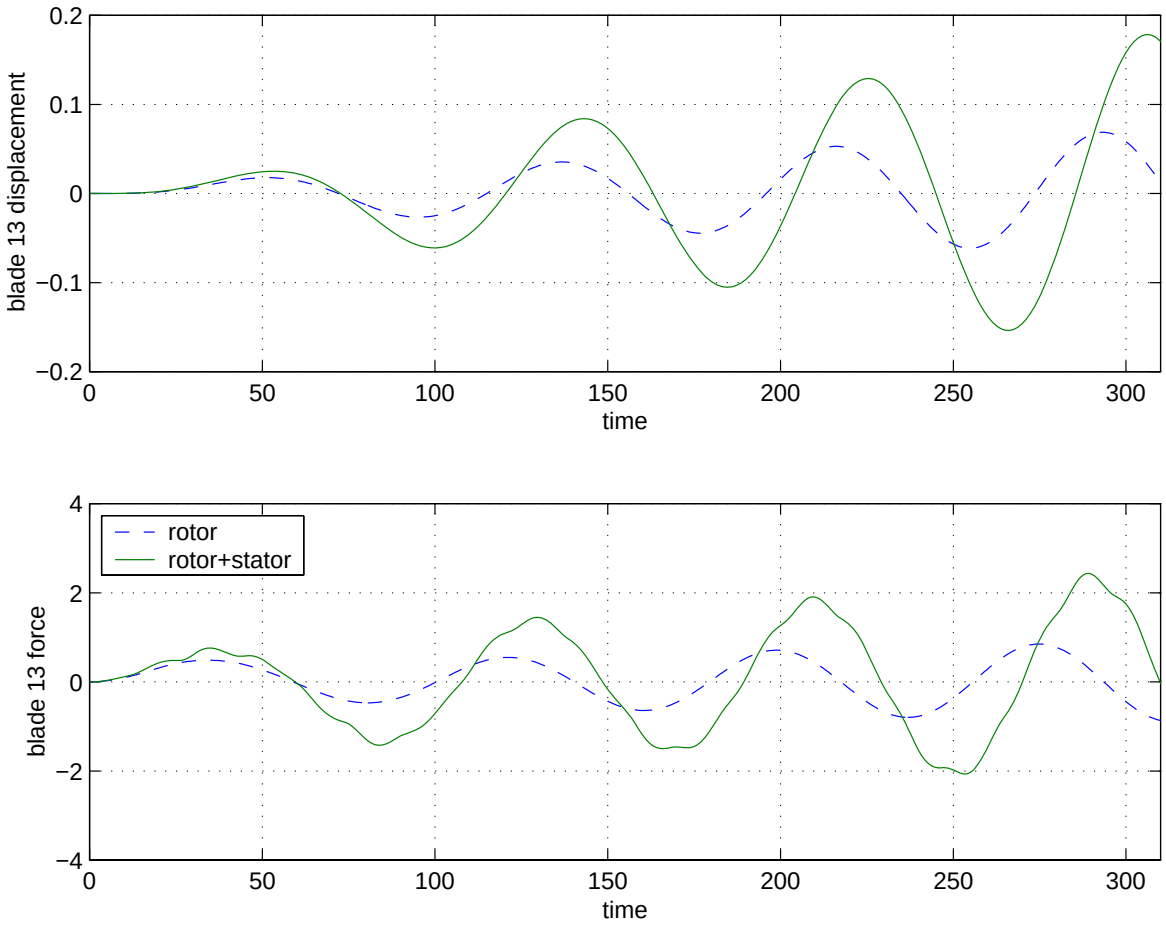

Figure 6-14: Response due to an initial plunge displacement at blade 1. Displacement and force on the thirteenth blade calculated with rotor-alone model (dashed lines) and coupled stator/rotor model (solid lines). $\mu = 100$, $k = 0.5$, $\zeta = 0.13$.

Chapter 7

Conclusions and Recommendations

The aeroelastic model can be formulated as an input/output problem, where the challenge is to find a means of accurately representing the aerodynamics and the structural dynamics, and the interaction between the two. Although CFD and finite element methods may provide models with the desired level of accuracy, they are high order and are therefore not suitable for design or control analysis. Moreover, because the number of controlling parameters in the aerodynamic framework is very high, CFD approaches are generally too expensive for routine determination of stability boundaries. Low-order aerodynamic models can be obtained by systematic reduction of a high-order CFD method. The resulting models replicate the output behaviour of the high-fidelity CFD method over a restricted range of inputs. The reduction can be performed according to the specific problem and which dynamics are considered important, yielding models for a wide range of applications.

Reduced-order aerodynamic models have been developed for the unsteady, linearised, two-dimensional Euler equations. Model order reduction has been demonstrated for both subsonic and transonic blade rows operating in unsteady plunging motion, and shows that three orders of magnitude reduction from the original CFD model is possible, while still accurately capturing the dynamics relevant to flutter and forced response. Simple assumed-frequency aerodynamic models are also derived using the high-order CFD method. These models are of the kind currently used in many aeroelastic analyses, and provide high-fidelity, low-order aerodynamics, but are strictly only valid at the assumed conditions. It is shown that for typical turbomachinery problems, a high degree of coupling exists between the flow and the structure, and in many situations these simple models inaccurately predict the system aeroelastic response. Derivation of reduced-order models using the Arnoldi-based approach is of comparable expense to the assumed-frequency method, but can accurately model

aeroelastic response for a range of inputs.

The reduced-order models are developed in the time domain for the full blade row for several reasons. Firstly, state-space form makes them appropriate for control applications and also allows them to be easily coupled to models of other engine components. To demonstrate this coupling, a model is constructed for a low-speed compressor stage with a stator/rotor configuration. The reduced-order model has less than four hundred states for the coupled stator/rotor system, which allows forced response and stability of the stage to be assessed. The results show that the stator may have an important destabilising effect on the rotor dynamics, and should be included in the analysis if the aeroelastic properties are to be predicted accurately. Secondly, because the models are developed for the full rotor, they can be applied to problems which lack cyclic symmetry. Blade mistuning has been identified as an important factor in determining aeroelastic response, however to date there has been a lack of high-fidelity aerodynamic models suitable for incorporation to a mistuning framework. Current analyses use assumed-frequency models which are even more inadequate when mistuning is present. The reduced-order models developed in this thesis couple naturally into a mistuned analysis, and have been used to investigate structural mistuning in a transonic rotor.

There are a number of extensions which could be applied to the reduced-order models developed in this research. These extensions include improvements on the model order reduction technique and possibilities for additional model applications. It is important to note that although two-dimensional, inviscid flows were considered here, the methodology applies to any linearised CFD model. If this underlying CFD code were available, it would be straightforward to consider three-dimensional and/or viscous effects. Inclusion of these effects would allow analysis of interesting flow phenomena such as tip clearance leakage flows, secondary flows in the blade passages and rotating stall. Moreover, since the Arnoldi vectors approximate the eigenvectors, investigation of the eigenmodes of the reduced-space basis can provide useful physical insight.

In terms of methodology, the Arnoldi-based approach has been used successfully to derive accurate low-order models very efficiently. This method provides several interesting options for future research. In this work, models were derived using a McLaurin expansion of the transfer function. An interesting extension would be to perform the expansion about some non-zero frequency point. A natural choice might be the blade natural frequency; due to the nature of the aeroelastic system, the blade response comprises a range of frequencies about this point. While a single frequency model cannot span this range accurately, an Arnoldi reduced-order model with just a few states could very accurately capture the important dynamics, with just a small increase in computational cost. In addition, the Arnoldi models presented here were derived by considering inputs of interest. It would

also be possible to consider outputs of interest by formulating the dual problem. If the number of inputs exceeds the number of outputs, this approach would be computationally more efficient. To obtain an improved model, a balanced realisation could also be implemented, in which both inputs and outputs of interest are considered.

There are many applications within a turbomachinery context to which one could envision implementing these models. In many cases, current analysis and design tools utilise very simple aerodynamic models which are often insufficient. Due to the general time-domain, input-output form chosen, the reduced-order models developed here can be easily incorporated into virtually any framework. For example, the time domain approach provides a convenient framework for incorporating the compressor analysis within a global engine model, such as the Moore-Greitzer model. In this model, the blade row is represented simply as an actuator disk, but could be replaced with a reduced-order model with appropriate boundary conditions. This framework would allow an accurate analysis of inlet distortions and surge. The use of generalised boundary conditions also allows the high-fidelity aerodynamics to be incorporated within other frameworks, such as analysis of acoustical interactions.

A particular application in which a serious need for suitable higher fidelity aerodynamic models has been identified is mistuning. Reduced-order models have been used in this research to demonstrate the effects of structural mistuning in a rotor. Significant interest also exists in the effects of aerodynamic mistuning. Within the linearised framework described here, sensitivities to blade shape and incidence could be included in the model. Thus the effects of aerodynamic mistuning could be investigated, both in an analysis and a design context.

The major restriction of the reduced-order models developed in this thesis is the assumption of small perturbation unsteady flow. In some cases nonlinear effects may be important, for example in unsteady transonic flows the motion of shocks may have a large nonlinear effect on the solution. Limit cycling is another nonlinear phenomenon exhibited by unsteady flows and is important if flutter stability boundaries are to be predicted accurately. Some consideration needs to be given to incorporating nonlinear effects into the models. It is possible to envision snapshots for a POD model being obtained from a full nonlinear simulation. Such a simulation would need to be performed in the time domain on the full rotor for each frequency and Mach number of interest, thus the computational cost would be significantly increased.

It is clear that reduced-order aerodynamic modelling offers a huge potential for improvement in aeroelastic analysis and design tools. The framework utilised is very general, enabling incorporation of the models to many different applications. The research has developed a methodology for obtaining such models efficiently in a turbomachinery context, and identified several possible applications.

Appendix A

GMRES Algorithm

The solution of a large linear system can be performed efficiently through use of a generalised minimal residual algorithm (GMRES) [62].

The algorithm is best described by considering a differentiable system expressed in vector form as

$$F(U) = 0. \tag{A.1}$$

Given an approximate solution U^n, we construct k orthonormal search directions, p_j, as follows:

$$p_1 = \frac{F(U^n)}{||F(U^n)||}. \tag{A.2}$$

For $j = 1, 2, ...k-1$ take

$$\tilde{p}_{j+1} = \overline{F}(U^n; p_j) - \sum_{i=1}^{j} b_{ij} p_i \tag{A.3}$$

and set

$$p_{j+1} = \frac{\tilde{p}_{j+1}}{||\tilde{p}_{j+1}||}, \tag{A.4}$$

where

$$b_{ij} = \overline{F}(U^n; p_j).p_i \tag{A.5}$$

and $\overline{F}(U^n; p_j)$ denotes the directional derivative of F evaluated at U^n in the direction of p_j and is

approximated as

$$\overline{F}(U^n; p_j) \sim \frac{F(U^n + \epsilon p_j) - F(U^n)}{\epsilon}, \tag{A.6}$$

where ϵ is taken to be a small number proportional to $||U^n||$.

Once the k search directions are known, U^n is updated according to

$$U^{n+1} = U^n + \sum_{j=1}^{k} a_j p_j, \tag{A.7}$$

where the coefficients a_j are evaluated by minimising $||F(U^{n+1})||^2$. The performance of this algorithm is very dependent on the use of a suitable preconditioner. In this research an incomplete LU factorisation routine from the SPARSKIT library [48] was used.

Bibliography

[1] Bolcs A. and T.H. Fransson. Aeroelasticity in Turbomachines; Comparison of Theoretical and Experimental Cascade Results. Technical Report AFOSR-TR-870605, Ecole Polytechnique Federale de Lausanne, 1986.

[2] J.J. Adamczyk and M.E. Goldstein. Unsteady Flow in a Supersonic Cascade wuth Subsonic Leading-Edge Locus. *AIAA Journal*, 16(12):1248–1254, September 1978.

[3] O.O. Bendiksen. Flutter of Mistuned Turbomachinery Rotors. ASME 83-GT-153, 1983.

[4] G. Berkooz, P. Holmes, and J.L. Lumley. The Proper Orthogonal Decomposition in the Analysis of Turbulent Flows. *Annual Review of Fluid Mechanics*, 25:539–575, 1993.

[5] R.L. Bisplinghoff and H. Ashley. *Principles of Aeroelasticity.* Dover Publications, New York, NY, 1975.

[6] D.H. Buffum. Blade Row Interaction Effects on Flutter and Forced Response. AIAA Paper 93-2084, 1993.

[7] E.F. Crawley. Aeroelastic Formulation for Tuned and Mistuned Rotors. AGARD Manual on Aeroelasticity in Axial-Flow Turbomachines, Volume 2, 1988.

[8] E.F. Crawley and K.C. Hall. Optimization and mechanisms of mistuning in cascades. *Transactions of the ASME*, 107:418–426, April 1985.

[9] E.H. Dowell, K.C. Hall, J.P. Thomas, R. Florea, B.I. Epureanu, and J. Heeg. Reduced Order Models in Unsteady Aerodynamics. AIAA Paper 99-1261, 1999.

[10] J. Dugundji and D.J. Bundas. Flutter and Forced Response of Mistuned Rotors Using Standing Wave Analysis. *AIAA Journal*, 22(11):1652–1661, November 1984.

[11] R.C.F. Dye and T.A. Henry. Vibration Amplitudes of Compressor Blades Resulting from Scatter in Blade Natural Frequencies. *ASME Journal of Engineering for Power*, 91:182–188, July 1969.

[12] D.J. Ewins. The Effects of Detuning Upon the Forced Vibrations of Bladed Disks. *Journal of Sound and Vibration*, 9(1):65–79, 1969.

[13] P. Feldmann and R.W. Freund. Efficient Linear Circuit Analysis by Padé Approximation via the Lanczos Process. *IEEE Transactions on Computer-Aided Design of Integrated Circuits and Systems*, 14:639–649, 1995.

[14] R. Florea, K.C. Hall, and P.G.A. Cizmas. Reduced Order Modelling of Unsteady Viscous Flow in a Compressor Cascade. AIAA Paper 96-2572, 1996.

[15] M.B. Giles. Non-Reflecting Boundary Conditions for the Euler Equations. CFDL-TR 88-1, Massachusetts Institute of Technology, February 1988.

[16] M.B. Giles. Stator/Rotor Interaction in a Transonic Turbine. *Journal of Propulsion and Power*, 6(5):621–627, 1990.

[17] M.B. Giles and R. Haimes. Validation of a Numerical Method for Unsteady Flow Calculations. ASME International Gas Turbine and Aeroengine Congress and Exposition, Paper 91-GT-271, Orlando. Florida, 1991.

[18] W.R. Graham, J. Peraire, and K.Y. Tang. Optimal Control of Vortex Shedding Using Low-Order Models, Part II - Model-Based Control. *International Journal for Numerical Methods in Engineering*, 44:973–990, 1999.

[19] E. Grimme. *Krylov Projection Methods for Model Reduction.* PhD thesis, Coordinated-Science Laboratory, University of Illinois at Urbana-Champaign, 1997.

[20] K. C. Hall, J. P. Thomas, and E. H. Dowell. Reduced-Order Modelling of Unsteady Small-Disturbance Flows Using a Frequency-Domain Proper Orthogonal Decomposition Technique. AIAA Paper 99-0655, 1999.

[21] K.C. Hall. *A Linearized Euler Analysis of Unsteady Flows in Turbomachinery.* PhD thesis, Dept. of Aeronautics and Astronautics, MIT, May 1987.

[22] K.C. Hall. Eigenanalysis of Unsteady Flows About Airfoils, Cascades and Wings. *AIAA Journal*, 32(12):2426–2432, December 1994.

[23] K.C. Hall and E.F. Crawley. Calculation of Unsteady Flows in Turbomachinery Using the Linearized Euler Equations. *AIAA Journal*, 27(6):777–787, September 1989.

[24] K.C. Hall, R. Florea, and P.J. Lanzkron. A Reduced Order Model of Unsteady Flows in Turbomachinery. ASME Paper 94-GT-291, 1994.

[25] K.C. Hall and P.D. Silkowski. The Influence of Neighboring Blade Rows on the Unsteady Aerodynamic Response of Cascades. ASME 95-GT-35, 1995.

[26] D.E. Hobbs, J.H. Wagner, J.F. Dannenhoffer, and R.P. Dring. Supercritical Airfoil Technology Program, Wake Experiments and Modeling for Fore and Aft-Loaded Compressor Cascades. Final Report FR-13514, Pratt and Whitney Aircraft Group, UTC, September 1980.

[27] M. Kamon, F. Wang, and J.K. White. Recent Improvements to Fast Inductance Extraction and Simulation. Proceedings of the 7^{th} Topical Meeting on Electrical Performance of Electronic Packaging, West Point, NY, October 1998.

[28] K.R. Kaza and R.E. Kielb. Coupled Bending-Torsion Flutter of a Mistuned Cascade with Nonuniform Blades. AIAA Paper 82-0726, 1982.

[29] K.R. Kaza and R.E. Kielb. Flutter and Response of a Mistuned Cascade in Incompressible Flow. *AIAA Journal*, 20(8):1120–1127, August 1982.

[30] J. Kenyon and D. Rabe. Aerodynamic Effects on Blade Vibratory Stress Vibrations. AIAA Paper 98-3744, Lake Buena Vista, Florida, 1998.

[31] J.L. Kerrebrock. *Aircraft Engines and Gas Turbines*. MIT Press, Cambridge, 2nd edition, 1992.

[32] T. Kim. Frequency-Domain Karhunen-Loeve Method and Its Application to Linear Dynamic Systems. *AIAA Journal*, 36(11):2117–2123, 1998.

[33] M. Kruse and C. Pierre. Dynamic Response of an Industrial Turbomachinery Rotor. Proceedings of the 32nd AIAA/ASME/SAE/ASEE Joint Propulsion Conference and Exhibit, 1996.

[34] M. Kruse and C. Pierre. Forced Response of Mistuned Bladed Disks using Reduced-Order Modeling. AIAA Paper 96-1545-CP, 1996.

[35] R.B. Lehoucq, D.C. Sorensen, and C. Yang. *ARPACK Users Guide: Solution of Large Scale Eigenvalue Problems by Implicitly Restarted Arnoldi Methods*. Rice University, October 1997.

[36] M. Loéve. *Probability Theory*. D. Van Nostrand Company Inc., New York, 1955.

[37] J.L. Lumley. The Structures of Inhomogeneous Turbulent Flow. *Atmospheric Turbulence and Radio Wave Propagation*, pages 166–178, 1967.

[38] A.J. Mahajan, E.H. Dowell, and D.B. Bliss. Eigenvalue Calculation Procedure for an Euler/Navier-Stokes Solver with Application to Flows over Airfoils. *Journal of Computational Physics*, 97:398–413, 1991.

[39] S.R. Manwaring and D.C. Wisler. Unsteady Aerodynamics and Gust Response in Compressors and Turbines. *Journal of Turbomachinery*, 115(4):724–740, 1993.

[40] F.K. Moore and E.M. Greitzer. A Theory of Post-Stall Transients in Axial Compression Systems: Part I - Development of Equations. *Journal of Engineering for Gas Turbines and Power*, 108:68–76, January 1986.

[41] B.R. Noack and H. Eckelmann. A global stability analysis of the steady and periodic cylinder wake. *Journal of Fluid Mechanics*, 270:297–330, 1994.

[42] G.S. Ottarsson, M.P. Castanier, and C. Pierre. A Reduced-Order Modeling Technique for Mistuned Bladed Disks. Proceedings of the 35th AIAA/ASME/ASCE/AHS/ASC Structures, Structural Dynamics, and Materials Conference, 1994.

[43] G.S. Ottarsson and C. Pierre. On the Effects of Interblade Coupling on the Statistics of Maximum Forced Response Amplitudes in Mistuned Bladed Disks. Proceedings of the 36th AIAA/ASME Structures, Structural Dynamics, and Materials Conference, 1995.

[44] M.M. Rai. Navier-Stokes Simulations of Rotor-Stator Interaction Using Patched and Overlaid Grids. *Journal of Propulsion and Power*, 3(5):387–396, 1987.

[45] M.C. Romanowski. Reduced Order Unsteady Aerodynamic and Aeroelastic Models using Karhunen-Loéve Eigenmodes. AIAA Paper 96-194, 1996.

[46] M.C. Romanowski and E.H. Dowell. Using Eigenmodes to Form an Efficient Euler Based Unsteady Aerodynamics Analysis. Proceedings of the Special Symposium on Aeroelasticity and Fluid/Structure Interaction Problems, ASME International Mechanical Engineering Congress and Exposition, AD-Vol. 44, pp. 147-160, 1994.

[47] Y. Saad. Numerical Methods for Large Eigenvalue Problems. Manchester University Press Series in Algorithms and Architectures for Advanced Scientific Computing, 1991.

[48] Y. Saad. *SPARSKIT: a basic tool kit for sparse matrix computations, Version 2 User Manual*, June 1994.

[49] B. Shapiro. Symmetry Approach to Extension of Flutter Boundaries via Mistuning. *Journal of Propulsion and Power*, 14(3):354–366, May-June 1998.

[50] B. Shapiro. *Passive Control of Flutter and Forced Response in Bladed Disks via Mistuning.* PhD thesis, California Institute of Technology, May 1999.

[51] P.D. Silkowski. Measurements of Rotor Stalling in a Matched and Mismatched Compressor. GTL Report 221, MIT, April 1995.

[52] L.M. Silveira, M. Kamon, I. Elfadel, and J. White. A Coordinate-Transformed Arnoldi Algorithm for Generating Guaranteed Stable Reduced-Order Models of RLC Circuits. *Computer Methods in Applied Mechanics and Engineering*, 169(3-4):377–389, February 1999.

[53] L. Sirovich. Turbulence and the Dynamics of Coherent Structures. Part 1 : Coherent Structures. *Quarterly of Applied Mathematics*, 45(3):561–571, October 1987.

[54] T. Theodorsen. General Theory of Aerodynamic Instability and the Mechanism of Flutter. Report 685, NACA, 1940.

[55] L.N. Trefethen and D. Bau. *Numerical Linear Algebra*. SIAM, Philadelphia, PA, 1997.

[56] J.M. Verdon. Review of Unsteady Aerodynamic Methods for Turbomachinery Aeroelastic and Aeroacoustic Applications. *AIAA Journal*, 31(2):235–250, February 1993.

[57] S.T. Wei and C. Pierre. Localization Phenomena in Mistuned Assemblies with Cyclic Symmetry, Part I: Free Vibrations. *ASME Journal of Vibration, Acoustics, Stress, and Reliability in Design*, 110(4):429–438, 1988.

[58] S.T. Wei and C. Pierre. Localization Phenomena in Mistuned Assemblies with Cyclic Symmetry, Part II: Forced Vibrations. *ASME Journal of Vibration, Acoustics, Stress, and Reliability in Design*, 110(4):439–449, 1988.

[59] D.S. Whitehead. Vibration of Cascade Blades Treated by Actuator Disc Methods. *Proceedings of the Institution of Mechanical Engineers*, 173(21):555–574, 1959.

[60] D.S. Whitehead. Force and Moment Coefficients for Vibrating Airfoils in Cascade. British Aeronautical Research Council, London, R.&M. 3254, February 1960.

[61] D.S. Whitehead. Classical Two-Dimensional Methods. AGARD Manual on Aeroelasticity in Axial-Flow Turbomachines, Unsteady Turbomachinery Aerodynamics, Volume 1, 1987.

[62] L.B. Wigton, N.J. Yu, and D.P. Young. GMRES Acceleration of Computational Fluid Dynamics Codes. AIAA Paper 85-1494, 1985.

[63] Karen E. Willcox. Aeroelastic Computations in the Time Domain Using Unstructured Meshes. Master's thesis, Dept. of Aeronautics and Astronautics, MIT, February 1996.

[64] K.E. Willcox, J.D. Paduano, J. Peraire, and K.C. Hall. Low Order Aerodynamic Models for Aeroelastic Control of Turbomachines. AIAA Paper 99-1467, 1999.

[65] K.E. Willcox, J. Peraire, and J. White. An Arnoldi Approach for Generation of Reduced-Order Models for Turbomachinery. Submitted, *Computers and Fluids*, 1999.